AFRL-AFOSR-UK-TR-2014-0040

Guiding of long-distance electric discharges by combined femtosecond and nanosecond pulses emitted by hybrid KrF laser system

Ionin Andrey Alekseevich

INSTITUTION OF RUSSIAN ACADEMY OF SCIENCES
QUANTUM RADIO PHYSICS INSTITUTE
53 LENINSKY PROSPECT
MOSCOW, 119991 RUSSIA

EOARD ISTC 09-7007/Proj 4073p

Report Date: January 2014

Final Report from 27 September 2010 to 31 December 2013

Air Force Research Laboratory
Air Force Office of Scientific Research
European Office of Aerospace Research and Development
Unit 4515, APO AE 09421-4515

REPORT DOCUMENTATION PAGE

Form Approved OMB No. 0704-0188

1. REPORT DATE *(DD-MM-YYYY)*	2. REPORT TYPE	3. DATES COVERED *(From – To)*
30 January 2014	Final Report	27 September 2010 – 31 December 2013

4. TITLE AND SUBTITLE

Guiding of long-distance electric discharges by combined femtosecond and nanosecond pulses emitted by hybrid KrF laser system

5a. CONTRACT NUMBER
ISTC Proj 4073p

5b. GRANT NUMBER
ISTC 09-7007

5c. PROGRAM ELEMENT NUMBER
61102F

6. AUTHOR(S)

Ionin Andrey Alekseevich

5d. PROJECT NUMBER

5d. TASK NUMBER

5e. WORK UNIT NUMBER

7. PERFORMING ORGANIZATION NAME(S) AND ADDRESS(ES)
INSTITUTION OF RUSSIAN ACADEMY OF SCIENCES
QUANTUM RADIO PHYSICS INSTITUTE
53 LENINSKY PROSPECT
MOSCOW, 119991 RUSSIA

8. PERFORMING ORGANIZATION REPORT NUMBER
N/A

9. SPONSORING/MONITORING AGENCY NAME(S) AND ADDRESS(ES)
EOARD
Unit 4515
APO AE 09421-4515

10. SPONSOR/MONITOR'S ACRONYM(S)
AFRL/AFOSR/IOE (EOARD)

11. SPONSOR/MONITOR'S REPORT NUMBER(S)
AFRL-AFOSR-UK-TR-2014-0040

12. DISTRIBUTION/AVAILABILITY STATEMENT

Distribution A: Approved for public release; distribution is unlimited.

13. SUPPLEMENTARY NOTES

14. ABSTRACT

The results obtained within the framework of the present project can be tentatively grouped as follows. The first part (Sections 2, 3) of the present project is devoted to a detailed description of the schemes for subpicosecond USP amplification in a chain of large-aperture KrF amplifiers with electron-beam pumping, as well as lasing dynamics of combined (amplitude-modulated) high-energy 100-ns long UV laser pulses in the regime of regenerative amplification of a USP train. Experimental and theoretical studies of filamentation of the USP UV and IR laser beams in atmospheric air, of the processes of air ionization, electron loss and revival in the laser-produced air plasma are described in the second part (Sections 4–6). The third part (Sections 7, 8) demonstrates the advantages of amplitude-modulated pulses in the production of extended plasma channels in the atmosphere and laser guiding of high-voltage electric discharges.

15. SUBJECT TERMS

EOARD, triggering and guiding electric discharge, KrF laser, femtosecond pulse, nanosecond pulse, filamentation, plasma channel, lightning control, laser control of discharge

16. SECURITY CLASSIFICATION OF:			17. LIMITATION OF ABSTRACT	18, NUMBER OF PAGES	19a. NAME OF RESPONSIBLE PERSON
a. REPORT	b. ABSTRACT	c. THIS PAGE			John Gonglewski
UNCLAS	UNCLAS	UNCLAS	SAR	93	19b. TELEPHONE NUMBER *(Include area code)* +44 (0)1895 616007

ISTC Project No. 4073 P

Guiding of long-distance electric discharges by combined femtosecond and nanosecond pulses emitted by hybrid KrF laser system

Final Project Technical Report

on the work performed from October 01, 2010 to December 31, 2013

P.N.Lebedev Physical Institute of Russian Academy of Sciences

Project Manager	**Ionin Andrey Alekseevich** **Professor, Dr. of Sciences**	_____
Director	**Mesyats Gennady Andreevich** **Academician, Dr. of Sciences**	_____

January 2014

This work is supported financially by European Office of Aerospace Research and Development (EOARD) and performed under the agreement with the International Science and Technology Center (ISTC), Moscow.

Title of the Project:	Guiding of long-distance electric discharges by combined femtosecond and nanosecond pulses emitted by hybrid KrF laser system
Commencement Date:	October 1, 2010
Duration:	39 months
Project Manager	Ionin Andrey Alekseevich
phone number:	7(499)783 3690
fax number:	7(499)783 3690
e-mail address:	aion@sci.lebedev.ru
Leading Institute:	P.N.Lebedev Physical Institute of Russian Academy of Sciences 53 Leninsky pr., 119991 Moscow, Russia 7(499)135 2430 postmaster@sci.lebedev.ru www.lebedev.ru
Participating Institutes:	None
Foreign Collaborators:	European Office of Aerospace Research and Development (EOARD) Bldg 186, 86 Blenheim Crescent, HA4 7HB Middlesex, United Kingdom +44 (0) 189 561 6146 Susan.fuller@london.af.mil <URL> if exist

Keywords: triggering and guiding electric discharge, KrF laser, femtosecond pulse, nanosecond pulse, filamentation, plasma channel

PARTICIPANTS OF THE PROJECT

Prof. Ionin Andrey Alekseevich
Dr. Levchenko Aleksey Olegovich
Dr. Klimachev Yurii Milhailovich
Dr. Kotkov Andrei Aleksandrovich
Dr. Kudryshov Sergey Ivanovich
Dr. Seleznev Leonid Vladimirovich
Dr. Sinitsyn Dmitrii Vasil'evich
Dr. Smetanin Igor Valentinovich
Dr. Ustinovsky Nikolai Nikolaevich
Dr. Zvorykin Vladimir Dmitrievich
Ionina Nina Anatol'evna
Kozlov Andrei Yur'evich
Shutov Aleksey Viktorovich
Sunchugasheva Elena Sergeevna

LIST OF CONTENTS

1. Introduction and Overview

The possibility of producing with the help of laser radiation an extended (tens and hundreds of meters in length) conducting plasma channel in the atmospheric air has attracted the attention of researchers since the 1970s. An artificial plasma waveguide may be employed for wireless transmission of electric current [1, 2] as well as of microwave and radio-frequency electromagnetic radiation for lowering its natural divergence [3–6]. Among important practical problems are the development of an active lightning protection system involving laser initiation and lightning trajectory control (see, for instance, papers [7–11] and references therein) as well as remote monitoring of atmospheric pollution with the use of a nitrogen laser operating in the regime of single-pass radiation amplification in the plasma channel produced by high-power ultra short pulses (USPs) in the air [12]. Of special interest for the solution of these problems is UV laser radiation, for which the multiphoton ionization (MPI) probability of the air is considerably higher than for infrared (IR) radiation [13], and it becomes the main gas ionization mechanism even for relatively low radiation intensities $I \geq 5\times10^8$ W cm^{-2} readily attainable with laser pulses tens or hundreds of nanoseconds in duration. This is attested, for instance, by the experiments [6, 11], where the GARPUN KrF laser operated in the regime of injection of laser pulses produced by an electric-discharge KrF master oscillator into the unstable confocal resonator with output smooth 100-ns long pulses of ultraviolet (UV) radiation (λ = 248 nm), laser energy amounted to 100 J and the divergence was of ~2×10^{-4} rad [14]. The laser produced tubular plasma waveguides in atmospheric air, which transmitted microwave radiation for a distance tens of meters in length, and extended plasma channels, which efficiently controlled a high-voltage discharge approximately 1 m in length. In the recent version being upgraded with a frequency-tripled femtosecond Ti: Sapphire front-end the novel Ti: Sapphire / KrF hybrid GARPUN-MTW laser system [15] acquired the capability to amplify subpicosecond pulses to energy of ~1 J [16, 17], in addition to the capability of generating long (100 ns) UV pulses.

The background to the present project is formed by the experiments involving electron density measurements in the plasma produced by the radiation of electric-discharge KrF laser with a pulse duration τ = 25 ns [6], which highlighted two significant circumstances. First, for intensities $I \geq 3\times10^8$ W cm^{-2} the photoelectron density n_e increases quadratically with intensity: $n_e \propto I^2$. This takes place in accordance with the stepwise Resonance Enhanced Multi-Photon Ionization (REMPI) mechanism, (2 + 1), via two-photon resonance excitation of oxygen molecules [18], which have the lowest ionization potential among the air components (I_i = 12.06 eV). Second, in the sequential action of two laser pulses spaced at a period approximately equal to the electron lifetime ($\Delta t \approx \tau_e$), not only does the second pulse produce its own portion of photoelectrons, but it also detaches those which are produced by the first pulse and managed to adhere to O_2 molecules. In this case, relatively low radiation intensity (~10^7 W cm^{-2}) is required for the efficient photodetachment of the adhered electrons [6]. Therefore, by going over from a smooth 100-ns long UV pulse to a combined amplitude-modulated pulse consisting of an USP train and a long pulse of quasi-stationary lasing, with the GARPUN-MTW facility it will be possible to substantially increase the electron plasma density [19–22]. This approach has been realized in our further experiments, the main results being published in papers [23–35].

The results obtained within the framework of the present project can be tentatively grouped as follows. The first part (Sections 2, 3) of the present project is devoted to a detailed description of the schemes for subpicosecond USP amplification in a chain of large-aperture KrF amplifiers with electron-beam pumping, as well as lasing dynamics of combined (amplitude-

modulated) high-energy 100-ns long UV laser pulses in the regime of regenerative amplification of a USP train. Experimental and theoretical studies of filamentation of the USP UV and IR laser beams in atmospheric air, of the processes of air ionization, electron loss and revival in the laser-produced air plasma are described in the second part (Sections 4–6). The third part (Sections 7, 8) demonstrates the advantages of amplitude-modulated pulses in the production of extended plasma channels in the atmosphere and laser guiding of high-voltage electric discharges.

2. Amplification of nanosecond and femtosecond pulses in e-beam-pumped KrF laser amplifiers

2.1. Initial remarks on the ultra-short pulse amplification in KrF gain medium

Particular features of KrF lasers operating on B→X bound-free transitions [15–17] are short lifetime of the excited state of the molecule (radiative time $\tau_r \sim 6$ ns; the lifetime due to collisional quenching τ_c is ~ 2 ns), large induced emission cross section $\sigma = 2.5 \cdot 10^{-16}$ cm^2, low saturation energy $Q_s = h\nu/\sigma = 2$ mJ/cm^2 (where $h\nu = 5$ eV is the energy of radiation quantum), and significant nonsaturable loss in a gain medium (typical ratio of small-signal gain to absorption coefficient g_0/α =10–20). Because of the rapid recovery time of the population inversion in the gain medium, which equals $\tau_c \sim 2$ ns for the quasi-stationary pumping condition of our KrF lasers, a single USP (with duration $\tau_p \le \tau_c$) extracts a small part (2–3%) of the total pumping energy delivered by e-beam with a typical pulse length of ~100 ns. The rest of energy is lost in the form of **A**mplified **S**pontaneous **E**mission (ASE). On the other hand, each USP does not affect the subsequent pulse if the latter follows with time interval $\Delta t \ge \tau_c$. That is why such a train of the USPs will be effectively amplified extracting much of the stored energy. Long pulses with $\tau_p \ge \tau_r$ are amplified in a quasi-steady mode. During their amplification at the optimal intensity (corresponding to maximum extraction efficiency) $I_{opt}=I[(g_0/\alpha)^{1/2}-1]$ the energy stored in the gain medium is not completely extracted. The rest can be used for simultaneous amplification of USPs, though with less gain $g = (g_0\alpha)^{1/2}$ [36]. This also might be a way to reduce the ASE, which decreases a contrast of the USP.

2.2. Basic components of the hybrid Ti: Sapphire / KrF GARPUN-MTW laser system

Hybrid Ti:Sapphire/KrF laser facility combines a previous version of e-beam-pumped multistage GARPUN KrF laser [14] with later launched Ti:Sapphire front-end "Start-248 M" [15]. The final large-aperture GARPUN amplifier with a gain volume of 12×18×100 cm^3 is pumped by two counter-propagating 350-keV, 60-kA (50 A/cm^2), 100-ns e-beams guided by magnetic field of ~0.08 T. When operating in free-running oscillation mode with Ar/Kr/F_2 gas mixture at 1.4-atm pressure and with specific pumping power W_b = 0.7–0.8 MW/cm^3, it provides up to 100 J in 100-ns pulse. Another 8×8×110-cm^3 Berdysh module pumped by a single-side magnetic field-guided 350-keV, 50-kA (50 A/cm^2), 100-ns e-beam with W_b = 0.6–0.7 MW/cm^3 produces up to 25 J at 1.8-atm gas mixture. Both amplifiers are synchronized with KrF master oscillator (Lambda Physik EMG TMSC 150 model) producing 200-mJ, 25-ns pulses, which ignites laser-triggered switches of HV pulsed power supply of e-beam guns of both Berdysh and GARPUN amplifiers. Frequency tripled Ti:Sapphire front-end "Start-248 M" (Avesta Project Ltd.) is designed to generate 10-Hz train of 0.5-mJ, 60-fs pulses at wavelength λ=248 nm matched with KrF gain band.

2.3. Double pass amplification of a single USP in KrF amplifiers

The layout of experiments on amplification of USPs is shown in **Fig. 2.1** with appropriate equipment for measuring pulse energy, duration, spectral and spatial distribution. A single pulse is cut out of 10Hz Ti:Sapphire front-end train and synchronized with KrF amplifiers within accuracy of ±5 ns at the top of 100-ns pumping pulse. Double-pass amplification is used for both preamplifier and final amplifier with a spatial filter placed between them. Initial 8-mm front-end beam diameter is successively expanded by convex and concave mirrors to fit amplifier apertures. The only transparent optics is CaF_2 amplifier windows inclined to prevent parasitic oscillations, and spatial filter windows.

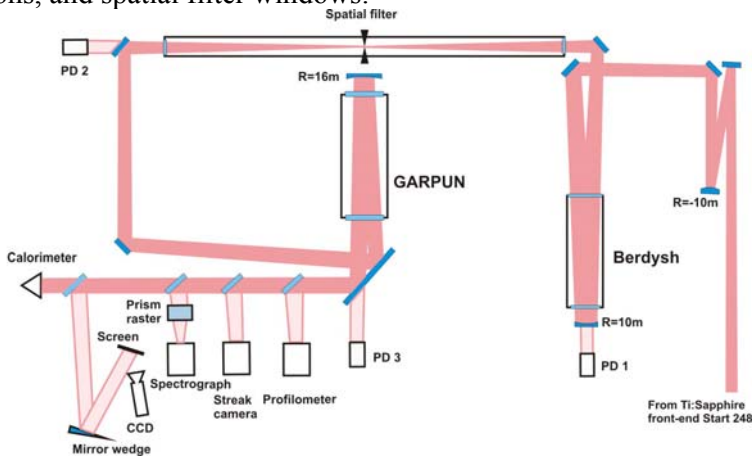

Figure 2.1. Layout of double-pass amplification of USPs in Berdysh and GARPUN amplifiers.

Figures 2.2, 2.3 present experimental dependences of output energy E_{out} on input one E_{in} for double-pass amplification in both Berdysh preamplifier and GARPUN amplifier compared with numerical simulation for various small-signal gain coefficients g_0 and nonsaturable absorption α. Depletion of the gain by the ASE in folded amplifiers is taken into account with corresponding gain profiles along the amplifiers [15]. The preamplifier operating with maximal Q_{out} = 0.6 mJ/cm^2 is far from saturation (Q_s=2 mJ/cm^2) and has a stage gain G = 70 (E_{out}/E_{in}). A deviation of experimental dots from calculated curves is probably due to nonlinear absorption of laser radiation in preamplifier windows, which should increase at higher intensities. Total output energy over laser beam cross-section area S_b = 38.5 cm^2 (it is averaged along the amplifier) is E_{out} = 23 mJ with a fill factor f = 0.6 (a fraction of S_b relative to the whole amplifier aperture). The final amplifier is saturated by Q_{out} = 6.7 mJ/cm^2, which gives total E_{out} = 620 mJ over S_b = 92.5 cm^2 (f = 0.43). Contribution of the ASE in a solid angle of calorimeter (~ 2×10^{-5} sr) is ~ 3%.

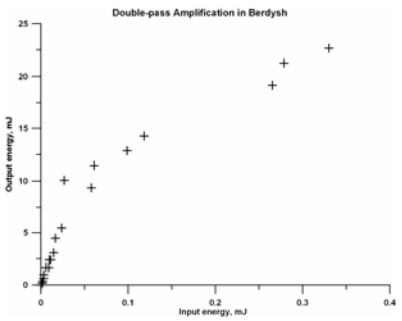

Figure 2.2. Output energy E_{out} vs. input E_{in} for Berdysh preamplifier.

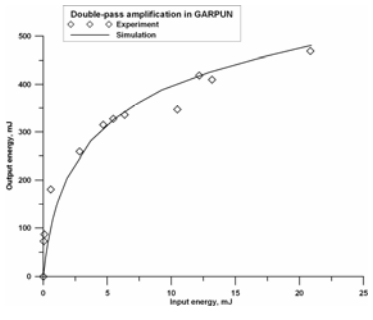

Figure 2.3. Output energy E_{out} vs. input E_{in} for GARPUN amplifier.

For 0.1-ps input pulse in present experiments, output pulse is time-broadened by group velocity dispersion (GVD) in amplifier windows (their total thickness for a double pass is 200 mm) and laboratory air along an extended amplification route of the length ~50 m. Its duration has been estimated by using two methods: by interference of two beams being split by a mirror wedge and by a streak camera. In fact a coherence length is measured using the former approach, which gives a lower limit $\tau_{1/2} \sim 0.33$ ps. The latter measurement is limited by a temporal resolution of the camera and gives upper limit $\tau_{1/2} \leq 1$ ps.

Spatial distribution of radiation is affected by block-like structure of CaF_2 amplifier windows (it is the best material in respect of nonlinear absorption) that introduces phase modulation at block boundaries and stimulated beam filamentation, as pulse power P~1 TW>> $P_{cr} \approx 100$ MW, critical power for filamentation of UV (λ=248 nm) light [37–39]. For measured ASE contribution and divergence of a USP beam $\Theta_{1/2}$=20 μrad the contrast ratios of the short pulse to the ASE can be estimated in the future target irradiation experiments: $CR_Q \sim 10^6$ for energy densities and $CR_I \sim 10^{11}$ for intensities (short pulse of ~ 1 ps is assumed).

2.4. Control of the USP parameters

The following optimization of the laser facility is done which included (i) a correction of aberrations introduced by an optical system with the help of a deformable (adaptive) mirror; (ii) shortening of the USP length and corresponding increase of its peak power by means of compensation of the dispersion broadening; (iii) amplification of the USP train with pulse delay comparable with gain recovery time of the KrF amplifier.

2.4.1. Correction of the USP amplification track aberrations. To diminish USP beam aberrations of the amplification track (**Fig. 2.1**), which contains an ample quantity of optical elements of big size up to 300 mm in diameter, a wavefront correction system is developed and tested. The system consists of two basic elements – the wavefront sensor with a matching telescope and the unimorph deformable mirror with high UV reflectivity. The sensor is developed according to Shack-Hartmann scheme and had an image sensor without protective glass to extend the spectral range to UV region down to the wavelength of ~200 nm. Lens raster of the sensor is fabricated from fused silica with a step of 30 μm. The telescope is also made of fused silica with specially designed objective to minimize spherical and coma aberrations. The telescope had a magnification factor of ~10x and a working aperture of 60 mm. The deformable mirror is manufactured through the unimorph technology with hexagonal arrangement of 59 controlling electrodes. The adaptive optical system is optimized to be used with UV femtosecond laser pulse with the central wavelength of 248 nm.

The third harmonic UV USP generated by Ti:Sapphire front-end (see Subsection 2.2) passed through the e-beam-pumped KrF laser amplifiers and spatial filter. Then the beam is widened up to 5 cm in diameter, collimated and directed to a wavefront correction system. After the adaptive mirror the USP is focused by a quartz glass lens with a focal length of 1 m. The far-field spatial distribution of the laser pulse attenuated down to 3 μJ is distorted because of the long (several tens of meters) path through the air, optical windows of the KrF laser amplifier and spatial filter (**Fig. 2.4.a**). If the wavefront correction system is introduced into the beam, the low–order aberrations are eliminated and far-field pattern is improved (**Fig. 2.4b**).

Dynamic range of the deformable mirror allowed us to add some artificial spherical aberrations. In the course of measurements the phase along the radial direction of the beam is changing according to the Zernike polynomial:

$$\varphi(r) = k\sqrt{5}\left(6(r/a_0)^4 - 6(r/a_0)^2 + 1\right) \times A_Z \qquad (2.1)$$

where e^{-1} beam diameter $2a_0$ is 5 cm in the experiment and the amplitude of the mirror deformations A_Z is varied from 0 to 0.18 μm (**Fig. 2.5**).

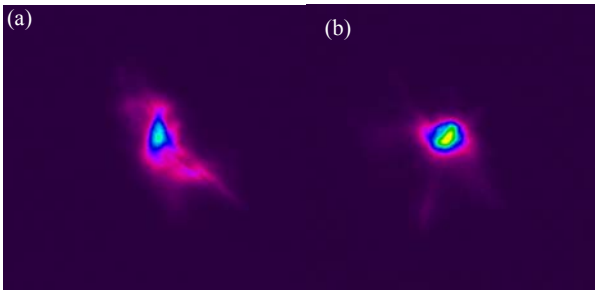

Figure 2.4. Far-field images of the UV pulse (248 nm) passed through the air, e-beam KrF laser amplifier and spatial filter without (**a**) and with (**b**) wavefront correction. The image area is 600 × 600 μm^2

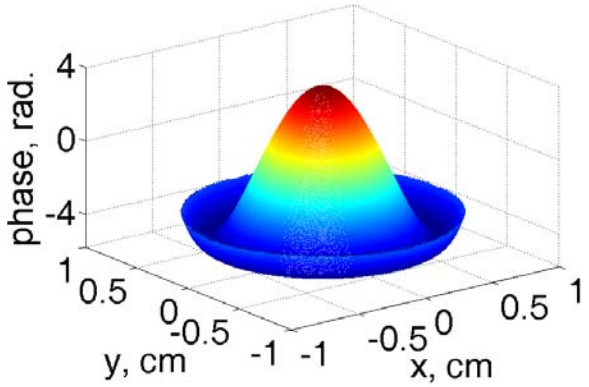

Figure 2.5. Transverse spatial profile of the phase deformations $\varphi(x, y)$, $2a_0$=5cm.

2.4.2. Amplification of chirped pulses. Amplification of USPs with a preliminary negative frequency chirp in e-beam-pumped KrF amplifiers is investigated experimentally in the same layout as in **Fig. 2.1**. The chirp is introduced by a double-pass prism stretcher shown in **Fig. 2.6.** An initial USP of the length of 60–100 fs is stretched up to 1.0–1.5 ps. Unfortunately, energy of the stretched pulse is rather low (~40 μJ) if compared with the maximum energy of the initial pulse (0.4 mJ) because of significant optical loss in the stretcher. After amplification output pulse energy is up to 0.1 J which is somewhat less than that for nonchirped pulses with the same input energy.

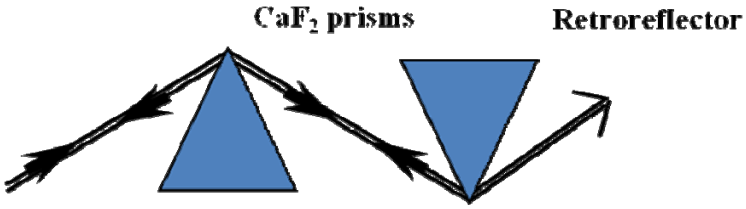

Figure 2.6. Layout a double-pass prism stretcher.

A home-made technique is developed to estimate UV USP length with an autocorrelator based on measurements of a plasma current produced by multi-photon ionization of air in the lens focus. This technique is applied to optimize the stretcher length (a distance between the prisms)

of about 220 cm, which corresponded to the minimal autocorrelation signal after the amplification tract (**Fig 2.7**).

The spectra of USPs which passed the amplification track without (1) and with e-beam pumping of amplifiers (2) are shown in **Fig. 2.8.** Both spectra are normalized to the peak values. The spectral width of the amplified pulse of 0.7 nm (at FWHM) is slightly less than for the non-amplified one (~1.0 nm). The spectrum of the ASE is also measured when input short pulse is blocked, and it is shown in **Fig. 2.9** on the same scale with the amplified USP. It is seen that the time-integrated ASE signal over the pumping time is small enough compared with the USP energy.

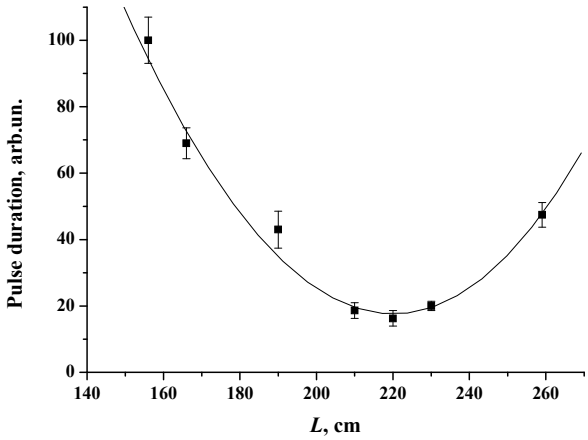

Figure 2.7. Dependence of the pulse length at the output of amplification route on distance between the prisms *L*.

Spectral measurements for a preliminary chirped pulse demonstrated that the output pulse is spatially chirped across the laser beam. This might cause some uncompensated broadening of the output pulse length, which is observed with autocorrelator measurements.

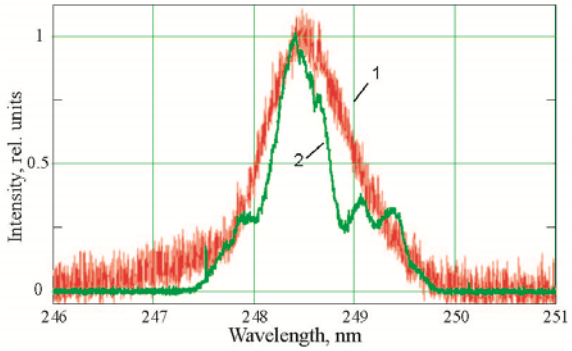

Figure 2.8. Spectra of a USP after amplification tract without (1) and with (2) pumping amplifiers. Both spectra are normalized to their maximums.

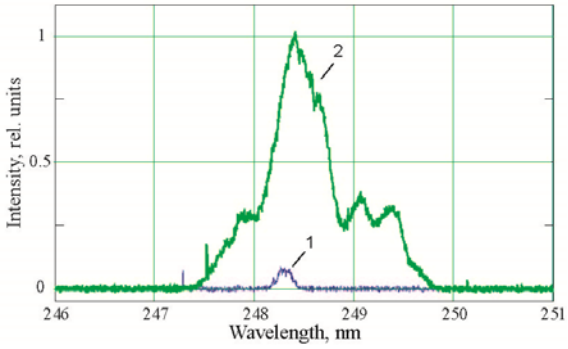

Figure 2.9. Spectra of the ASE (1) and amplified USP (2) on the same scale.

2.4.3. Amplification of the USP train. Experiments are performed on amplification of a train of USPs in two stages of KrF amplifiers in a double-pass configuration (see **Fig. 2.1**). The train is

produced by using a scheme shown in **Fig. 2.10.** Laser beam of the front-end is split by a partially transparent mirror coated on a thin CaF_2 plate and after passing a two-mirror delay line is combined into a single beam of the USP train. Time interval between pulses and their amplitudes could be varied by changing the delay line length and beam-splitter reflection.

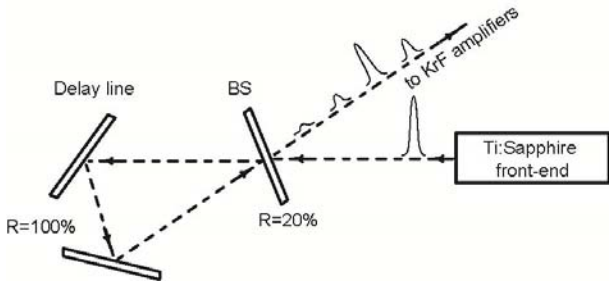

Figure 2.10. Optical scheme to form a train of ultrashort pulses.

Typical oscilloscope traces of the train are shown in **Fig. 2.11**. Signals are time-integrated over ~2 ns (resolution of a photo-detector together with the oscilloscope) A train of USPs (b) can be easily modified into a single USP (a) by blocking radiation transmitted through the beam-splitter. It is seen that for a time delay between pulses 5 ns comparable with gain recovery time (~2 ns), amplification of individual pulses (#1, 2, 3) is different, although all of them are in a time interval corresponding to maximum pumping (c). The reason might be incomplete gain recovery in the gain medium where successive pulses in the train are counter-propagating in amplifiers in the double-pass scheme.

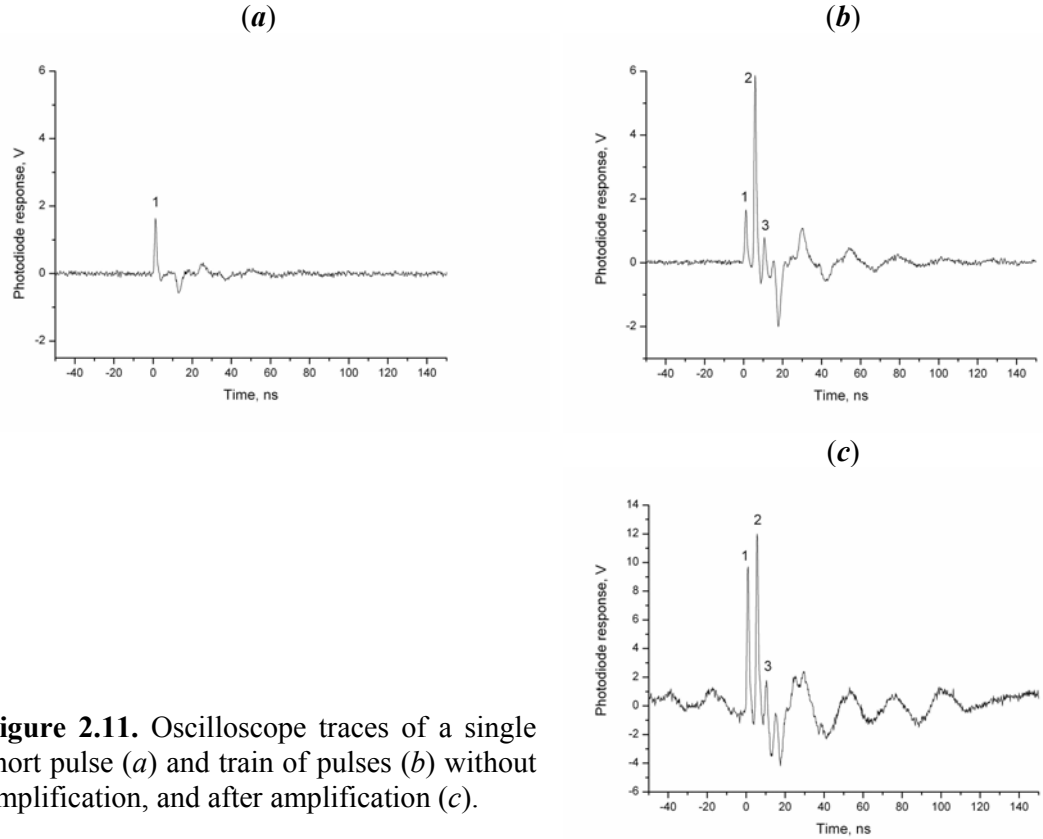

Figure 2.11. Oscilloscope traces of a single short pulse (*a*) and train of pulses (*b*) without amplification, and after amplification (*c*).

2.5. Optimization of the USP amplification scheme

The highest amplification efficiency is to be achieved at maximum amplifier gain which, all other factors being the same, depends on the rate of depopulation of the upper laser level by the ASE. ASE build-up is delayed with respect to the e-beam pump whereas its intensity, direction and divergence are strongly dependent on particular amplification scheme. To find the optimum time of injection of the USP train (in the view of highest amplification efficiency) in each of the two amplifiers, we have performed two measurement series. Within particular measurement series only one of the amplifiers is pumped whereas the other operated in an idle mode, and the time delay between the pump (more exactly, ASE pulse) and USP train is varied with the help of digital delay generator BNC 575 incorporated with Start 248 front-end. **Figure 2.12** shows typical photodetector signals for the case when only BERDYSH preamplifier is pumped. It is seen that photodetector PD1 placed near the amplifier window shows small spikes corresponding to the USP train against the background of long intense ASE pulse (at its leading edge, see **Fig. 2.12**). Here let us remind that one cannot directly compare photodetector signals corresponding to the USP and ASE because photodetectors temporal resolution of ~1 ns is far longer than the USP duration; moreover, photodetectors are somehow saturated by high-intensity USP. Even though the spatial filter almost completely discriminates the ASE, and PD2 shows only USP train, this saturation alone makes it impossible to use the photodetector signal as a marker of amplification efficiency.

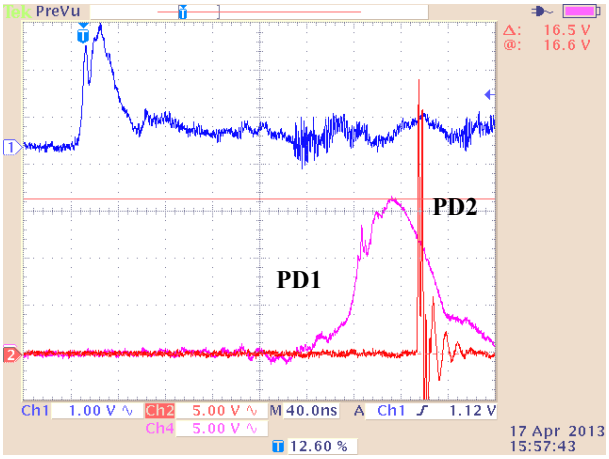

Figure 2.12. Signals from photodetector PD1 (magenta) and PD2 (red). Upper trace (blue) shows the light pulse of the auxiliary KrF laser triggering the spark gaps of the amplifier Blumlein forming lines.

A calorimeter placed in these measurements at a distance of ~10 m from GARPUN amplifier (see **Fig. 2.1**) measured the energy of the USP train. Inlet diameter of the calorimeter just slightly exceeded diameter of the amplified USP beam and the ASE energy even from GARPUN amplifier is negligibly small being at the noise level. The dependence of the USP energy versus time delay for different amplifiers in action is shown in **Fig. 2.13**. By now, it is rather difficult to explain asymmetry in the dependences of **Fig. 2.13**. We did not monitor the pump power time behavior in these experiments and the ASE maximum is not expected to match the pump power peak. The dependences are however of definite practical value in further developing of most efficient scheme for the USP train amplification. Finally, the optimal timing is chosen in experiments with both amplifiers pumped.

To enlarge the USP train energy and improve contrast of USP train against the ASE pedestal we implemented the optical scheme with two extra passes of USP train through BERDYSH amplifier. Two versions of this scheme with single and double passes through GARPUN amplifier are shown in **Fig. 2.14.** As extra passes are delayed by 50 ns relative to the first two passes because of an additional optical length, the optimal timing in BERDYSH amplifier corresponded to the first passes with time delay $\tau = -50$ ns and to successive passes to with $\tau = 0$ ns. In GARPUN the optimal time delay is $\tau = 30$ ns.

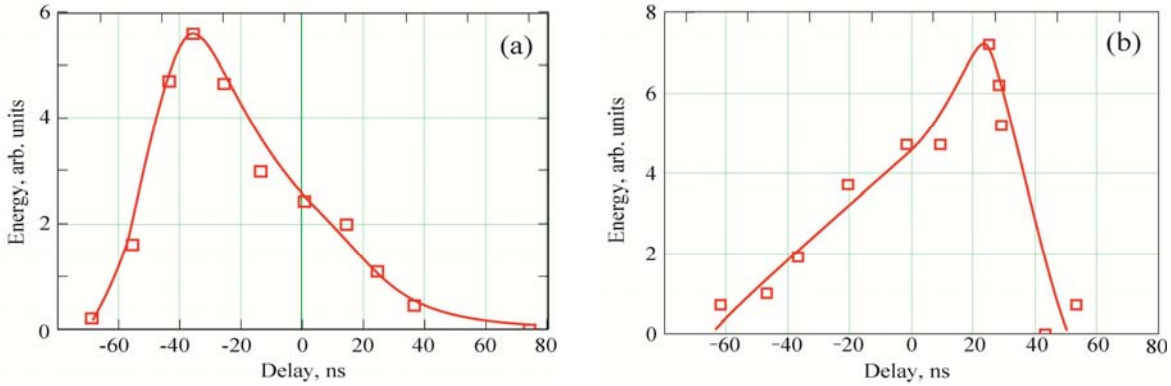

Figure 2.13. Amplifier output energy vs. time delay between the ASE peak and the USP train arrival (first pulse in the train) for operation of only (***a***) BERDYSH or (***b***) GARPUN amplifiers.

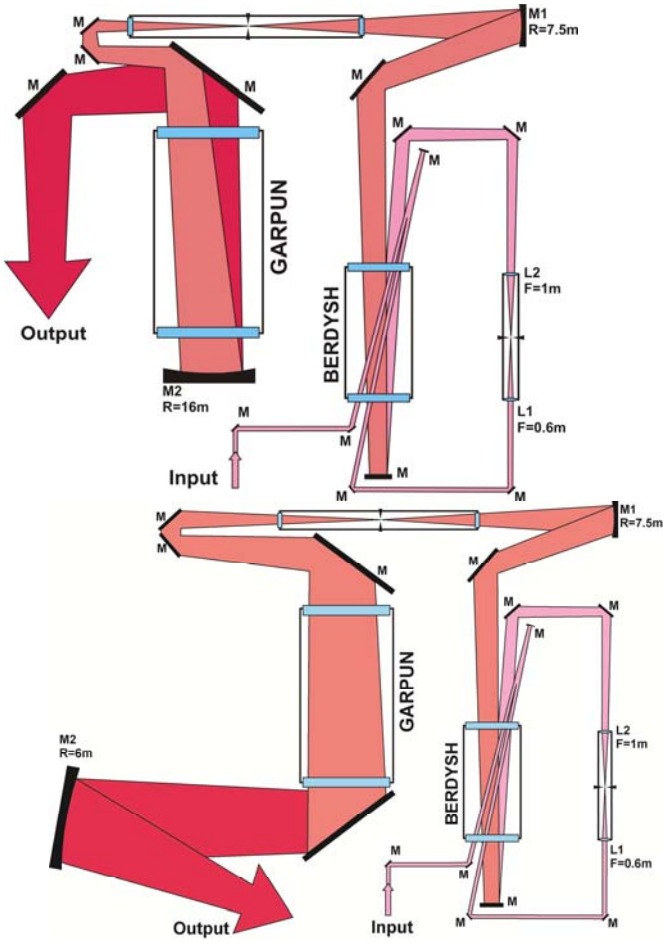

(***a***)

(***b***)

Figure 2.14. Amplification scheme with two extra passes of the USP train through BERDYSH amplifier with (***a***) double and (***b***) single passes through GARPUN amplifier.

A narrow (d ≅ 30 mm) USP beam passes twice the BERDYSH gain medium and then goes through a spatial filter evacuated to fore-vacuum. The focal distances of L1 and L2 lenses and the lengths of spatial filter arms are chosen in such a way that the USP beam going out of the filter diverges and fills up all the aperture of BERDYSH amplifier. The calorimeter measured all the ASE and USP train energy delivered via large-aperture concave mirror M2. Implementation of two extra passes of USP train through BERDYSH amplifier allowed us to employ single pass through GARPUN amplifier. The length of gain medium in GARPUN amplifier thus twice decreases and ASE intensity radically drops down from the initial value which is comparable with the saturation intensity. Hence, small signal gain of $g_0 \cong 0.06$ cm^{-1} averaged over amplification length, with suppression by the ASE taken in to account is higher in the single-pass scheme than that in the double-pass scheme ($g_0 \cong 0.03$ cm^{-1}) [15], which makes it possible to obtain higher USP energy.

Figure 2.15 presents the total energy measured by the calorimeter versus the USP train input energy for the "conventional" amplification scheme with two passes through BERDYSH and GARPUN amplifiers, see **Fig. 2.1**.

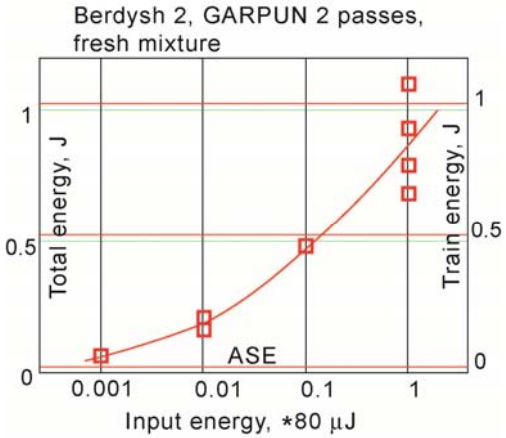

Figure 2.15. Total energy measured by the calorimeter (left y-axis) vs. injected USP train energy for the scheme with two passes through BERDYSH and GARPUN amplifiers. Right y-axis shows amplified USP train energy.

The total energy (left y-axis) is composed of the amplified USP train (right y-axis) and ASE energy. The latter measured without injection of the USP train is only a few percent of the total energy and is shown by a thin red line (zero horizontal graticule line is related to the right y-axis). Here and thereafter, unless otherwise specified, all the measurements are carried out with "fresh" (newly-prepared) gas mixtures in the amplifiers.

The dependences similar to that shown in **Fig. 2.15** are measured also for the optical schemes with two extra passes of USP train through the amplifiers under study. **Figure 2.16** presents output versus input dependence for the case of 4 passes through BERDYSH amplifier. The calorimeter is set after the second spatial filter and measures the energy delivered to the input of GARPUN amplifier. The ASE energy of ~3 mJ detected in this scheme is very low.

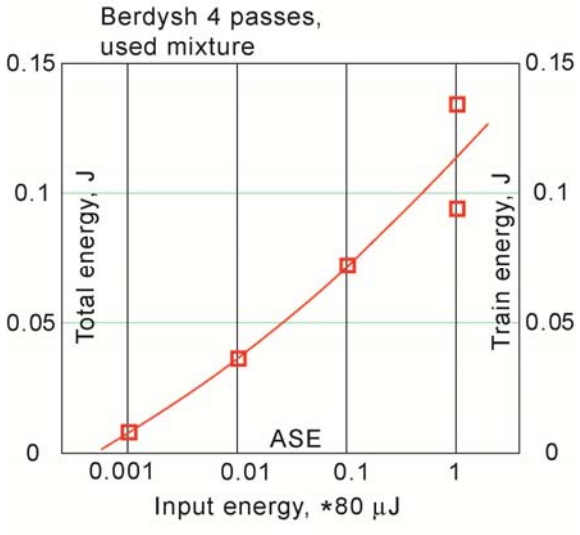

Figure 2.16. Total output energy after BERDYSH amplifier (left y-axis) vs. injected USP train energy for the scheme with 4 passes through BERDYSH amplifier. Right y-axis shows amplified USP train energy.

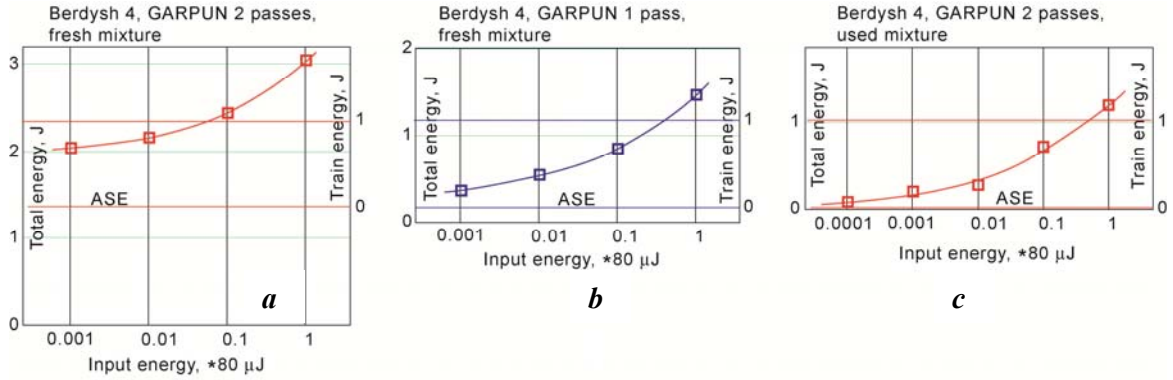

Figure 2.17. Total output energy after BERDYSH and GARPUN amplifiers (left y-axes) vs. injected USP train energy for the schemes with (***a***) 4 passes through BERDYSH and 2 passes through GARPUN amplifiers (**Fig. 2.12*a***); (***b***) 4 passes through BERDYSH and 1 pass through GARPUN amplifiers (**Fig. 2.12*b***); and (*c*) 4 passes through BERDYSH and 2 passes through GARPUN amplifiers filled with "used" (long time served) gas mixtures (**Fig. 2.12*a***). Right y-axis shows amplified USP train energy.

Figure 2.17 compares the output versus input dependences for the cases presented in **Fig. 2.14**. One can see that all the dependences are similar to each other. There is a kind of saturation when one order of magnitude increase in the input energy leads to increase in the output energy by a factor of 1.5 – 2 throughout the whole range of varying input energy (3 – 4 orders). Such behavior is difficult to explain only by saturation of the gain medium. More likely, it is a result of joint action of the gain medium saturation and nonlinear absorption of the USP train energy in the optical scheme components and air. It is measured that, while passing even a high-quality 30-mm thick CaF_2 window, amplified USP train loses up to 50 % of its energy. It is thus greatly advantageous to reduce the number and thickness of optical components in amplification scheme later on.

In the scheme with two passes through GARPUN amplifier, contribution of the ASE into the total energy is about 50%, see **Fig. 2.17*a***. With the use of a single pass through GARPUN amplifier, the ASE contribution decreases by nearly an order of magnitude, see **Fig. 2.17*b***, whereas USP train energy is just slightly reduced. Similar behavior occurs when gas mixture in the amplifiers degrades, see **Fig. 2.17*c***. Both addition of another pass through GARPUN amplifier and increase in the gain due to "refreshing" working gas mixture result in minor increase in the USP train energy, which is in saturation mode, and great increase in the nonsaturated ASE energy.

In conclusion, the optimal injection time of the USP train into KrF amplifier chain is found and various amplification schemes are compared to obtain the maximal USP energy and the lowest ASE level. In this regard 4 passes in BERDYSH and a single pass in GARPUN seem to be the most promising for further experiments.

3. Combining of femtosecond and nanosecond pulses in KrF amplifiers

This section is devoted to the development of an optical scheme which enables us to obtain combined high-energy UV laser pulses at GARPUN MTW KrF laser facility in the injection-controlled regime. By itself such operation mode has been routinely used at the GARPUN KrF laser facility for decades with 20-ns KrF master oscillator pulse being injected into the unstable resonator cavity [14]. In that case, the injected pulse intensity is many orders of a magnitude lower than the output radiation and no significant temporal modulation is observed. Nevertheless, it effectively controlled the angular and spectral distribution, as the lasing started from the injected radiation rather than from spontaneous emission. By injecting a USP with high peak intensity exceeding in many times the intensity of a quasi-steady oscillations one can expect a strong modulation of the output radiation. Possibility of the USP amplification against a background of long pulses amplification in KrF gain medium is firstly considered in the paper [36], some numerical simulations are carried out in [15] but no experimental realizations have been done up to date.

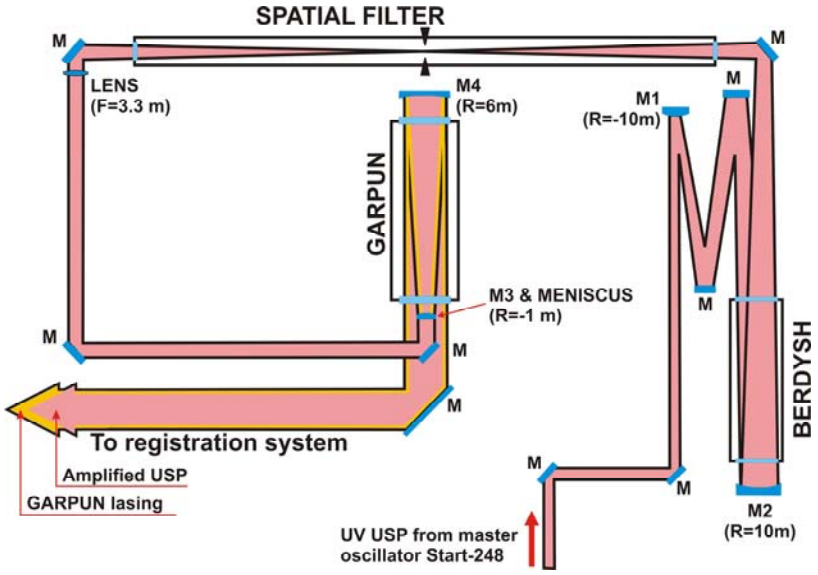

Figure 3.1. Layout of experiments on combined (long & short) pulse generation.

Figure 3.1 shows a layout of present experiments being published in papers [23–29]. The UV USP of 0.5-mJ energy, 60-fs duration and with λ=248.4 nm wavelength are generated at the frequency-tripled Ti:Sapphire front-end facility "START-248 M". They are first amplified in a double-pass scheme in the Berdysh e-beam-pumped KrF pre-amplifier up to 20-mJ energy. After passing 6-m length spatial filter USP laser beam is collimated by the lens (F=3.3 m) into a parallel beam and directed to the main GARPUN amplifier, which is equipped by a confocal unstable resonator with magnification factor M=6 formed by a back concave HR mirror (R=6 m) and partially-transparent convex mirror deposited upon the meniscus lens. The foci of both the concave mirror and meniscus are matched being equal to 0.5 m.

Typical oscilloscope traces of a free-running oscillation pulse (when USP injection is blocked) and of the combined laser pulse (when USP injection is open) are compared in **Figs. 3.2*a*, 3.2*b***. The upper trace (blue) represents a side-wall spontaneous emission; the middle trace (red) is output radiation, and the lower trace (pink) is the injected USP signal. The side-wall emission pulse width is 120 ns at FWHM which corresponds to the e-beam pumping time and accordingly the gain in the medium. It takes about 30-40 ns for the free-running oscillations are formed in the resonator cavity. The injected USP radiation is amplified in the regenerative manner while it is running multiply in the resonator cavity being superimposed with free-running oscillations. It should be noted that the USP amplitudes in oscilloscope traces are in ~10^3 times less than the real ones because of a limited temporal resolution of a vacuum photodiode (~1 ns) which integrated USP pulses (being estimated as ~1 ps [16, 17]).

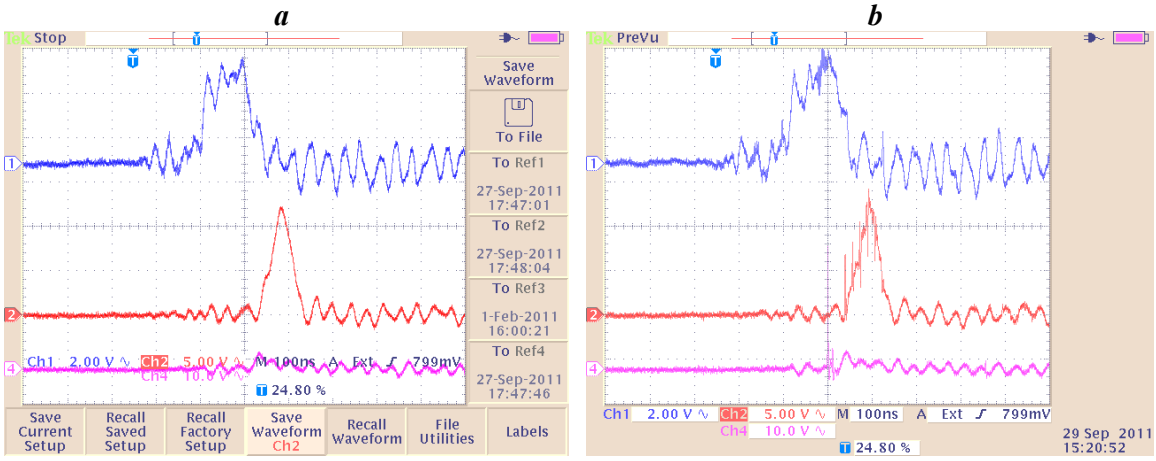

Figure 3.2. Side-wall spontaneous emission in the GARPUN regenerative amplifier (upper oscilloscope trace), output laser radiation (middle trace), and injected radiation (lower trace) for a case of free-running oscillations (***a***) and with USP injection (***b***). Time scale is 100 ns/div.

It is also seen in **Fig. 3.2*b*** (see also **Fig. 3.4** with larger time scale) a gradual decrease in the USP amplitudes during the time. Besides of the USP spikes the holes appear in a quasi-steady oscillation pulse form. The probable reason is that the USP is not perfectly injected inside the resonator cavity along its axis. In this case the successive USP round trips would deviate off the resonator axis far and far and therefore go away from an aperture of the photodiode being set in a near field of the output radiation. Such effect is confirmed in the experiment where the photodiode is set behind a pinhole in the focus of F=8 m mirror. In the case if the USP injection is slightly misaligned, the photodiode measured only the first USP while the others are fully discriminated by the pinhole. Another reason might be that increasing free-running oscillations are depleting a population inversion to a greater extent thus affecting on

amplification of the USP. In its turn, the USP is also depleting the gain, which is evidently embodied in the holes seen in the pulse form.

An important question for application of the combined laser pulse is how to increase energy of the USP train in a competition with quasi-steady oscillations. One of the ways is to increase the USP power at the input of GARPUN amplifier by arranging additional pass of the initial front-end pulse in Berdysh pre-amplifier. Another way is to reduce an interval between the USP in KrF gain medium down to the gain recovery time $\tau_c \sim 2$ ns. For a fixed length of the resonator cavity this can be done by injecting a short train of the USP preliminary formed after the front end. We used such USP multiplexer earlier (see **Fig. 2.8**, Subsection 2.2). In present experiments, it is slightly modified by using four mirrors instead of three in the scheme (**Fig. 3.3**). For the delay line length of 160 cm and beam-splitter reflection of 30% the USP train is produced with a time interval between pulses of about 5.3 ns and a ratio of their amplitudes 3:5:1.5:0.5…

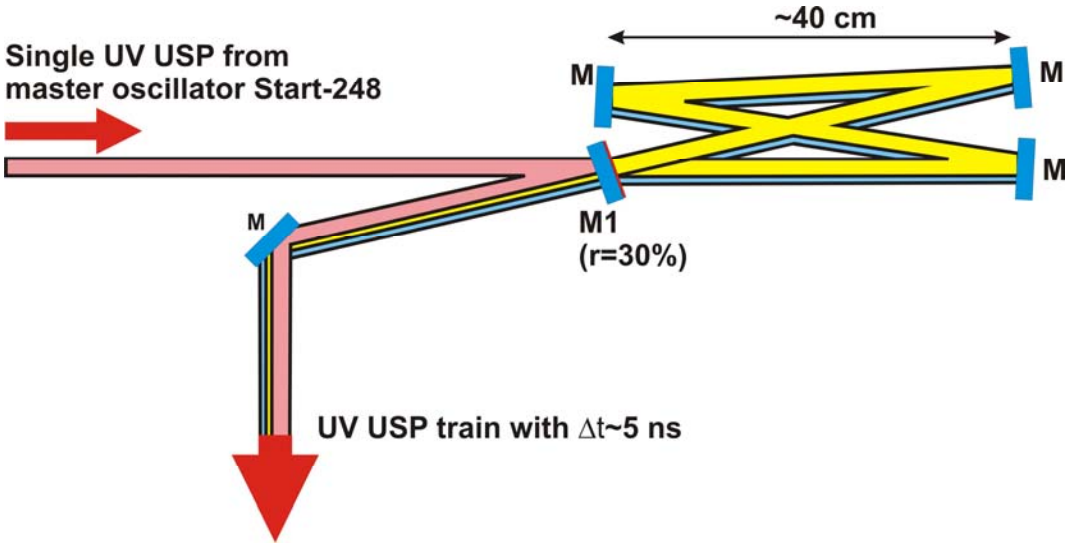

Figure 3.3. Optical scheme to form a train of the USP with a time interval Δt~5 ns.

The effect of the injected train is demonstrated in **Fig. 3.4** in which it is compared with the free-running oscillations (when USP injection is blocked) and injection of the single USP (when USP delay line is blocked). A strong modulation of the output radiation is achieved since the very beginning and during almost a full pulse width.

Output energy of the combined laser pulses is measured for different reflections of the meniscus coating mirrors. The highest radiation energy ~30 J is obtained for the reflection R=80% but the pulse modulation is rather low. For R=10% and 30% meniscus the energy is about 20 J and the highest modulation is observed. For reflection R=4% the energy decreased down to 5 J. It is difficult to separate precisely a part of energy contained in the amplified USP train. But if taking into account that the energy is approximately the same both in a free-running regime and with USP injection for obtained pulse forms, one can believe that a significant part (tens percents) of the total laser energy is transformed from free-running oscillations into the amplified USP train under the injection of the train with 5-ns interval. One can estimate the maximum peak power of the USP in the train of 20 pulses as ~0.2-0.3 TW if assumes pulse duration ~1 ps. Indeed duration the USP is growing on for the successive pulses because of group velocity delay in the CaF_2 windows of GARPUN amplifier in the course of round trips in the resonator cavity.

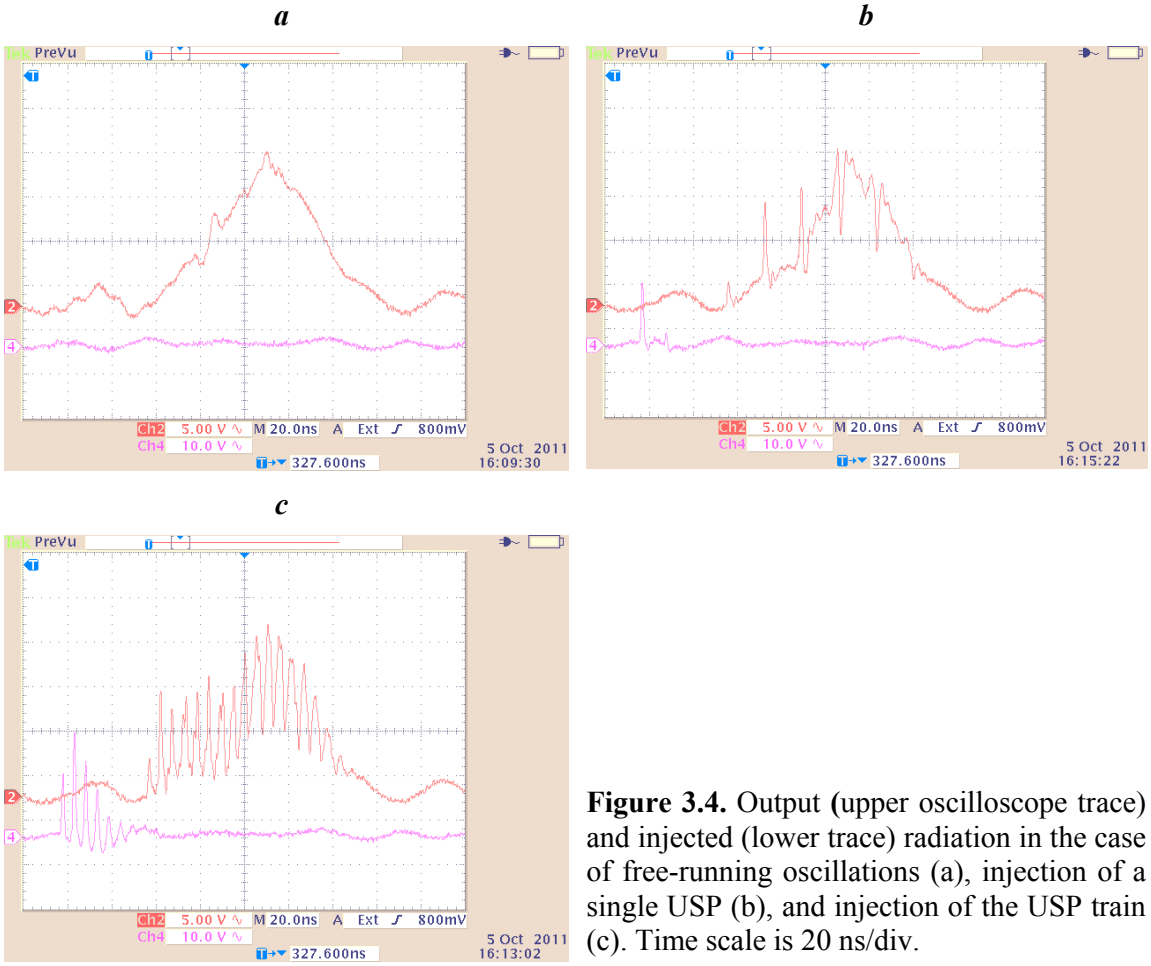

Figure 3.4. Output (upper oscilloscope trace) and injected (lower trace) radiation in the case of free-running oscillations (a), injection of a single USP (b), and injection of the USP train (c). Time scale is 20 ns/div.

By introducing a negative frequency chirp into the initial USP in the manner described in Subsection 2.2 one can obtain different evolution of the USP time width in the train. When further propagating in the air these chirped USP should be compressed (temporally focused) at various distances. Variable space focusing of the USP train in different points of a trajectory can be also implemented by using slightly unmatched injection or non-confocal resonator.

4. Filamentation of the USP UV laser beam in atmospheric air

Peak power of a single USP produced at GARPUN-MTW facility attains $P \approx 1$ TW for output laser energy up to 1 J and pulse duration ~1 ps. This value exceeds by four orders of magnitude the critical filamentation power $P_{cr} = 3,77\lambda_0^2 / 8\pi n_0 n_2 \approx 0.1$ GW, where $\lambda_0 = 248$ nm is the laser wavelength in vacuum, $n_0 \approx 1$ and $n_2 = (8–10)\cdot 10^{-19}$ cm^2·W^{-1} are, correspondingly, a linear and nonlinear Kerr refraction indexes [37–39]. Compared with $P_{cr} \approx 3$GW for IR radiation of Ti:Sapphire laser (λ_0~800 nm, $n_2 = (2.8–3.0)\cdot 10^{-19}$ cm^2·W^{-1}) it is rather low, and some new physical effects are observed in present experiments, e.g. linear (geometrical) laser beam focusing in the case of multiple small-scale filamentation of a supercritical UV USP. The latter is initiated by a block structure of CaF_2 windows of the final KrF amplifier that introduced phase modulation at block boundaries [16, 17]. Oppositely, for terawatt-level IR radiation a slightly convergent (or even collimated) laser beam collapses before the focal plane to a bundle of filaments, which propagates over hundreds of meters [37–39]. In this extended nonlinear focusing region, nonlinear Kerr self-focusing compensates the divergence caused by diffraction or defocusing of radiation by plasma. This circumstance hampers the maintenance of filament-

induced air ionization by an additional longer nanosecond UV or visible-range laser pulse, which is proposed to photodetach electrons captured by oxygen molecules [40]. In fact, to produce a long-lived and extended plasma channel by combined radiation one needs to use two separate laser systems to generate the USP and a long pulse, as well as complicated electronic and optical schemes to match both pulses temporally and spatially. Linear focusing of a long pulse can be adjusted to self-focusing of the USP by some kind of conic optics (axicons) [40–42].

4.1. Filamentation of the terawatt USP UV laser beam

One of obvious advantages of the hybrid Ti:Sapphire/KrF GARPUN-MTW laser system is its capability to generate amplitude-modulated UV radiation combined of amplified train of picosecond USPs and a 100-ns free-running laser pulse (see Section 3). Focusing capabilities of combined UV radiation have not been comprehensively investigated in previous papers [23–29]. In present studies of multiple filamentation of powerful UV USP radiation attention is paid to the following issues: (i) if initially filamentous USP beam is geometrically focused, is the filametation structure kept behind the focus, where air ionization mostly takes place; (ii) how does the USP beam behave in different focusing conditions and at various laser powers; (iii) are there any distinctive features for the filamentation of the USP train.

Figure 4.1 shows a layout of experiments on filamentation of powerful UV USP radiation in air**.**

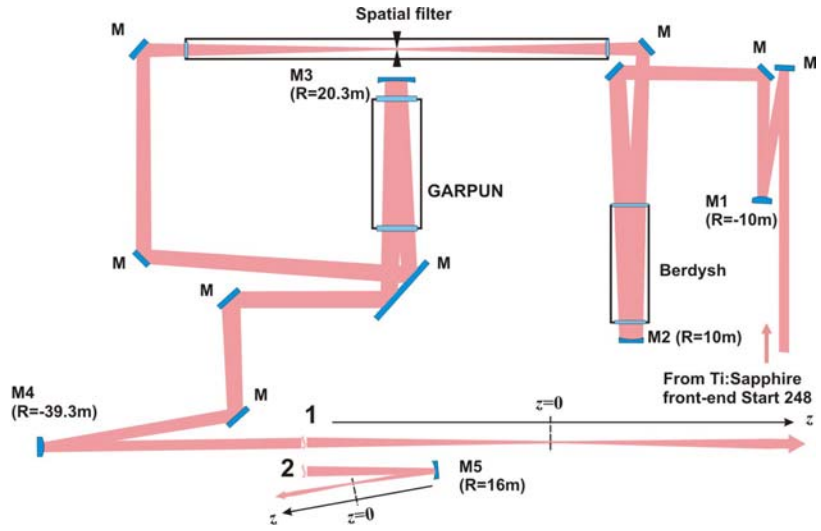

Figure 4.1. Layout of experiments on investigation of powerful USP radiation at GARPUN-MTW laser facility.

Typical oscilloscope traces of the USP train with a time interval $\Delta t \approx 5$ ns or a single USP after double-pass amplification in successive preamplifier and the main amplifier are shown in **Fig. 4.2**. Note once again that the USP duration of about 1 ps is integrated by a photodiode over ~1 ns. To obtain a single USP the delay line of the multiplexer (see Section 3) is blocked. This did not change the first pulse in the train, whose energy is up to 0.3 J, while completely removed the others. Output radiation is formed into a slightly convergent laser beam by an all-reflecting mirror system consisting of the back concave M3 mirror of the final amplifier and convex M4 mirror (Layout 1 in **Fig. 4.1)**. It is further transported by several flat turning mirrors (they are not shown in **Fig. 4.1**) from the laboratory room into a building corridor, whose length is about

100 meters. The focal length counted off from the M4 mirror is varied from $F\approx100$ m to $F\approx60$ m by changing the distance between M3 and M4 mirrors. When additional M5 mirror is installed in the Layout 2 at 32 m behind M4 mirror (which is set in a position with $F\approx60$ m) the resulted focus laid at $F\approx6.75$ m distance from M5 mirror. Radiation distribution in different cross sections along the beam is measured by fluorescence imaging of a K8 glass plate under UV irradiation, which is registered by a CCD camera.

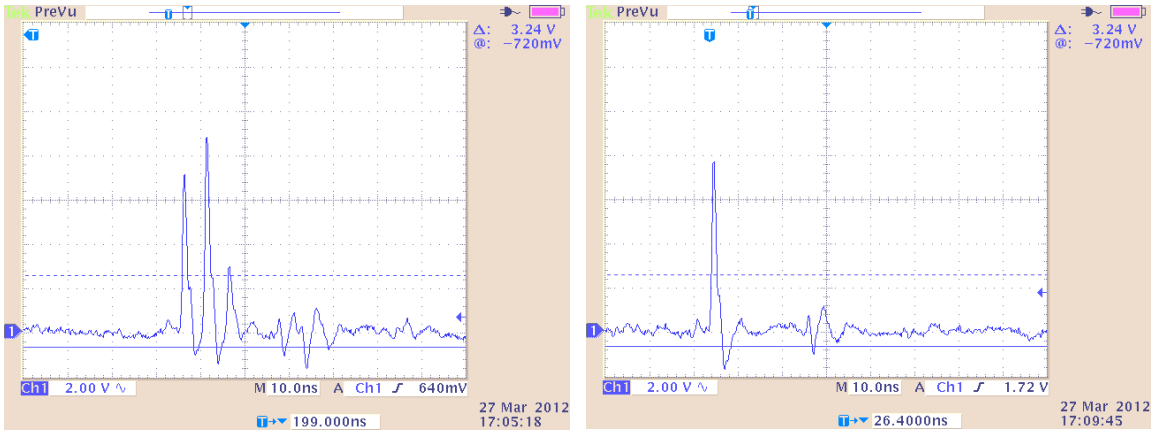

Figure 4.2. Typical oscilloscope traces of the USP train (left) and single pulse (right) after double-pass amplification. Time scale is 10 ns/div. The USP temporal width is broadened by a photodiode.

Small-scale filamentation of the output radiation induced by CaF_2 windows is clearly observed at little distance from the final amplifier. For example, intensity distribution for a single USP with energy E_1=0.23 J and peak power P_1=0.23 TW=2.3×10$^3P_{cr}$ at 25 m distance from mirror M4 (75 m before the focus F=100 m) contains hundreds of bright spots, i.e. filaments, which are grouped along the boundaries of the window blocks (**Fig. 4.3**).

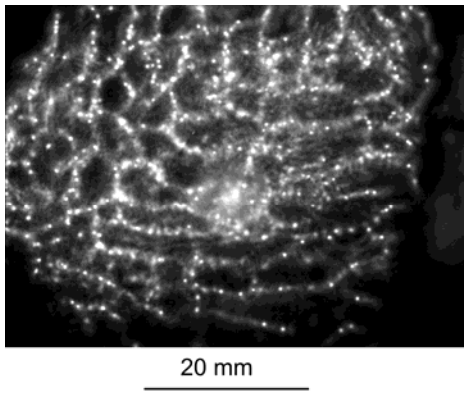

Figure 4.3. Intensity distribution for a single USP with energy E_1=0.23 J (peak power P_1=0.23 TW) at 75 m distance before the focus F=100 m.

Typical diameter of the filaments is between 300 and 500 microns. When approaching the focus, an effective radius of the USP beam (defined as geometrical mean between two mutually perpendicular dimensions of the whole spot) decreases as shown in **Fig. 4.4.** Peak power for this graph is in the range P_1=0.2÷0.25 TW. Correspondingly, an areal density of filaments increases and their distribution becomes more uniform over the cross-section. Because of limited length of the propagation track in the corridor for such focusing we did not trace beam radius and filaments development behind the focus.

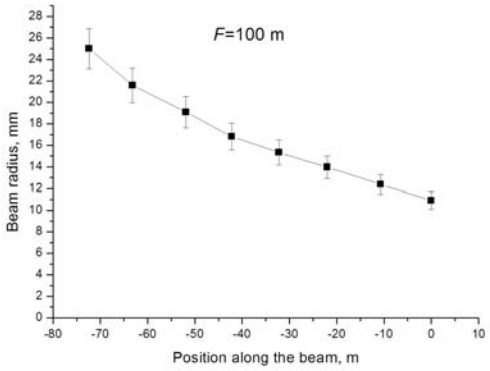

Figure 4.4. Effective USP beam radius along focusing length F=100 m. Peak power of the USP is P_1=0.2÷0.25 TW. Axis z is directed along propagation of radiation with z=0 lying in the focus.

To study how the USP beam behaves in front and behind the focus, the focusing system is turned to shorter focal length F=60 m. Intensity distributions for single USPs of different energies at 22.5 m distance in front of the focus F=60 m are shown in **Fig. 4.5.** With decreasing the USP energy total amount of filaments gradually decreases (***a-d***) and at E_1=0.004 J (P_1=0.004 TW=40P_{cr}) they merge together resulting in light intensity nonuniformities of larger size ~1 mm (***e***).

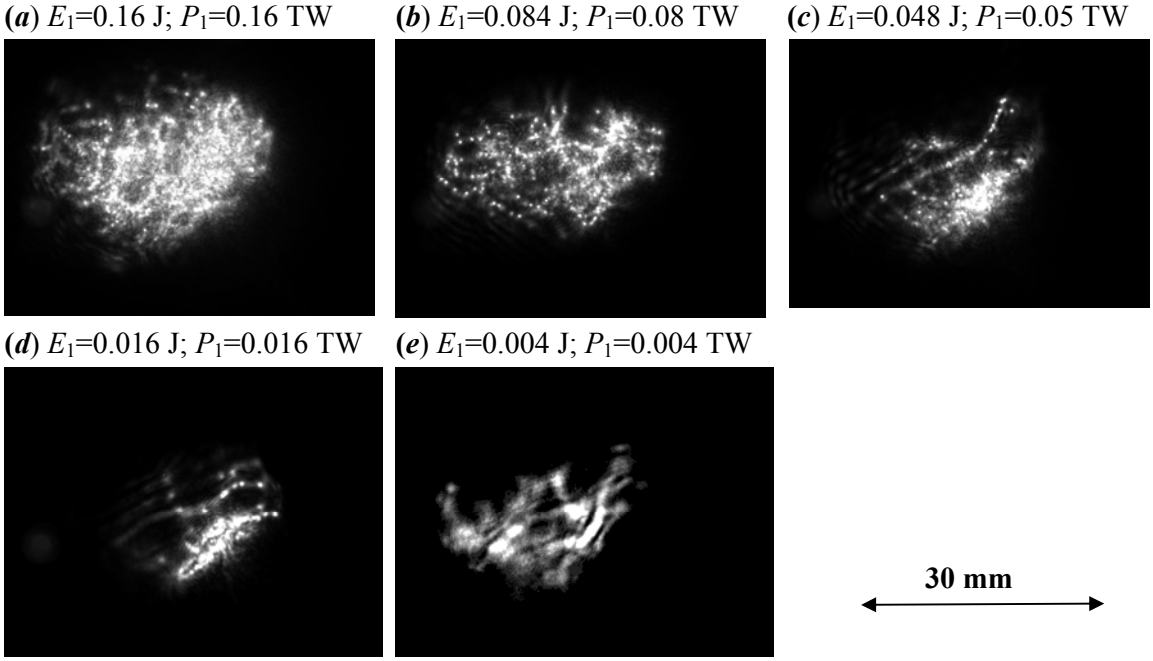

Figure 4.5. Intensity distribution for a single USP at 22.5 m distance before the focus F=60 m for different USP energies.

Intensity distribution in the focal plane for a single USP with energy E_1=0.2 J (P_1=0.2 TW=2×10^3P_{cr}) at the same focusing (F=60 m) is shown in **Fig. 4.6.** The density of filaments is so high that they are almost fully overlapped in the focal spot that shapes a circle. In general, even though macroscopic USP beam distribution in the near-field is not symmetrical (**Figs. 4.3, 4.5)**, in the far-field and even at rather long distances behind the focus it becomes almost circular.

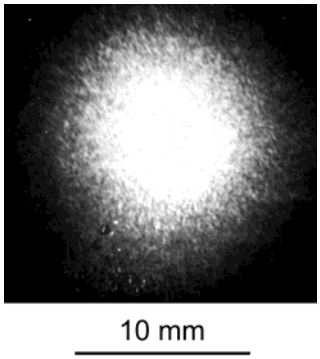

Figure 4.6. Intensity distribution for a single USP in the focus F=60 m for the USP energy E_1=0.2 J (P_1=0.2 TW).

In the expanding beam behind the focus filamentous structure reappears, although it is not as clear as before the focus (**Fig. 4.7)**. Beam diameter and amount of filaments decrease at lower USP energy while typical diameter of light nonuniformities increases 2 - 3 times.

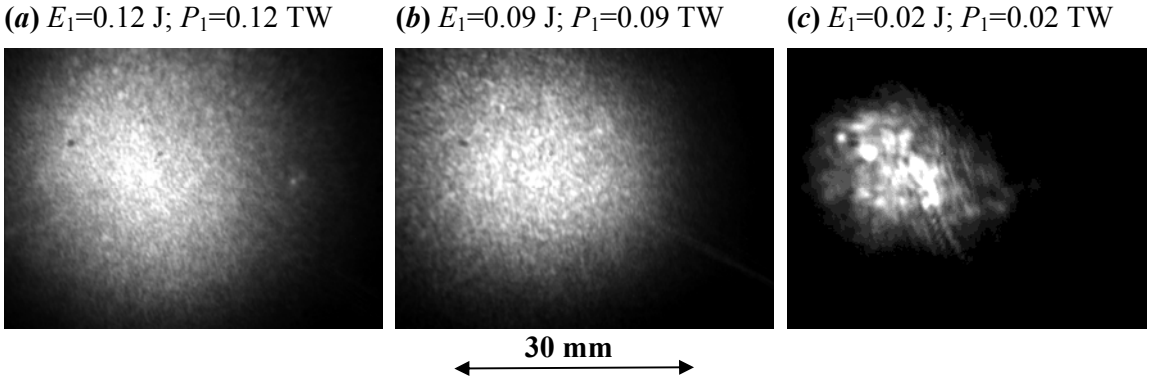

Figure 4.7. Intensity distribution for a single USP at 37.5 m distance behind the focus F=60 m for different USP energies.

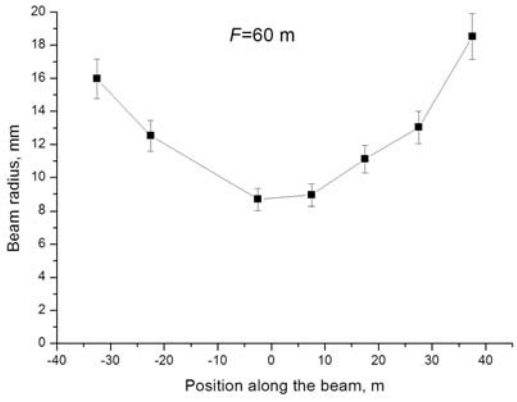

Figure 4.8. Effective beam radius along the USP propagation for F=60 m. Peak power of the USP is P=0.15÷0.2 TW. Axis z is directed along propagation of radiation with z=0 lying in the focus.

The mean radius of the USP beam in dependence on propagation distance (**Fig. 4.8.**) obeys a linear focusing law with the caustic waist radius ~9 mm, which corresponds to the beam angular divergence of ~1.5×10^{-4} rad. It is determined mostly by rather poor optical quality of

the windows of laser amplifiers. The similar filamentation behavior is observed for the USP beam focusing with F=6.5 m (Layout 2 in **Fig. 4.1**). Note that **s**uch focusing geometry of the combined radiation is used in further experiments on HV electric discharge guiding (Section 8). In present experiments, the effect of the USP train on beam filamentation is also studied. Intensity distributions for a single USP and USP train are compared in **Fig. 4.9** in left and right-hand columns. For a single USP energy and power are designated as E_1 and P_1, correspondingly. For the USP train total energy $E \approx E_1+E_2+E_3$, where individual USP energies and peak powers are in the ratio 3:5:1.5:0.5 (**Fig. 4.2**).

Far before the focus macroscopic distributions of filaments over a cross-section of the laser beam for the USP train and single USP are similar (see ***a*** and ***b*** for comparison). However, multiple small-size filaments of a single USP distribution merge into light intensity nonuniformities of larger size or so-called filament clusters in the case of the USP train. This effect becomes more pronounced when approaching the focus (***c-h***). In addition, the most intensive filament clusters are formed in the central part of almost circular beam cross section. At larger distances behind the focus multi-filamentous structure reappears with the same tendency towards clusterization of individual filaments for the USP train.

a z=-3.45 m; E_1=0.19 J; P_1=0.19 TW

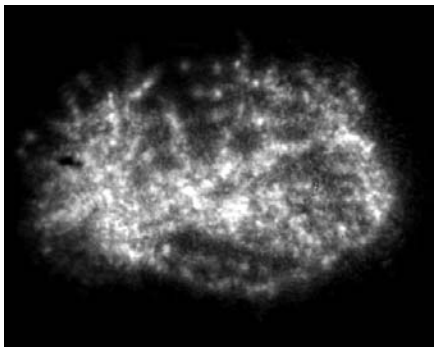

20 mm

b z=-3.45 m; E=0.43 J

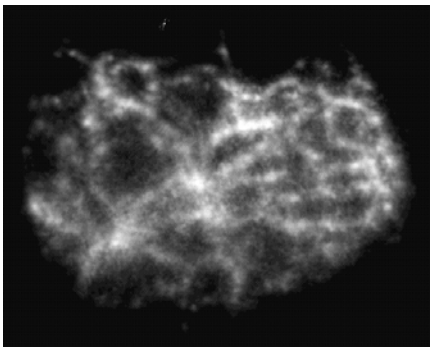

20 mm

c z=-0.5 m; E_1=0.16 J; P_1=0.16 TW

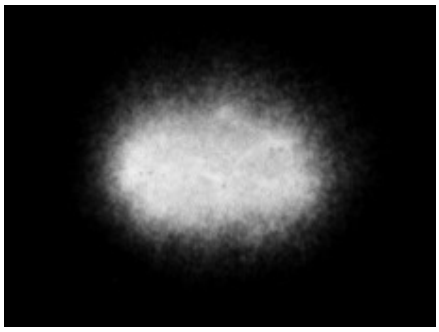

5 mm

d z=-0.5 m; E=0.46 J

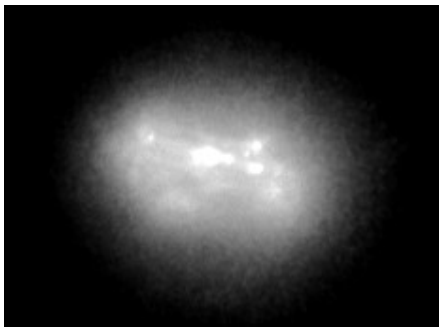

5 mm

e z=-0.2 m; E_1=0.17 J; P_1=0.17 TW

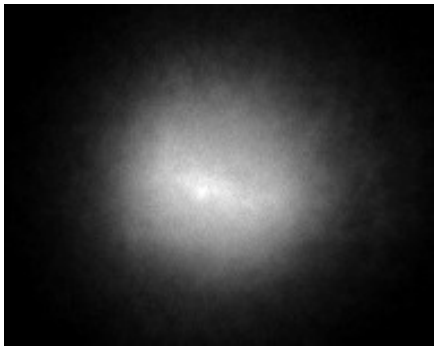

2 mm

f z=-0.2 m; E=0.51 J

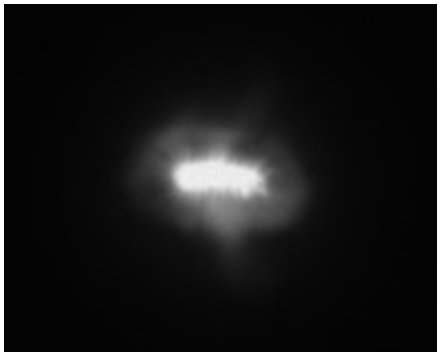

2 mm

g z=0; E_1=0.15 J; P_1=0.15 TW

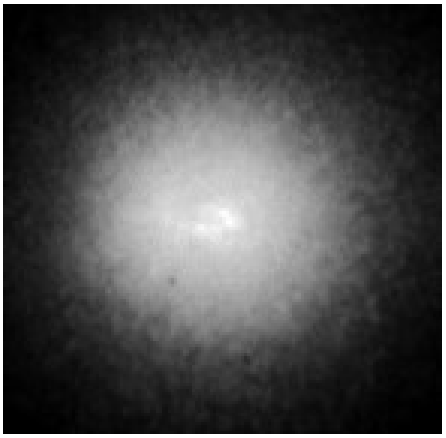

2 mm

h z=0; E=0.30 J

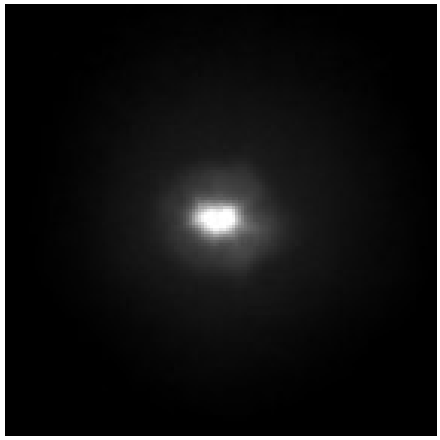

2 mm

i z=0.20; E_1=0.15 J; P_1=0.13 TW

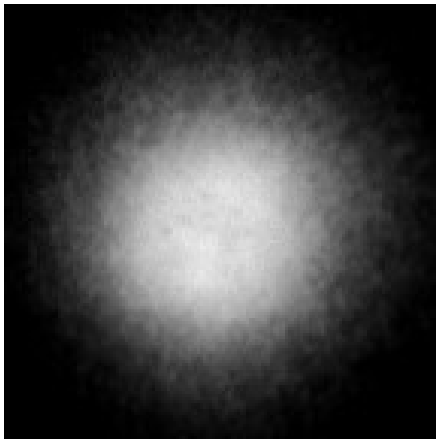

2 mm

j z=0.20; E=0.30 J

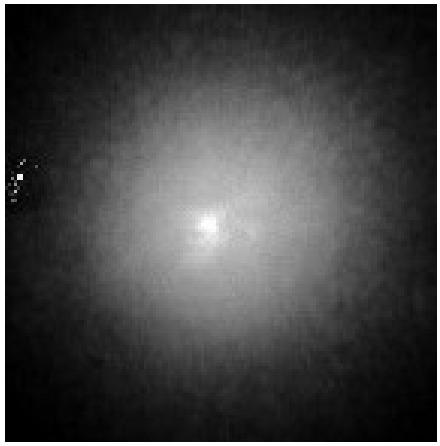

2 mm

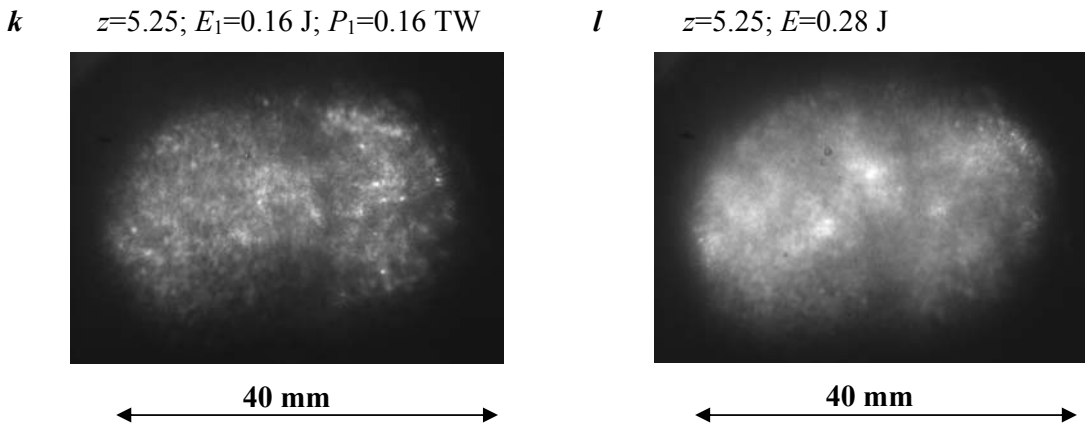

Figure 4.9. Intensity distribution for a single USP (left) and USP train (right) along the laser beam propagation for F=6.75 m focusing. Values of z are counted off from the focus point in the direction of radiation propagation.

For shorter focal length F=6.75 m the mean radius of the USP beam demonstrates evident linear dependence on distance which is counted off from the focus (**Fig. 4.10**).

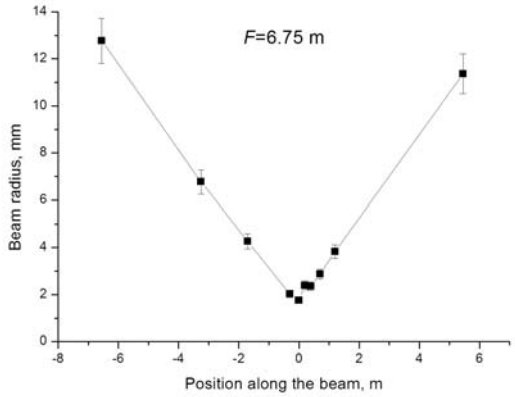

Figure 4.10. Effective beam radius along the USP propagation for F=6.75 m. Peak power of the USP is P=0.15÷0.2 TW. Axis z is directed along the propagation of radiation with z=0 lying in the focus.

The caustic waist radius of ~1.8 mm corresponds to the beam divergence of ~2.6×10^{-4} rad. Compared with previous measurements (F=60 m) it is 1.7 times higher being inversely proportional to the USP beam size at focusing mirrors in Layouts 1 and 2.

4.2. Filamentation of UV and IR femtosecond USP governed by variable wavefront distortions via a deformable mirror

The objective is to study experimentally and numerically filamentation of focused femtosecond laser pulses governed by variable wavefront distortions including spherical aberrations introduced by a deformable mirror. The simulations are aimed at understanding of how the phase shape introduced by the mirror deformation leads to increase in the filament and plasma channel length [33].

4.2.1. Experiment. Experimental setup consisted of Ti:Sapphire laser facility with the central wavelength of 744 nm and the pulse duration of 100 fs. The first series of experiments is conducted with UV USPs. To obtain the UV USP the output IR USP is directed to the third harmonic generator made of KDP/BBO crystals. The radiation with energy of about 0.2 mJ at pulse duration of 100 fs is focused with the lens, and the laser beam profile is registered with a CCD matrix Spiricon SP620 at different distances from the geometrical focus position. The beam diameter is determined for each of the registered images (**Fig. 4.11**). Even though the peak power of the UV laser pulse exceeded the critical power ~ 0.1 GW by an order of magnitude, only a single filament is formed in the experiment. The confined propagation is characterized by the length along which the transverse beam size remains fairly constant. The plasma diameter obtained in our experiment is within the typical range 20 – 100 microns. As a criterion of the confined propagation regime we choose the characteristic hot spot diameter below or equal to 55 μm, above which the width of the filament formed without spherical aberrations starts to increase more rapidly and confined propagation no longer exists.

The longitudinal distance along which the filament diameter remains less than the characteristic diameter is indicated by the dashed horizontal line in **Fig. 4.11**. Note that the length of the filament produced by the beam with spherical aberrations is almost twice longer as compared to the filament length created by the beam without aberrations (compare the two arrow-marked horizontal lines in **Fig. 4.11)**.

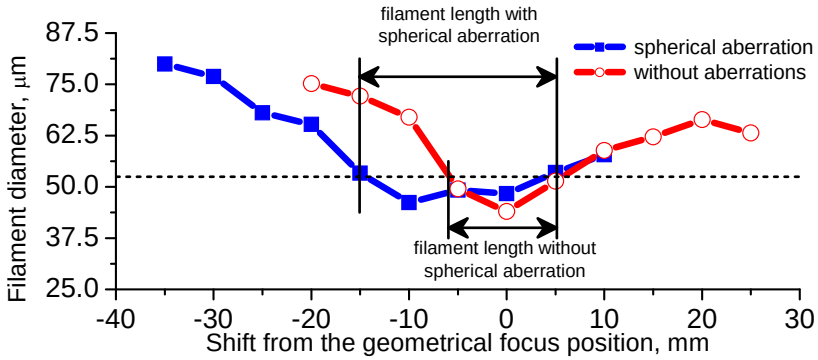

Figure 4.11. Beam diameter measured by CCD camera at 248 nm for different distances from the geometrical focus position corresponding to 0 mm. The horizontal dotted line shows the level of 55 μm, while the two arrow-marked horizontal lines indicate the filament extension with (squares) and without (circles) spherical aberrations

The second series of experiments is carried out with IR laser pulses centered at 744 nm. After the compressor the laser beam is expanded with the off-axis telescope up to the diameter of 30 mm. Further on, the radiation is sent to the wavefront correction system (**Fig. 4.12**). After the wavefront corrections and introduction of additional spherical aberrations, the radiation is focused into the air by means of the lens with the focal distance of 70 cm. The laser energy is 2 mJ that is controlled by an energy meter situated directly behind the lens. For all the laser shots only a single filament is experimentally observed even though the IR laser pulse peak power (more than 20 GW) is about three times the critical one used in our calculations (see below). Thus, there is no multi-filamentation in the experiment. A single femtosecond filament started in front of the geometrical focus of the lens. The extended plasma channel accompanying the

filament is visualized from the side by means of the CCD matrix (Spiricon SP620). The remarkable increase of the filament length with increasing amplitude of the spherical aberration is observed (**Fig. 4.13**) (geometrical focus is not shown in the figure because the spherical aberration introduction resulted in a small change of the focus distance in the experiment).

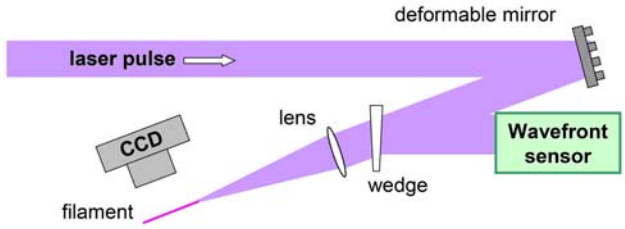

Figure 4.12. Experimental setup for introducing spherical aberrations into the laser beam profile

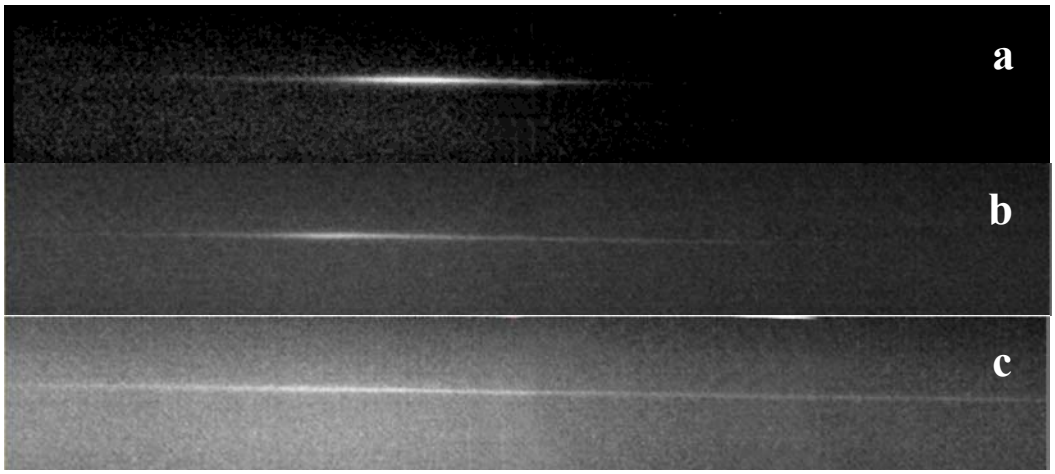

Figure 4.13. Side images of plasma channels for different spherical aberrations of amplitude A_Z introduced by the deformable mirror. **a**– $A_Z = 0$, **b** – $A_Z = 0.1$ μm, **c** – $A_Z = 0.18$ μm. The image longitudinal size is 35 mm. Laser pulse is directed from the right hand side.

4.2.2. Numerical simulation of the pulse propagation in the air has been performed based on the slowly evolving wave approximation. The equation for the slowly varying light field amplitude $E(r, z, \tau)$ in the case of cylindrical symmetry, which we can assume due to the experimental fact of a single filament formation, is given by:

$$2ik_0 \frac{\partial E}{\partial z} = \hat{T}^{-1}\Delta_\perp E - k_0 \sum_{n=2}^{\infty} \frac{k^{(n)}}{(i^n n!)} \frac{\partial^{(n)} E}{\partial \tau^n} + 2k_0^2 \left(\hat{T}\Delta n_k + \hat{T}^{-1}\Delta n_p\right) E - ik_0 \alpha(r,\tau) E \qquad (4.1)$$

where $\tau = t - z/v_g$ is the pulse time, Z is the propagation distance, $\Delta_\perp = r^{-1}\partial/\partial r(r\partial/\partial r)$ is the transversal Laplacian describing diffraction, ω_0 and k_0 are the laser central frequency and the corresponding wavenumber, v_g is the group velocity corresponding to the frequency ω_0. The second term on the right-hand side of the Eq. (4.1) describes material dispersion including the second and the higher orders ($k^{(n)}$ is the dispersion coefficient of the n-th order). The values Δn_k and Δn_n in the third term on the right-hand side of Eq. (4.1) represent Kerr and plasma nonlinearities, respectively. The function $\alpha(r, \tau)$ is responsible for the ionization energy loss in the air. Operator $\hat{T} = 1 + i/\omega_0 \, \partial/\partial\tau$ describes self-steepening.

In the simulations the critical power for self-focusing in the air is taken as $P_{cr} \approx 10$ GW for a 45 fs laser pulse with the wavelength 744 nm propagating in the atmospheric pressure air according to the experiment. Such magnitude of the critical power of self-focusing in air

corresponds to its direct measurement for laser pulse with ~50 fs duration. The experimental results obtained for femtosecond radiation with similar duration and lower quality of spatial mode are in good agreement with [43]. The self-consistent plasma production is taken into account through the contribution to the refractive index, the real part of which is represented by:

$$\Delta n_p(r,z,\tau) = -\frac{2\pi e^2 n_e}{m_e \omega_0^2} \tag{4.2}$$

where m_e and e are electron mass and charge respectively, and n_e is the free electron density, which is calculated according to the rate equations with the ionization probability of nitrogen or oxygen molecules taken from [44].

In the simulations the initial pulse is Gaussian with the wavefront $\varphi(r)$ (Eq. (2.1)) corresponding to the spherical aberration introduced by deformable mirror in the experiment:

$$E(r,z=0,\tau) = E_0 \exp\left(-\frac{r^2}{2a_0^2} - \frac{\tau^2}{2\tau_0^2}\right) \times \exp\left[i\frac{k_0 r^2}{2F} + i\varphi(r)\right] \tag{4.3}$$

The beam radius is a_0 = 1.2 mm, the half-pulse duration is τ_0 = 27fs, the pulse energy is 1.5 mJ. The geometrical focusing distance is F = 226 cm. The beam radius a_0 in the simulations is smaller than in the experiment in order to preserve good spatio-temporal resolution on the 3D plus time grid. In the simulation we used the same ratio $A_z/k_0a_0^2$ of the mirror deformation amplitude A_Z to the diffraction length $k_0 \cdot a_0^2$ as used in the experiment. Therefore, the absolute values of the mirror deformation amplitude $A_{Z\text{sim}}$ will be smaller in the simulations than in the experiment A_{Zexp}. At the same time, the ratio $A_{Zsim} / k_0 a_{0sim}^2 = A_{Z\exp} / k_0 a_{0\exp}^2$ remains unchanged when we simulate the filament with spherical aberrations in the initial wavefront. The simulations show that in the linear regime the spherical aberration leads to the elongation of the focal zone by a factor of 1.5 with the beam wavefront distortion corresponding to A_Z = 0.15μm as compared to the case without distortion. Self-focusing and filamentation enhance the elongation effect. Both experimentally registered and simulated filaments reveal more than twofold plasma channel length increase with the increase in the spherical aberration amplitude A_Z from 0 to 0.15 μm (compare panels (**a**) and (**c**) in **Figs. 4.13** and **4.14**).

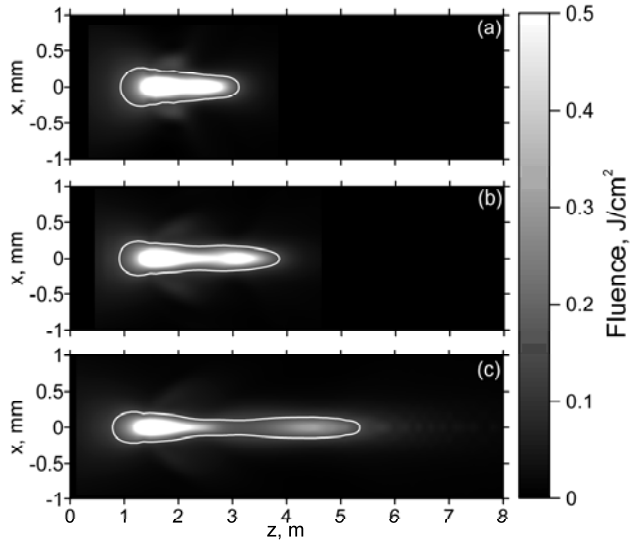

Figure 4.14. Elongation of simulated femtosecond filaments. The amplitude of the wavefront deformations corresponds to **a** - A_Z = 0, **b** - A_Z = 0.1 μm, **c** - A_Z = 0.18 μm

The structure of the simulated channels is in good qualitative agreement with the experiment. Indeed, without spherical aberrations the channel is comparatively bright and short (**Fig. 4.13a** and **Fig. 4.14a**). The arrows (**Fig. 4.13a**) and the white contour line (**Fig. 4.14a**) define the intense fluence region at the level 0.1 of the maximum fluence value. With the increase of the spherical aberration amplitude the length of this selected region is preserved, the overall channel length increases by a factor of 2 at least (**Fig. 4.13b,c** and **Fig. 4.14b,c**). Comparison between the experimentally obtained and calculated channel dynamics shows that numerical simulations reproduce filamentation controlled by the spherical aberrations in an adequate way (**Fig. 4.14**). Loose geometrical focusing chosen in the simulations allows us to further reveal the effect of wavefront deformation on the channel shape which is not straightforward in the experiment. The detailed structure of the channels is shown by the contours of equal fluence in **Figs. 4.15a,b**. Without spherical aberrations the radiation diverges out of the channel at a larger angle than in the case with the spherical aberration (compare **Fig. 4.15a** and **Fig. 4.15b)**. The local minima or the "brim" of the hat-like phase of the spherical aberration (**Fig. 2.5**) keep the radiation within a limited transverse area for a longer distance (**Fig. 4.15b**) than without the aberration (**Fig. 4.15a**).

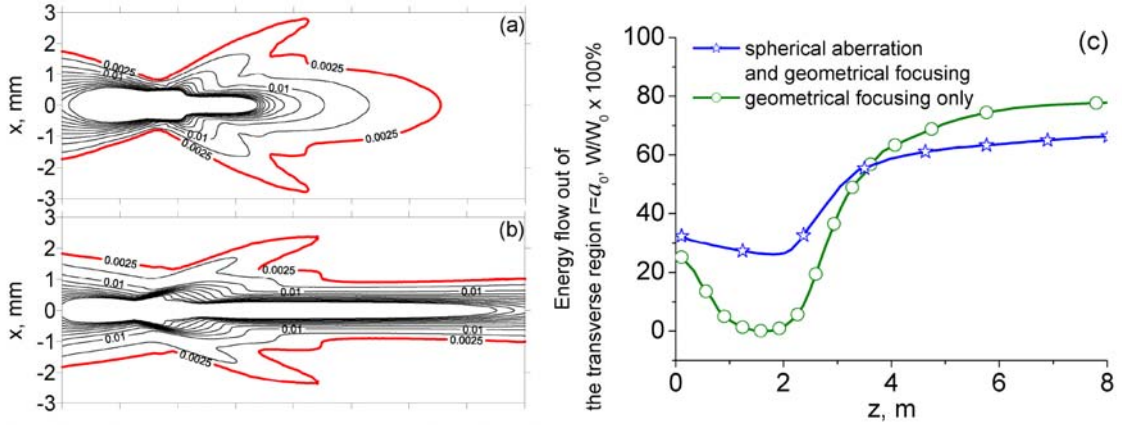

Figure 4.15. (a, b) Contour maps of the simulated filament channels obtained (**a**) without the wavefront distortions and (**b**) with the maximum wavefront distortion, which corresponds to $A_Z = 0.18$ μm. The interval between the lowest and the nearest contours is 0.0025 J/cm^2, all the other contour intervals are 0.005 J/cm^2. (**c)** The energy leaking out from the channel region in the case of the maximum $A_Z = 0.18$ μm wavefront deformation (stars) and without the wavefront deformations (circles).

Quantitatively, the change of the filament channel properties in the presence of spherical aberrations is characterized by the amount of energy outgoing from the channel (**Fig. 4.15c**). The two curves in **Fig. 4.15c** show how much energy is outside of the round-shaped near-axis area with the radius equal to the initial beam radius a_0. If there are no spherical aberrations in the beam phase, than the energy pulsations in the channel are very high, up to 80 % (**Fig. 4.15c**, circles) of the total beam energy. At the beginning of the propagation all the energy flows inside the area with the initial beam radius a_0, then 80% of the beam energy flow outside this area. The critical effect of spherical aberration introduced into the beam is the decrease in both the energy flowing inside the near-axis area and the energy flowing outside (**Fig. 4.15c**, stars). The energy variation in the near–axis area decreases down to 35% of the total beam energy. This energy variation decrease quantitatively demonstrates that the spherical aberration leads to the decrease in the energy outflow from the filament. If the outflow decreases then the filament can be sustained for longer distance. That is why we observe filament elongation in the presence of spherical aberrations in the laser beam profile.

5. Basic mechanisms of air ionization and relaxation under UV nanosecond and femtosecond pulses at 248-nm wavelength

To investigate the basic mechanisms of air ionization by UV laser radiation experiments were carried out with two different laser sources, both being operated at wavelength λ = 248 nm. One laser is electric-discharge pumped KrF laser Lambda Physik EMG TMSC with output energy up to 200 mJ, which is sometimes used as the master oscillator of GARPUN KrF laser facility [14], or in the present hybrid Ti:Sapphire/KrF performance it is commonly used for triggering e-beam pumped preamplifiers [15]. As the original laser pulse FWHM length of τ_p=25 ns is comparable with electron lifetime τ_e, in some experiments laser pulse is shortened down to 4 ns by using electro-optic truncating scheme (**Fig. 5.1)**. A HV pulser has been specially developed for the Pockels cell, which produced a variable drive pulse of 4–10 ns with leading and trailing edges less then nanosecond. The other laser is frequency-tripled 100-fs, 0.5-mJ Ti:Sapphire front-end commonly used as the master oscillator of the hybrid GARPUN-MTW laser system (see Subsection 2.2).

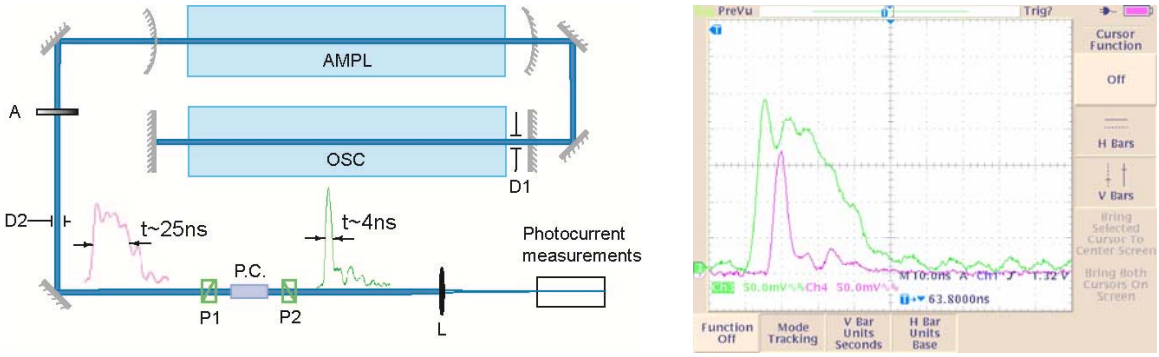

Figure 5.1. Electro-optic truncating scheme for shortening the laser pulse (left); original (green) and truncated (pink) laser pulses (right).

To measure photoionization plasma conductivity and electron density laser radiation with variable pulse energy is focused with various lenses (F = 0.5, 0.7 and 2 m) through ring electrodes (to eliminate a photoemission from electrodes) into inter-electrode gap with the length l that is varied from 0.5 to 12 mm in adjustment with the length of laser beam waist in lens caustic (**Fig. 5.2**). A DC voltage U=0.2÷2.5 kV is applied to the gap with a caution that no spark gas breakdown does occur. A distribution of laser radiation across the laser beam waist near the focus is measured by an OPHIR beam profiler.

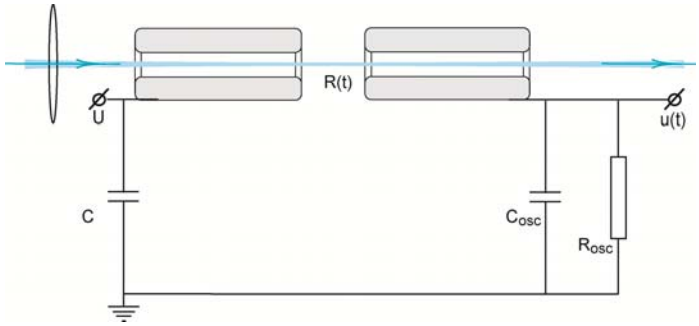

Figure 5.2. Layout of plasma conductivity measurements.

5.1. Electron density measurement in plasma produced by 25-ns UV laser pulse in atmospheric air

For the discharge-pumped KrF laser an average diameter d of the beam in a focal plane (at FWHM of energy fluence distribution) of 2-m focal lens length is ~100 μm (**Fig. 5.3)**. For other lenses, the distribution is similar, the diameter being proportional to a focal length. Laser intensity is varied in the range $I=3\cdot10^6–7\cdot10^{10}$ W/cm^2 by attenuation of laser energy by a stepped diffraction attenuator, by changing the focal length, or by defocusing laser beam (by moving the focus off the inter-electrode gap). The maximum laser intensity is just below avalanche air breakdown. For nanosecond UV pulses it is determined to be $I_{th}=(2–3)\cdot10^{11}$ W/cm^2.

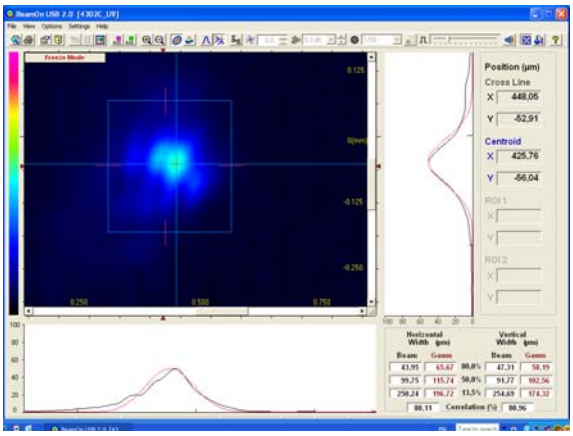

Figure 5.3. Distribution of laser radiation in the focal plane of F=2 m lens. Beam diameter at FWHM is d~100 μm.

To measure plasma photoconductivity in different gases and at reduced gas pressures, the measurement facility is placed inside a chamber which is equipped with a vacuum pump and gas-filling system (**Fig. 5.4**).

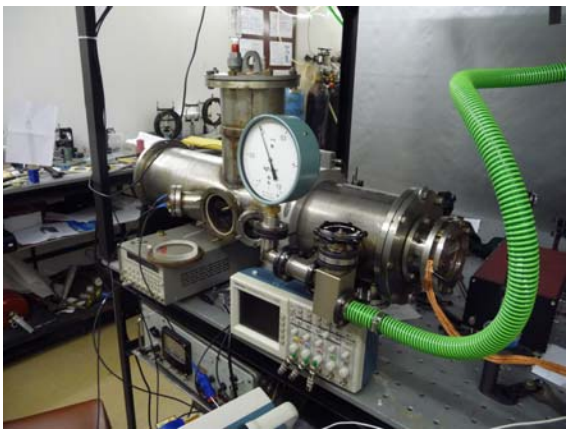

Figure 5.4. The chamber for conductivity measurements in various gases.

Specific conductivity of the plasma channel $\sigma(t)$ and oscilloscope signal $u(t)$ are related by following formula:

$$\frac{du(t)}{dt}C_{osc}+u(t)\frac{1}{R_{osc}}=\frac{US}{l}\sigma(t), \tag{5.1}$$

where C_{osc} =150 pF includes both oscilloscope input and cable capacitances; $S=\pi d^2/4$ is a cross-section area of the plasma channel along inter-electrode gap l. For a low-impedance matched oscilloscope with the input resistance R_{osc} = 50 Ω plasma conductivity is proportional to the oscilloscope signal $\sigma(t)=\frac{l}{USR_{osc}}u(t)$ with a response time ~1 ns. For high-impedance input R_{osc}= 1 MΩ the signal is integrated over time $R_{osc}C_{osc}$~150 μs, and $u(t)=\frac{US}{lC_{osc}}\int_0^t\sigma(t')dt'$.

Laser pulses and different waveforms of voltage signals $u(t)$ produced by photoionization current for different oscilloscope inputs are measured on different time scales. For atmospheric air, they are shown in **Figs. 5.5*a*–5.5*d***.

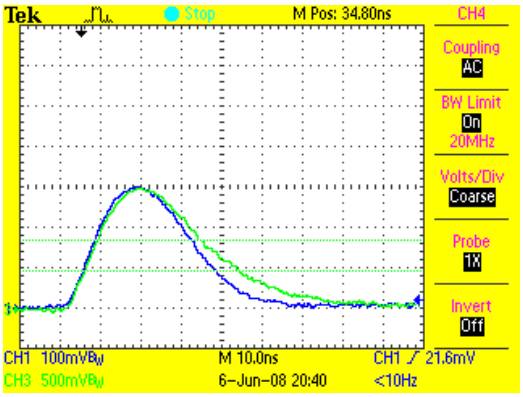

(*a*) R_{osc} =50 Ω, 10 ns/div

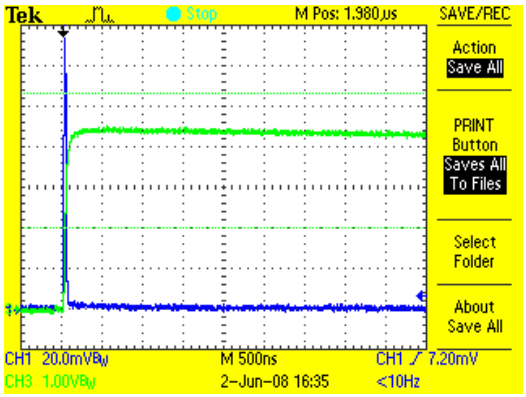

(*b*) R_{osc} =1 MΩ, 0.5 μs/div

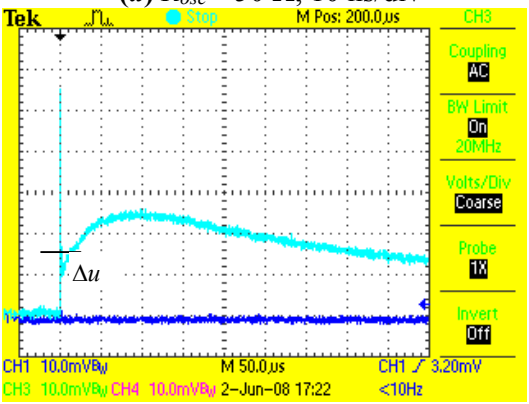

(*c*) R_{osc} =1 MΩ, 50 μs/div

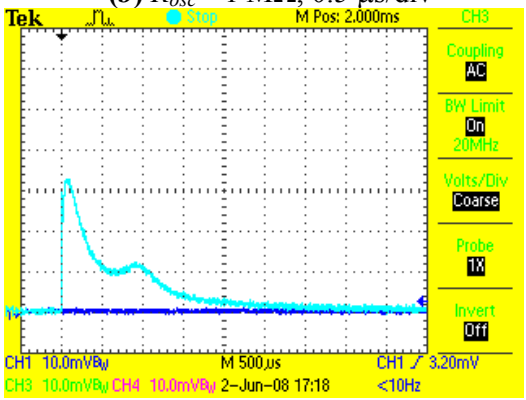

(*d*) R_{osc} =1 MΩ, 500 μs/div

Figure 5.5. Oscilloscope traces of laser pulse (dark blue) and signals produced by photoionization current for various oscilloscope inputs and on different time scales (other colors).

By analyzing the signals in **Fig. 5.5** one can see that there are three photocurrent regions with different current carrier mobility in a steady electric field $E=U/l$ and with different relaxation time: (i) the fast current component is synchronous with laser pulse and lasts slightly longer (a) – it is attributed to electrons; (ii) the slower current component attains the maximum value by

~100 μs – it is attributed to positive or negative ions O_2^+, N_2^+, O_4^+, O_2^-, and so on, being formed from the main air species such as oxygen and nitrogen in ionization and electron attachment processes and going down due to ion-ion relaxation; (iii) long-lived ion current lasting for a few ms – it might be caused by non-compensated ions in the presence of microscopic charged aerosol particles (or very large cluster ions) formed in the photoemission process. The latter is blown off if airflow is organized perpendicular to the discharge gap. As electrons have at least 3 orders of magnitude higher mobility than the ions one, we easily select their contribution into plasma conductivity σ_e. In the case of high-impedance oscilloscope input photoelectron current integrated over electrons lifetime τ_e produced the initial steep jump Δu, while the following gradual signal growth and decline corresponded to time-resolved ion current.

As the distribution of laser radiation contains broad wings (they are not distinctly visible with the beam profiler because of its limited dynamic range), special attention is paid to prevent photoelectron emission from ring electrodes. A fulfillment of Ohm's law is checked firstly for Δu versus applied voltage U (for a fixed drift gap l) and Δu versus l (for a fixed voltage U) dependences. Being shown in **Fig. 5.6** they evidence that (i) there is no contribution of photoelectron emission from the electrodes (dependence $\Delta u \sim 1/l$), and (ii) there is no noticeable variation of electrons lifetime with electric field strength in the gap (dependence $\Delta u \sim U$). It means that electron attachment to oxygen (the main relaxation process for moderate electron densities) is suppressed by an inverse photodetachment process, which takes place for long enough 25-ns laser pulse. The electron density is then calculated as $n_e = \dfrac{\sigma_e}{e\mu_e}$ with assumed electron mobility value $\mu_e \approx 600$ cm^2 atm·(V·s)$^{-1}$ in accordance with [45, 46].

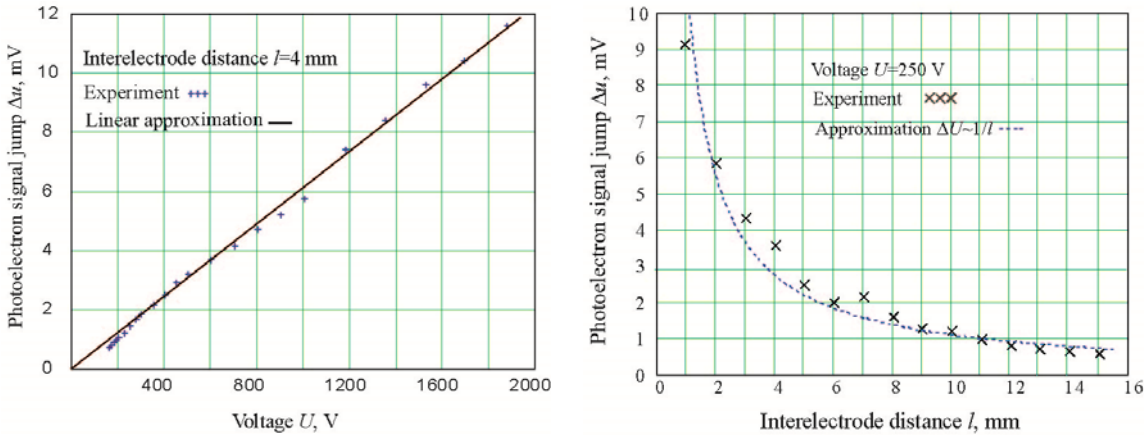

Figure 5.6. Photoelectron signal jump Δu vs. applied DC voltage U for a fixed drift length l=4 mm (left) and vs. l for a fixed U=250 V (right).

The dependence of the electron density n_e on laser intensity I derived from the conductivity measurements is shown in **Fig. 5.7**. In the intensity range $I = 3\cdot10^8$–$7\cdot10^{10}$ W/cm^2 experimental dots are well approximated by a power law $n_e \propto I^2$. Similar dependences are observed in experiments [47, 48] for short UV laser pulses τ_p=35 ps with I=10^{10}–10^{11} W/cm^2 and in [49] for even shorter pulses τ_p=400 fs and I~10^{11} W/cm^2. Such dependence manifests the REMPI proceeding through an excitation of high-energy Rydberg intermediate molecular levels which is followed by one-photon ionization. The REMPI processes can lead to significant enhancement of the ionization yield compared with direct Multi-Photon Ionization (MPI) of air molecules from the ground state. A reach vibration spectrum of the key air components,

molecular nitrogen and oxygen, opens a number of REMPI channels, the most probable of which are those which includes a two-photon excitation of metastable states. The (2 + 1) and (3 + 1) REMPI in N_2 with ionization potential I_i=15.6 eV through the $^1\Sigma_g^+$ molecular state is observed in the field of ArF ($h\nu$=6.3 eV) [50, 51] and KrF laser radiation ($h\nu$=5.0 eV) [51]. MPI of molecular oxygen via two-photon resonant $ns\sigma_g$, $nd\sigma_g$, and $nd\pi_g$ Rydberg levels by KrF laser radiation is studied in [52].

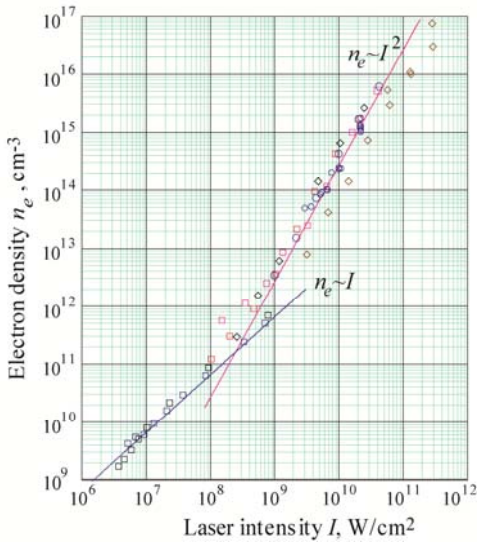

Figure 5.7. Electron density n_e vs. laser intensity I. Different symbols correspond to various focusing conditions.

For higher laser intensities $I \geq 5\cdot10^9$–$2\cdot10^{10}$ W/cm^2 and correspondingly higher electron density (**Fig. 5.7**) the dependence n_e (I) goes softly. This manifests that electron attachment to oxygen changes to electron recombination with positive ions. As a result, a photocurrent signal in **Fig. 5.5*a*** follows a laser pulse-form, being slightly delayed during its falling edge. At lower laser intensity $I = 3\cdot10^6$–$3\cdot10^8$ W/cm^2 a linear dependence $n_e \propto I$ is observed which could be explained by a (1 + 1) REMPI of impurity molecules with low ionization potential $I_i \leq 10$ eV or by photoemission from aerosol microscopic particles [53]. An influence of impurities on the conductivity is observed in experiments – additives of some organic hydrocarbon vapors, e.g. kerosene to laboratory air increased photoionization signal by 2–3 orders of magnitude and it is linear within the whole intensity range $3\cdot10^6$–$7\cdot10^{10}$ W/cm^2. Similar effect is also observed in the tobacco-smoke atmosphere.

5.2. Electron density measurement in plasma produced by 25-ns UV laser pulse in nitrogen

Comparison of photoionization signals in air (***a***, ***c***) and pure nitrogen (***b***, ***d***) measured for the same laser intensity and inter-electrode voltage is demonstrated in **Fig. 5.8.** Nitrogen before filling the chamber is passed through a cryogenic filter. The main difference of photoelectron current in nitrogen is a long tail of few μs duration after termination of the laser pulse**,** which evidences that either attachment of electrons to N_2 molecules or electro-ion recombination has less impact on electron lifetime. This results in accumulation of electrons during the laser pulse. However, the amplitude of electron current in nitrogen being measured on the matched oscilloscope input is 10 times less than in air. No long-lived ms-scale ion currents as those in atmospheric air (see **Figs. 5.5*c*, 5.5*d***) were observed in nitrogen. The dependence of σ_e on laser

intensity in nitrogen is plotted in **Fig. 5.9**. For higher intensities $I = 5 \cdot 10^9 – 7 \cdot 10^{10}$ W/cm^2 experimental dots are well approximated by a power law $n_e \propto I^3$ typical for a two-step cascade ionization of N_2 molecules through a resonance 3-photon excitation of intermediate highly-excited Rydberg levels with successive fast 1-photon ionization (3 + 1). In general, electron densities n_e in nitrogen including a linear region at low laser intensities are less than in air. Thus, it is confirmed in present experiments that oxygen plays the main role in generation of photoelectrons in air.

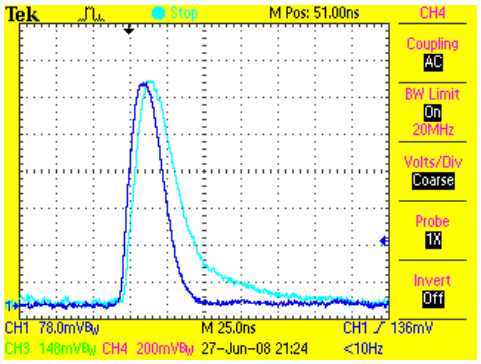

(*a*) Air; R_{osc}=50 Ω, 25 ns/div

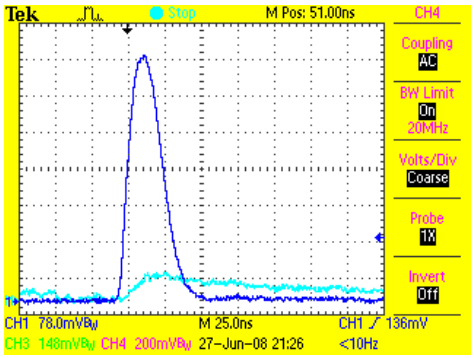

(*b*) Nitrogen; R_{osc}=50 Ω, 25 ns/div

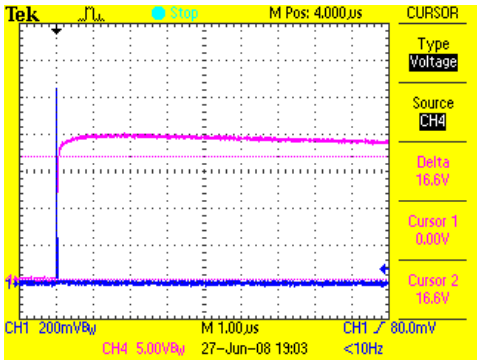

(*c*) Air; R_{osc}=1 MΩ, 1 µs/div

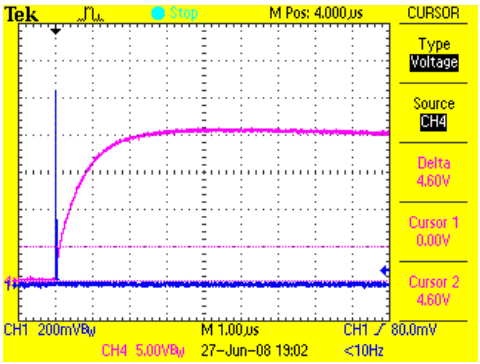

(*d*) Nitrogen; R_{osc}=1 MΩ, 1 µs/div

Figure 5.8. Oscilloscope traces of laser pulse (dark blue) and signals produced by photoionization current on various oscilloscope inputs and in different time scales (other colors) in air and nitrogen.

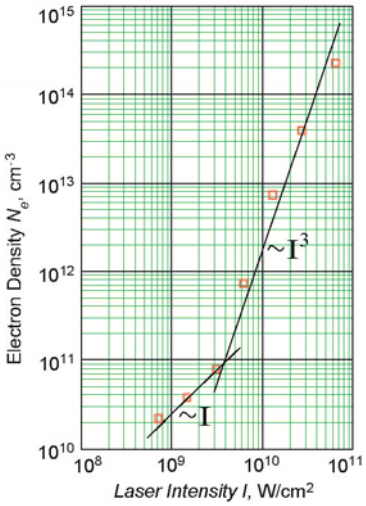

Figure 5.9. Electron density vs. laser intensity in nitrogen.

5.3. Electron density measurement in plasma produced by 4-ns UV laser pulse in reduced pressure air

Shortened pulse duration τ_p = 5 ns is less than electron relaxation time τ_e. In the range of linear dependence of photoelectron concentration on laser intensity ($I \le 3 \cdot 10^8$ W/cm^2) one can express the experimental values of photoelectron signal jump Δu through total laser pulse energy integrated over laser spot distribution $Q = \tau_p \int_S Ids$.

$$\Delta u = \frac{e\mu_e E Q k_{ph}^{(1)} p \tau_e}{C_{osc}} \left[1 - \frac{\tau_e}{\tau_p} \left(1 - exp\left(-\tau_p / \tau_e \right) \right)^2 \right], \qquad (5.2)$$

where e is elementary charge; μ_e is electron mobility; $k_{ph}^{(1)}$ is a coupling coefficient between the rate of electrons production $\frac{dn_e}{dt}$ and laser intensity I in air at atmospheric pressure p = 1 atm.

Experimental dependences $\Delta u(Q)$ measured for different air pressures (**Fig. 5.10**) are linear, Δu rapidly falls down with the pressure (**Fig. 5.11**).

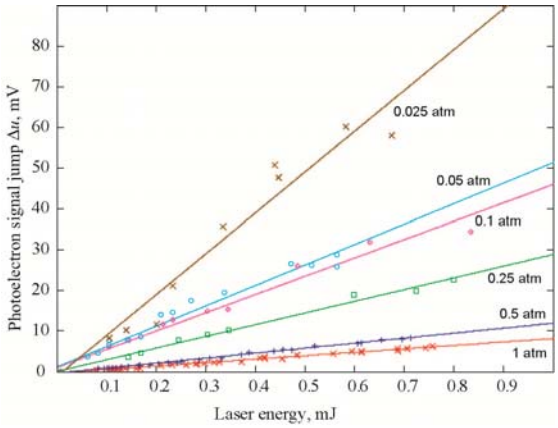

Figure 5.10. Photoelectron signal jump Δu vs. laser energy Q for different air pressures p. U=2 kV, l=4 mm.

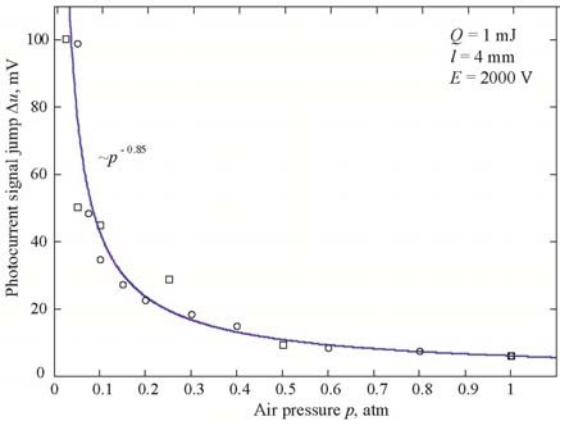

Figure 5.11. Photoelectron signal jump Δu vs. air pressure p. Q=1 mJ, U=2 kV, l=4 mm.

The coupling coefficient $k_{ph}^{(1)}$ = 5.3·10^{10} (cm·s·W·atm)$^{-1}$ is determined using formula (5.2) from the slope of $\Delta u(Q)$ dependence for the atmospheric pressure air. The electron mobility is assumed $\mu_e \approx 600$ cm^2·atm·(V·s)$^{-1}$, electric field E = 5 kV/cm, laser pulse duration τ_p = 4 ns. The lifetime of electrons τ_e = 50 ns at p=1 atm is measured in independent experiments described below (Subsection 5.7.1).

As electron mobility is inversely proportional to gas pressure $\mu_e \sim 1/p$, dependence $\Delta u(p)$ in formula (5.2) is determined only by pressure dependence of electron lifetime τ_e (p). It is calculated from the experimental data and is shown in **Fig. 5.12.** The observed behavior reflects that with a reduced pressure a three-body electron attachment with a rate $\infty k_{3at} \cdot p^2$ is gradually changed by a two-body dissociative process with a rate $\infty k_{dat}\, p$ (see Subsection 5.5). Note that for a fixed drift field E =5 kV/cm the ratio E/N increases with pressure decrease, which should lead to the electron temperature rise [8, 9, 46]. In addition, at higher E/N

avalanche gas ionization might affect the electron density, so that the measured τ_e at low pressures should be considered like "an effective lifetime".

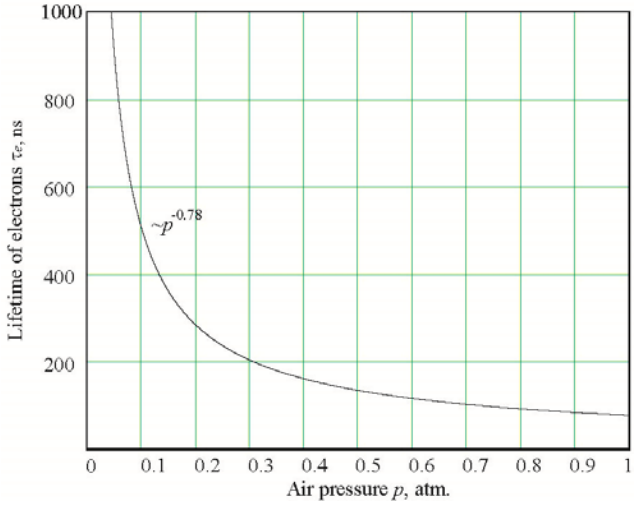

Figure 5.12. Lifetime of electrons τ_e vs. air pressure p. Q=1 mJ, U=2 kV, l=4 mm.

5.4. Electron density measurement in plasma produced by double 100-fs IR and UV filamented laser pulses

In this section parameters of plasma channels formed by double laser pulse consisting of two sequential USPs with a variable nanosecond time delay at wavelengths of both λ=248 nm and 740 nm are experimentally studied using a Ti-sapphire femtosecond laser system. The USPs of 100 fs pulse duration (FWHM) followed with 10-Hz repetition rate and have laser beam radius of 4 mm (at e^{-1} level). The USP peak power is as high as a few self-focusing critical power (P_{cr} ~ 3-5 GW for λ = 744 nm, P_{cr} ~ 100 MW for λ = 248 nm), which guaranteed just a single filament formation. The USP energy is 1 mJ for IR radiation and 35 μJ for the UV one. The laser beam is directed to a semitransparent mirror which splits it into two beams in different directions and again being superposed on the next semitransparent mirror to propagate along the common optical axis. The time delay between the two USPs is varied from 1.5 to 15 ns by changing optical paths of the USPs. The double pulse is focused by a concave mirror with 1 m focal length. The match of the optical axes for the two USPs is controlled by a CCD-camera in the far-field region.

Electron density distribution of the plasma channels along the filaments formed by the double pulse is measured by a photocurrent produced in a gap between two spherical electrodes. When a laser pulse goes through the electrode gap, capacity formed by the electrodes is changed due to arising plasma, and the capacitor recharge current and corresponding voltage are recorded by an oscilloscope with time resolution ~1 ns. Since the change of the capacity depends on the electron density, length and width of the plasma channel being formed between the electrodes, the measured current and corresponding voltage are proportional to the linear density of the plasma channel (the integral of the plasma density over the cross section of the channel). The electrodes are moved along the plasma channel giving an opportunity to measure the linear plasma distribution over the plasma channel length. First, the peak voltage corresponding to the first and second USPs is measured. Then the second USP is blocked, and the signal amplitude is measured at a time corresponding to the second USP time delay. The electron plasma density formed by the second USP is determined through measuring the difference of signal amplitudes. It should be noted that the voltage between the electrodes (2.5 kV) is chosen in such a way that the time of electron attachment to oxygen depending on applied voltage exceeds 15 ns [30]. Thus, the second pulse is propagated in electron-ion plasma.

Figure 5.13 shows the linear density (arb. units) of the plasma channels formed under filamentation of two consequent UV USPs versus the distance $\Delta Z = F - Z$ (Z-coordinate of the plasma channel counted off from the focusing mirror along the optical axis, F - focal length) for the first and second pulses at various time delays. Propagation and focusing of the first USP takes place in the neutral air, and density distribution in the plasma channel formed by the first USP is the same in all measurements. At time delays longer than 5 ns, distribution in the plasma channel formed by the second USP is close to that created by the first one. Probably due to refraction of the second USP in a long plasma channel formed by the first one, a slight decrease of plasma density is observed near the end of the channel (in front and behind the focal plane). Nevertheless, the end of the plasma channel is unchanged for different time delays. Reducing the time delay results in significant decrease of plasma density in the channel formed by the second USP. Firstly, this decrease is assumed to be probably caused by refraction of the second USP on the electron-ion plasma formed by the first one, which concentration drops down with time following hyperbolic law because of electron-ion recombination within the time domain under consideration. It seemed this refraction effect must have been far stronger for the IR pulses with higher energy and longer wavelength, creating much higher plasma concentration. It should be noted that plasma density created by USPs for experimental conditions and in nanosecond time domain (about 10^{15}-10^{16} cm^{-3}) is far smaller than critical plasma density for UV and IR radiation (~ 10^{22} and ~ 10^{21} cm^{-3}, respectively). Therefore, plasma channel formed by the first USP has to be transparent for the second one).

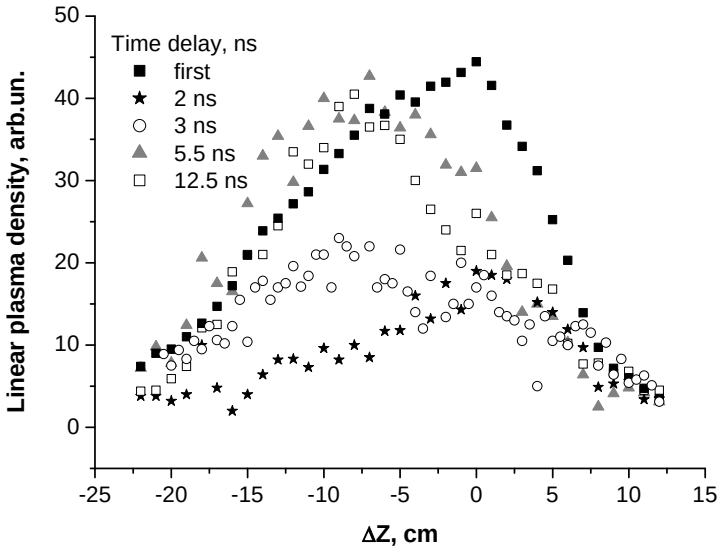

Figure 5.13. Linear plasma density vs. distance $\Delta Z = F - Z$ (Z-coordinate of the plasma channel along the optical axis, F - focal length) for the first UV USP and the second one for various time delays between them. Laser radiation goes from the left side.

That is why the similar experiment (under the same experimental conditions, the optical system, and the same measurement procedure) is carried out with double pulses in the near IR range (wavelength $\lambda = 740$ nm), experimental results being shown in **Fig. 5.14**. It should be noted that at the beginning of the plasma channel the linear plasma density formed by the second USP is slightly higher as compared to the first one. At various time delays the maximal value of linear plasma density formed by the second USP (in the vicinity of linear focus) is approximately two times lower than plasma density formed by the first pulse. Indeed, the process of focusing and self-focusing of the second IR USP seems to be limited by refraction on plasma created by the first pulse. However, in contrast to the UV USPs, there are no significant differences in plasma channels formed by the second IR pulse for the delay times changing from 1.6 ns to 15 ns.

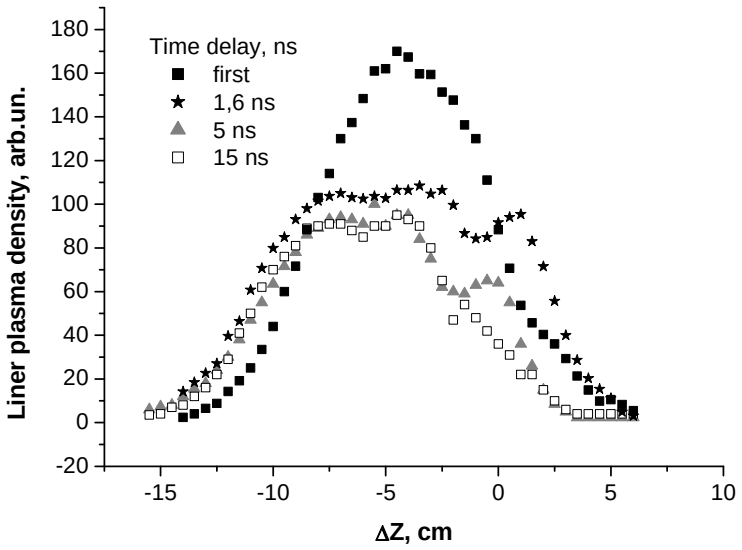

Figure 5.14. Linear plasma density vs. distance $\Delta Z = F - Z$ (Z-coordinate of the plasma channel along the optical axis, F - focal length) for the first IR laser pulse and the second one for various time delays between them. Laser radiation goes from the left.

To determine the nature of such a difference in the experimental results for UV and IR double pulses, the energy ratio of the first and second USPs in front and behind the filamentation area is measured by a wide-aperture detector. In front of the filamentation area for various time delays, the energy ratio of the first and second USPs for both UV and IR double pulses is equal one. In experiments at the wavelength of 740 nm there is no absorption at all of the second USP for all time delays (from 1.5 ns to 15 ns). At 248-nm wavelength absorption of the second USP in the plasma channel formed by previous USP is (15 ± 3)% for the time delay of 1.5 ns. An increase of time delay resulted in a decrease of absorption: (11 ± 3) % at 2.5 ns and (8 ± 3)% at 3.5 ns. For the time delay of 5.5 ns there is no absorption within the experimental error ranged from 0 to 3%. Any appreciable scattering of the second USP in the plasma created by the first USP is not observed. Thus, in the plasma induced by UV femtosecond USP some absorption at the wavelength of 248 nm with a characteristic relaxation time of a few nanoseconds is observed, which can result in change of optical properties of the medium.

The results on UV double pulse (absorption and lower plasma density at short time delay) allow one to suggest the existence of some resonance effects with a decay time of a few nanoseconds. For example, oxygen ions O_2^+ formed by the first USP can be excited by 5-eV energy quantum (λ = 248 nm) resonantly from $X^2\Pi_g$ to $a^4\Pi_u$ levels. It should be noted that probability of 3-quanta process of oxygen ionization is higher than 4-quanta that of nitrogen, i.e. concentration of oxygen ions is higher than nitrogen ones. The resonant absorption at the wavelength of 248 nm can lead to significant changes in the USP propagation. Within a few nanoseconds due to electron-ion recombination oxygen ion concentration is reduced significantly. Properties of the medium turn to initial ones, and, as it is observed at 5.5 ns time delay, the influence of plasma created by the first USP on the second USP propagation becomes negligible. It should be noted that for wavelengths near 740 nm the similar transitions in oxygen ion are absent, i.e. at this wavelength such processes can not be observed, which is confirmed by experiments on the absence of absorption of the second laser pulse at time delays from 1.5 ns to 15 ns.

Therefore, in the conditions of a single filament and a single plasma channel (low power excess over the critical self-focusing one) the use of a train of UV USPs with a period less than 5 ns does not look practical for sustaining plasma in the channel. It should be noted that in case of multifilament mode (laser peak power is much higher than self-focusing one) short time delays

can cause an opposite effect: for the second USP filaments and corresponding plasma channels can appear outside the filamentation zone of the previous USP, which can lead to more uniform filling of the "thick" plasma channel.

5.5. Simple analysis of electron component dynamics in the air plasma

Although a comprehensive description of the air plasma evolution under action of ionizing radiation include a huge amount of secondary reactions and ions (see e.g. [54]) we will follow a bulk of works (see e.g. [46]) in our simple analysis of the main processes

$$\begin{aligned}\frac{dn_e}{dt} &= S_e - n_e\left(k_1 N_{O_2}^2 + k_2 N_{O_2} N_{H_2O} + k_3 N_{O_2}\right) - k_4 n_e^2 - \frac{D_a}{\Lambda^2} n_e + \frac{I}{h\nu} N_{O_2^-}\sigma_{ph} \\ \frac{dN_{O_2^-}}{dt} &= n_e\left(k_1 N_{O_2}^2 + k_2 N_{O_2} N_{H_2O}\right) - \frac{I}{h\nu} N_{O_2^-}\sigma_{ph}\end{aligned} \tag{5.3}$$

Here $S_e = N_0 \sum_j \alpha_j \sigma_j^{(K)} I^K$ is a rate of electrons production in different MPI processes; N_0 is total molecules concentration in air; α_j concentration fractions of various species; $\sigma_j^{(K)}$ are corresponding MPI cross sections; K_j is the MPI degree (i.e., the number of photons needed to ionize the specific air molecule). For KrF laser a direct 3-photon MPI of O_2 molecules (with ionization potential I_i=12.06 eV) is usually suggested as a primary ionization process, while direct 4-photon ionization of N_2 molecule (I_i=15.6 eV) is assumed significantly less probable (see e.g. [55, 56]). However, our experiments and [47–49] evidence that (2 + 1) REMPI dominates for KrF laser pulses of subpicosecond to nanosecond length at least in the intensity range below 10^{11} W/cm^2.

Electron relaxation in the air plasma of medium density is caused mostly by a three-body electron attachment to O_2 molecule

$$O_2 + e + O_2\left(H_2O\right) \xrightarrow{k_1(k_2)} O_2^- + O_2\left(H_2O\right) \tag{5.4}$$

In atmospheric pressure air, the characteristic time for this relaxation $\tau_e = \left(k_1 N_{O_2}^2 + k_2 N_{O_2} N_{H_2O}\right)^{-1}$ varies in literature from few nanoseconds to several hundred nanoseconds. Alternative process of the electron losses, dissociative attachment,

$$O_2 + e \xrightarrow{k_3} O^- + O \tag{5.5}$$

is less effective and gives under our experimental conditions for a ratio of drift electric field E to gas particle density E/N_0 = 20 Td (E=5 kV/cm; N_0=2.7*10^{19} cm^{-3}) the characteristic relaxation time of a few milliseconds estimated on the base of [8]. Both a three-body and two-body relaxation processes are dependent on electric field and air density. For higher E/N_0 and correspondingly for increased electron energy a two-body process begins to dominate over a three-body one [8, 46].

As the binding energies of electron in negative molecular ions O_2^- ε_b~0.5 eV and in atomic ions O^- ε_b~1.4 eV are significantly less than energy quantum of KrF laser radiation $h\nu$ = 5 eV, a reverse process of electrons photodetachment takes place [57]

$$O_2^- + h\nu \rightarrow O_2 + e \tag{5.6}$$

Actually, it is accompanied by photodissociation of O_2^- in the process [58]

$$O_2^- + h\nu \rightarrow O + O^- \tag{5.7}$$

where atomic ions O^- in absorption of photons give again free electrons

$$O^- + h\nu \rightarrow O + e \tag{5.8}$$

Cross sections for the processes (5.6), (5.7) and (5.8) depend on the laser wavelength. For KrF laser (λ =248 nm) they are measured to be enormously high $\sigma_{O_2^-}^{ph}$=9.5*10^{-18} and $\sigma_{O^-}^{ph}$=11.3*10^{18} cm^2 [59, 60]. The photodetchment mitigates or fully vanishes loss of electrons during the laser pulse if its intensity $I >> \frac{h\upsilon}{\tau_e \sigma^{ph}}$ ≈ 8·10^6 W/cm^2, where electron attachment time τ_e ~ 10 ns (without external electric field) is assumed on the base of direct measurements (Subsection 5.7.1). Besides, photodetachment by a consequent laser pulse enables one to revive electrons captured by O_2 molecules up to then [7, 40, 61]. This effect might be very useful to keep the electron density in a plasma channel for a long time using a train of pulses with a relatively low intensity.

An ambipolar electron-ion diffusion is taken into account in Eq. (5.3) for plasma cylindrical geometry with an appropriate diffusion coefficient D_a~ 200 cm^{2}s^{-1} [46] where $\Lambda = R_{pl}/2.4$, R_{pl} is plasma radius equal to laser beam radius. Although diffusion leads to electrons escape from the initial plasma channel of radii R_{pl}≤50 μm, the photocurrent signal in the drift gap being integrated over the plasma cross section is not sensitive to the diffusion.

Dissociative recombination of electrons with positive molecular oxygen ions O_2^+ (their concentration is assumed to be $N_{O_2^+} \approx n_e$) [46],

$$O_2^+ + e \xrightarrow{k_4} O + O^* \tag{5.9}$$

is the only relaxation process where electrons are irretrievably lost and the laser energy spent until then for ionization of O_2 molecules is redistributed between oxygen atoms in the ground and excited states. The rate constant for this process is in the range 1.3·10^{-8}–3.1·10^{-7} cm^3·s^{-1} in dependence on electron temperature. Dissociative recombination prevails at higher electron density $n_e \geq n_e^* = \frac{\left(k_1 N_{O_2}^2 + k_2 N_{O_2} N_{H_2O}\right)}{k_4}$ = 10^{14}-10^{15} cm^{-3}, which corresponds in our case to laser intensities I≥5·10^9–2·10^{10} W/cm^2 (**Fig. 5.7**). Such regime becomes apparent in **Fig. 5.5*a*** with a photocurrent signal following a laser pulse except for its trailing edge.

5.6. Photodetachment of electrons from O_2^- ions

To demonstrate the revival effect and storage of electrons via the processes (5.6) – (5.8) we used a tandem (or another word a double) pulse scheme (**Fig. 5.15)**. Laser radiation is split into two beams, one of them passes an optical delay line and is superimposed with a non-delayed beam. The combined beam is focused by F=70 cm lens in the drift gap to measure a photocurrent response. Overlapping of both beams in the focal plane is controlled by the beam profiler. Because of slight astigmatism of the focal spots and parasitic vibration of optical mirrors of the delay line overlapping of the beams is measured to be ζ=0.8 on the average.

Typical oscilloscope signals of the tandem laser pulse and photoelectron current on matched oscilloscope input are presented in **Fig. 5.16** for a time delay between two pulses τ_d =80 ns. The intensity of the first pulse is set I_1=3.3·10^9 W/cm^2 (averaged value over a full focal spot distribution of 250-μm diameter) so that the condition $n_e \le n_e^*$ is satisfied and a three-body attachment (5.4) prevailed over dissociative recombination (5.9). It is seen that photocurrent attains the maximum to the end of the laser pulse and lasts for about 100 ns. This manifests slowdown of electrons attachment to O_2 molecule under the action of laser radiation. By the arrival of the second delayed pulse, the most of electrons produced by the first pulse are already attached. Amplitude of the second photocurrent pulse appears to be bigger than of the first one in contrast to the ratio of amplitudes of laser pulses. This definitely indicates that the second laser pulse not only produces photoelectrons in the primary REMPI process but, additively, photo-detaches them from negative molecular ions O_2^-, formed in the relaxation after the first laser pulse. This effect of the second pulse is observed also for a 40-ns time delay between laser pulses.

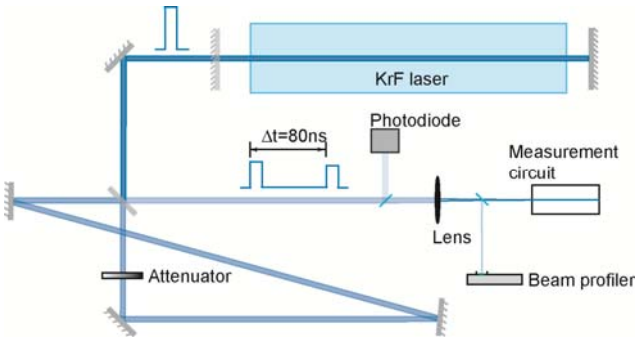

Figure 5.15. Layout of the tandem pulse experiments.

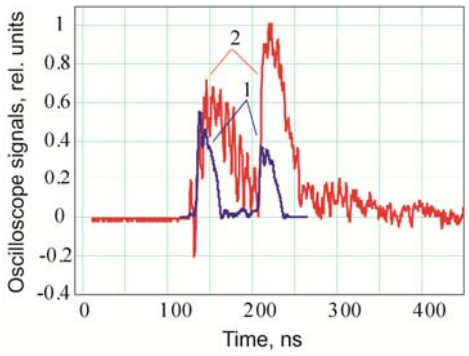

Figure 5.16. Oscilloscope traces of the tandem laser pulse (1) and photoelectron current on matched oscilloscope input (2).

To characterize how much electrons are revived by the second laser pulse the electron revival photodetachment ratio R_e is introduced which is

$$R_e = \frac{\Delta u_{1+2} - (\Delta u_1 + \Delta u_2)}{\Delta u_1 \zeta \left[1 - exp\left(-\frac{\tau_d - \tau_p}{\tau_e}\right)\right]} \qquad (5.10)$$

Here Δu_{1+2} is photoelectron signal jump produced by the tandem laser pulse, Δu_1 and Δu_2 are photoelectron signals produced in turn by two single pulses (with blocked second pulse) with the same amplitudes like in the tandem pulse, all being measured independently on a high-impedance oscilloscope input; ζ =0.8 is a spatial overlapping in the tandem laser beams. A numerator in expression (5.10) is proportional to the total amount of revived electrons flowed through a drift gap. A denominator is proportional to amount of ions O_2^- formed after termination of the first laser pulse in electron attachment till the beginning of the second pulse. It is assumed that under the action of laser radiation attachment is fully balanced by a photodetachment process. The value τ_e in Eq. (5.2) can be considered as fitting parameter to attain independence of parameter R_e on τ_d varying in the range up to at least a few hundreds of microseconds (that is the characteristic time of ion-ion recombination). For our two experimental marks of τ_d = 40 and 80 ns, the best fit for τ_e is 50 ns (see **Fig. 5.17**).

Figure 5.17 represents the photodetachment ratio R_e for the fixed intensity of the first pulse I_1=3.3*10^9 W/cm^2 as a function of average intensity of the second pulse which is varied by a stepped diffraction attenuator in the range I_2 = 2·10^7–2·10^9 W/cm^2. It is seen that for the assumed value of electron lifetime τ_e =50 ns for both time delays τ_d of 40 and 80 ns the ratio R_e is the same and it depends only on the intensity of the second pulse. For average intensity in the laser spot higher then ~10^9 W/cm^2 R_e tends to unity that is almost all attached electrons are revived.

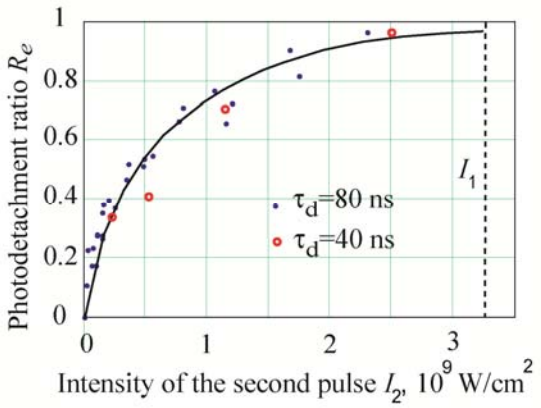

Figure 5.17. Electron photodetachment ratio R_e vs. averaged intensity of the second laser pulse I_2. Intensity of the first pulse I_1 = 3.3·10^9 W/cm^2 and τ_e = 50 ns.

5.7. Decay of air plasma produced by pulsed UV laser. Electron attachment in DC electric field

Electron density time behavior in air obeys Eq. (5.3). Dissociative recombination of electrons with positive ions at $n_e \geq n_e^*$ (see Subsection 5.5) is the only process where electrons are

irretrievably lost and the laser energy spent for ionization of O_2 molecules is redistributed between atoms and molecules in the ground and excited states.

$$\begin{aligned} &O_2^+ + e \xrightarrow{\beta_1} O + O^* \\ &O_4^+ + e \xrightarrow{\beta_2} O_2 + O_2^* \\ &N_2^+ + e \xrightarrow{\beta_3} N + N^* \\ &N_4^+ + e \xrightarrow{\beta_4} N_2 + N_2^* \end{aligned}, \qquad (5.11)$$

Positive ions are formed in the primary air photo-ionization or via conversion processes

$$\begin{aligned} &O_2^+ + 2O_2 \rightarrow O_4^+ + O_2 \\ &N_2^+ + 2N_2 \rightarrow N_4^+ + N_2 \end{aligned} \qquad (5.12)$$

The rate constants $\beta_1 \ldots \beta_4$ in the reactions (5.11) depend on the effective electron temperature T_e (in Kelvin) [54, 62]

$$\begin{aligned} &\beta_1 = 2 \cdot 10^{-7} \left(\frac{300}{T_e} \right) \ \mathrm{cm^3 \cdot s^{-1}} \\ &\beta_2 = 1.4 \cdot 10^{-6} \left(\frac{300}{T_e} \right)^{0.5} \ \mathrm{cm^3 \cdot s^{-1}} \\ &\beta_3 = 4.8 \cdot 10^{-7} \left(\frac{300}{T_e} \right)^{0.5} \ \mathrm{cm^3 \cdot s^{-1}} \\ &\beta_4 = 2 \cdot 10^{-6} \left(\frac{300}{T_e} \right)^{0.5} \ \mathrm{cm^3 \cdot s^{-1}} \end{aligned}, \qquad (5.13)$$

which is established in the relaxation of initial spectrum of photoelectrons. Although the rate constant for the first reaction of (5.11) is the lowest, it plays the main role among the others because it is O_2^+ ions that are predominantly formed due to mutiphoton air ionization.

When it becomes that $n_e \leq n_e^*$, electrons in the air plasma disappear mostly via three-body electron attachment to O_2 molecule (see Subsection 5.5). The process of three-body attachment of an electron in the air plasma consists of two stages, first of which is the attachment of electron to the oxygen molecule yielding the excited ion $(O_2^-)^*$ state

$$e + O_2 \rightarrow \left(O_2^- \right)^* \qquad (5.14)$$

In the second stage, the negative ion $\left(O_2^- \right)^*$ is quenched (stabilized) into the stable state O_2^- in collision with the third molecule

$$\left(O_2^-\right)^* + M \rightarrow O_2^- + M,$$
$$\left(O_2^-\right)^* + M \rightarrow e + O_2 + M \qquad (5.15)$$

The highest rates are reported for the electron attachment with the third molecule such as oxygen O_2 or water H_2O molecule. Up to now, there are many experimental and theoretical data for the rate of these processes [62–69], but they are often contradictory, particularly in regard to electron attachment rates in different electric fields.

5.7.1. Measurement of the three-body attachment rate in the laboratory air in external electric field. The technique used for measurement of plasma conductivity in the plasma density range of $n_e = 10^9 \div 10^{16}\,\mathrm{cm}^{-3}$ is described in Subsection 5.1. In brief, the third harmonic of the Ti:Sapphire front-end with the pulse width 100 fs (λ=248 nm) provided a δ–source of free electrons whose loss versus time can be monitored in a pure form. The laser radiation is focused into the inter-electrode gap of the length l=7.85 mm between the tube electrodes with the use of the lens of focal length f=1m. The voltage applied to the gap is varied in the range U=5÷5500 V with electric field ranged from 0.1 to 10 kV/cm. The photocurrent is measured by oscilloscope with the matched input impedance R_{osc}=50 Ω, and specific plasma conductivity is proportional to the oscilloscope signal. Air temperature in experiments was T = 294 K and relative humidity η = 17%.

Typical oscilloscope traces measured for different initial electron densities at the DC external electric field E=6 kV/cm are shown in the **Fig. 5.18a**.

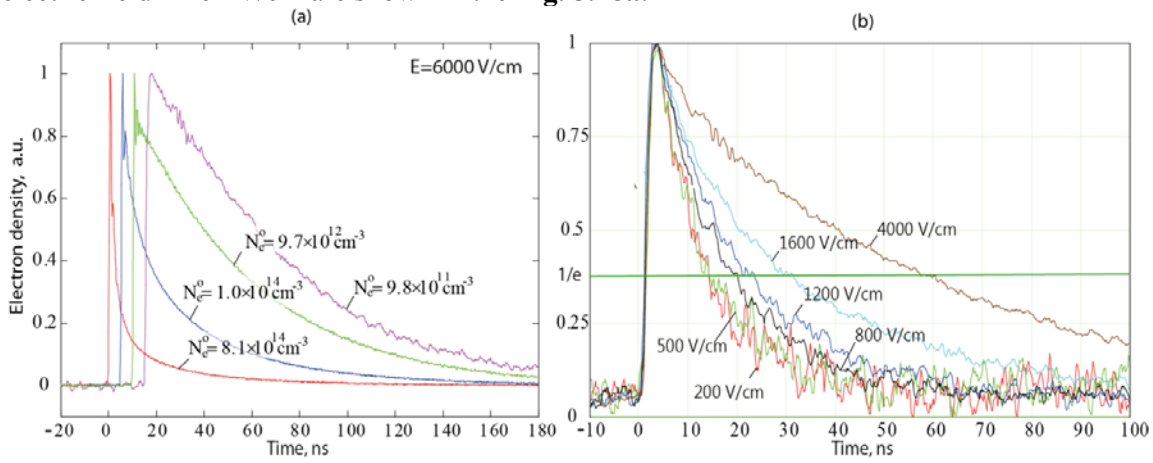

Figure 5.18. (a) Normalized oscilloscope signals measured at different initial electron densities in the DC electric field E=6 kV/cm; **(b)** normalized oscilloscope signals for fixed initial electron density N_{e0}=10^{12} cm^{-3} and different electric field strengths.

For higher initial density of electrons, fast relaxation of electron density with the characteristic time of few nanoseconds is observed indicating electron-ion recombination. At low initial densities $n_{e0} < 10^{13}\mathrm{cm}^{-3}$ all photocurrent signals have the same pulse shape, which is well described by the exponential decay, thus corresponding to electrons attachment to oxygen. A set of oscilloscope traces measured at the same initial electron density $n_{e0} = 10^{12}$ cm^{-3} and different electric field strengths is shown in the **Fig. 5.18b**. Fitting of these curves by exponential law enables us to determine a three-body characteristic attachment time τ_{att}. The

dependence of τ_{att} on the external electric field strength is shown in the **Figs. 5.19, 5.20** jointly with calculated dependencies (see below) at different values of air humidity.

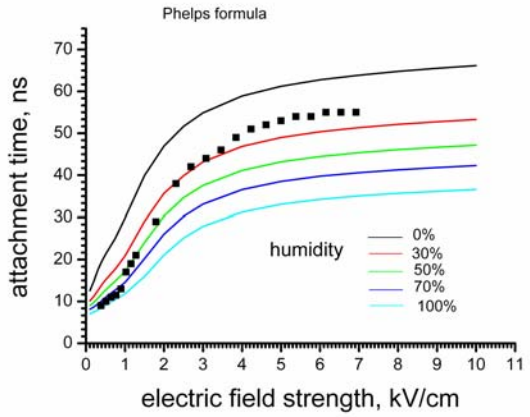

Figure 5.19 The dependence of characteristic attachment time of electrons in weakly ionized air plasma τ_{att} on the DC electric field strength in the inter-electrode gap**.** The curves show the calculated values of τ_{att} at temperature T = 294K and different air humidity, 0%, 30%, 50%, 70% and 100%, respectively. The experimental values are shown by the squares. Calculations are made using A.V. Phelps' formula [68].

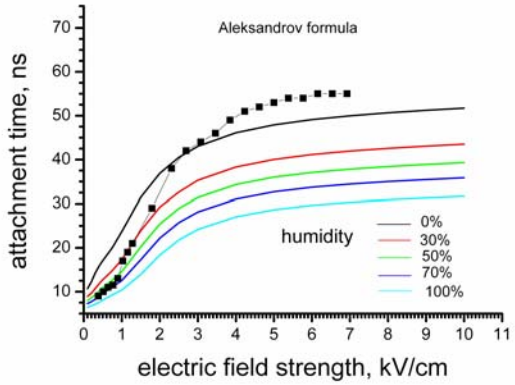

Figure 5.20. The dependence of characteristic attachment time of electrons in weakly ionized air plasma τ_{att} on the DC electric field strength in the inter-electrode gap**.** The curves show the calculated values of τ_{att} at temperature T = 294K and different air humidity, 0%, 30%, 50%, 70% and 100%, respectively. The experimental values are shown by the squares. Calculations are made using N.L. Aleksandrov's formula [62, 69].

5.7.2. Theoretical analysis of electron evolution and attachment in the air plasma in DC electric field. The three-body attachment of an electron in laser plasma in the laboratory air under the DC external electric field has a characteristic time much more larger than that for most of the key elastic and inelastic electron collision processes. The characteristic attachment time is determined by the net electron energy, and to calculate it one can use the steady-state electron energy distribution function.

To determine the quasi-steady state energy spectrum of plasma electrons, we have developed the following simple kinetic model. In the energy domain, the kinetic equation for the electron energy distribution function $n(\varepsilon,t)$ can be written as (see for example, the review [70])

$$\frac{\partial n}{\partial t} = -\frac{\partial}{\partial \varepsilon} j_E + I_{inel} + I_{el} \tag{5.16}$$

Here, the first term in the right hand side is the energy-domain flux j_E which describes the heating of the low-density plasma electrons in the static electric field of the strength E,

$$j_E = u_E(\varepsilon) n(\varepsilon,t) - D_E(\varepsilon)\frac{\partial n}{\partial \varepsilon} \tag{5.17}$$

In the DC electric field, an electron acquires the energy in elastic collisions with gas neutrals which is characterized by the heating rate $u_E(\varepsilon) = (eE)^2 / 6m\nu_T(\varepsilon)$ and the energy diffusion coefficient $D_E(\varepsilon) = \varepsilon(eE)^2 / 3m\nu_T(\varepsilon)$, $\nu_T(\varepsilon)$ is the electron-neutrals momentum-transfer collision rate. Under our experimental conditions, one can easily estimate that the 3D diffusion loss is negligible. Also, the static electric field strength is well below the air breakdown threshold, so that the electron energy distribution function vanishes at energies of collision excitation of electronic states of air components (molecular oxygen and nitrogen). We will neglect also the collision excitation of rotational states. Under these assumption, the inelastic collision term is determined by the vibrational excitation of molecules in collisions with electrons,

$$I_v = -\sum N_k \sum_m [\sigma_{km}(\varepsilon + \hbar\omega_{km})\mathrm{v}(\varepsilon + \hbar\omega_{km}) n(\varepsilon + \hbar\omega_{km}) - \sigma_{km}(\varepsilon)\mathrm{v}(\varepsilon) n(\varepsilon)] \tag{5.18}$$

Summation in Eq. (5.18) is over the vibration states and type of molecules, N_k is the correspondent number density of molecules of type k, $\sigma_{km}(\varepsilon)$ is the cross-section for the excitation of m-th vibration state in collision with the electron of energy ε. Expanding in powers of the ratios of the vibration quanta to the electron energy $\hbar\omega_{km} / \varepsilon$, one can reduce Eq. (5.18) to the form of additional electron flux along the energy axis [70],

$$I_v \cong -\frac{\partial}{\partial \varepsilon} j_v,\ j_v = \nu_v(\varepsilon) n(\varepsilon,t) \tag{5.19}$$

where the effective rate of energy loss by an electron in the collisional excitation of molecular vibrations is

$$\nu_v(\varepsilon) = \sum_{k,m} (2\varepsilon / m)^{1/2} N_k \sigma_{km}(\varepsilon) \hbar\omega_{km} \tag{5.20}$$

The elastic collision integral also can be reduced to the additional flux of electrons in the energy domain,

$$I_{el} \cong -\frac{\partial}{\partial \varepsilon} j_{el},\quad j_{el} = \nu_{el}\left(n(\varepsilon,t) + T_0 \frac{\partial}{\partial \varepsilon}(n/\sqrt{\varepsilon}) \right) \tag{5.21}$$

here the characteristic rate of the energy loss in elastic collisions is $\nu_{el} = \sum_i (2m/M_i)\varepsilon\nu_{Ti}$ and T_0 is the temperature of the laboratory air molecules.

Solution of the kinetic equation (5.16) in the case of atmospheric pressure air and the dominating three-body attachment plasma relaxation regime (i.e., at densities $n_e \le 10^{13}\,\mathrm{cm}^{-3}$) becomes rather rapidly (~ 1 ns) the quasi-stationary function. The electron energy spectrum is then described by Druyvestein-like distribution function

$$n_{st}(\varepsilon) = \sqrt{\varepsilon}\exp\left[-\int_0^{\varepsilon} d\varepsilon \frac{\nu_v(\varepsilon)+\nu_{el}(\varepsilon)}{T_0\nu_{el}(\varepsilon)+D_E(\varepsilon)}\right] \tag{5.22}$$

In our calculations, we modeled the laboratory air of different humidity by the mixture of 79% N_2 and 21% O_2 molecules and the proper number of H_2O molecules at the temperature T_0=294 K. The correspondent electron elastic and inelastic collision cross section data are taken from [71–76]. The calculated according to Eq. (5.22) electron energy spectrum shapes are shown in the **Fig. 5.21** at different electric field strengths.

Using the calculated spectra (5.22) one can find the dependence of the mean electron energy on electric field strength. These dependencies calculated at different air humidity are shown in **Fig. 5.22**. The mean energy of electrons decreases with air humidity which is a consequence of the growth in the electron energy loss in elastic collisions and collisional excitation of water molecule vibrational modes. The difference between the curves in the **Fig. 5.22** is maximal at the field strength of 1kV/cm. With an increase in the field strength the role of energy loss in collisions with water molecules decreases because of the shift of electron energy spectrum out of the domain of effective water molecule excitation, and all the curves converges.

The calculated mean electron energy enables us to determine the characteristic three-body attachment time. The total rate of three-body attachment is calculated as the sum of rates with a) the oxygen molecule as the third body, and b) the water molecule as the third body, as

$$\tau_{att}^{-1} = k_{att\_O_2} N_{O_2}^2 + k_{att\_H_2O} N_{O_2} N_{H_2O} \tag{5.23}$$

here N_{O_2} and N_{H_2O} are the densities of the oxygen and water molecules in the laboratory air, respectively.

We have used two different analytic approximation formulas for the rate of process a), first is given by A.V. Phelps [68]

$$k_{att\_O_2} = 3.6\times10^{-31}\times\left(\frac{1}{T_e}\right)\exp\left(-\frac{0.052}{T_e}\right)\ \mathrm{cm}^6/\mathrm{s} \tag{5.24}$$

here the electron temperature T_e is in eV and is calculated as $T_e = (2/3)<\varepsilon>$.

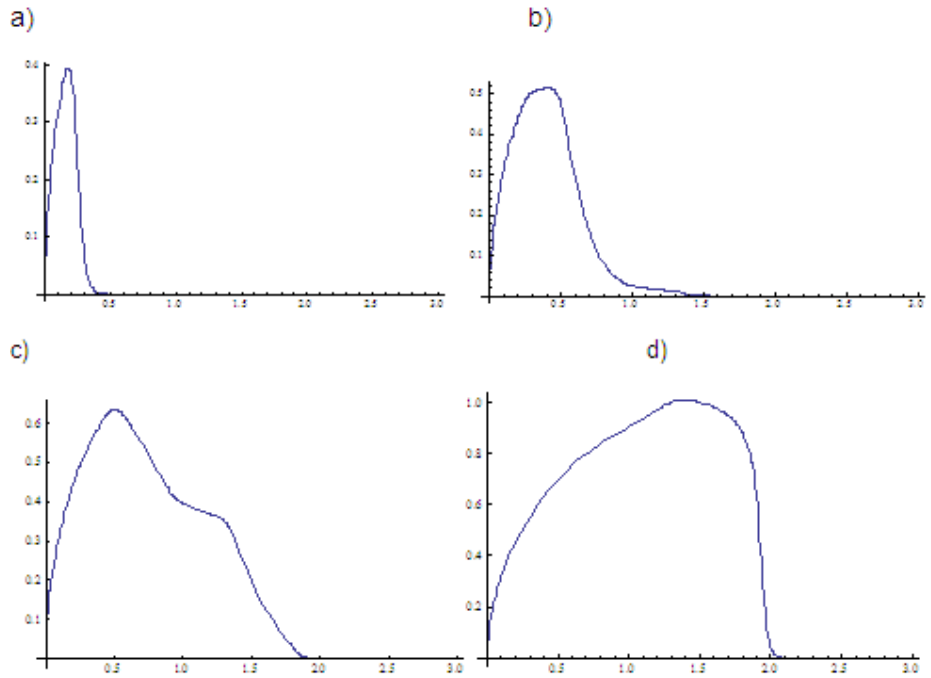

Figure 5.21. The electron energy steady-state spectrum at different DC inter-electrode electric field strengths, E = (a) 0.2 kV/cm; (b) 1 kV/cm; (c) 2 kV/cm and (d) 6 kV/cm. Air humidity is 30%.

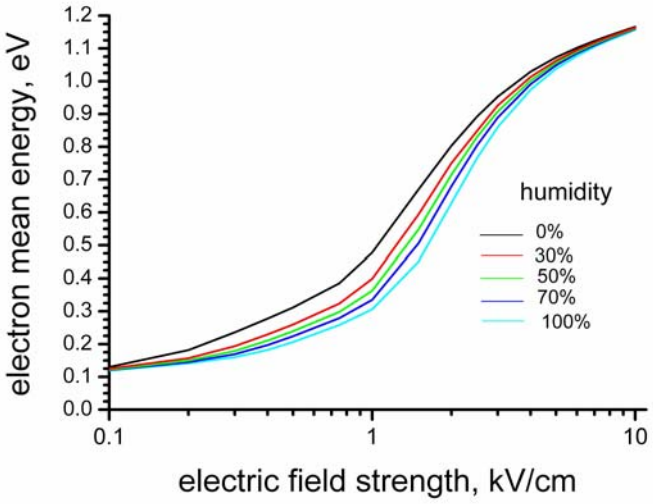

Figure 5.22. The calculated electron mean energy vs. DC electric field strength in the inter-electrode gap at different atmospheric air humidity, 0%, 30%, 50%, 70% and 100%.

The second approximation formula is given by N.L. Alexandrov [62, 69]

$$k_{att\_O_2} = 1.4\times10^{-29}\times\left(\frac{300}{T_e}\right)\exp\left(-\frac{600}{T}\right)\exp\left(\frac{700}{T}-\frac{700}{T_e}\right)\ \text{cm}^6/\text{s} \qquad (5.25)$$

here T and T_e are measured in Kelvin units. In both cases, the rate of attachment process with the water molecule as the third body has been calculated using N.L.Alexandrov's formula [62, 69].

$$k_{att\_H_2O} = 8.5\times10^{-29}\times\left(\frac{300}{T_e}\right)\exp\left(-\frac{600}{T}\right)\exp\left(\frac{700}{T}-\frac{700}{T_e}\right)\ \text{cm}^6/\text{s} \qquad (5.26)$$

It is seen from **Figs. 5.19** and **5.20** that the best fit with the experimental results is found for the approximation (5.24).

The following equation is solved for electron density relaxation

$$\frac{dn_e}{dt} = S_e - \frac{n_e}{\tau_e} - \beta_1 n_e N_{O_2^+} - \beta_2 n_e N_{O_4^+} - \beta_3 n_e N_{N_2^+} - \beta_4 n_e N_{N_4^+}, \qquad (5.27)$$

where $S_e = N_0\sum_j \alpha_j \sigma_j^{(K)} I^K$ is an ionization rate of O_2 and N_2 molecules via MPI and REMPI, $\tau_e \equiv \tau_{att}$ is electrons lifetime in a three-body attachment process. Conversion of primary ions O_2^+ and N_2^+ (processes 5.12) and electron-ion dissociative recombination (5.11) were taken into account with rate constants versus electron temperature dependences (5.13). For short enough laser pulse τ (less than the shortest of the relaxation times) initial electron density $n_e^0 = S_e\cdot\tau$ is set by hands, while corresponding initial concentrations of positive oxygen and nitrogen ions are found from the balance equation $n_e^0 = N_{O_2^+}^0 + N_{N_2^+}^0$ using experimental values for the production rates with accounting for their content in the air.

In **Fig. 5.23** temporal dependences of different plasma components are presented being calculated on the base of Eq. (5.27) without external electric field (***a***) and with the field strength of 2 kV/cm (***b***).

a

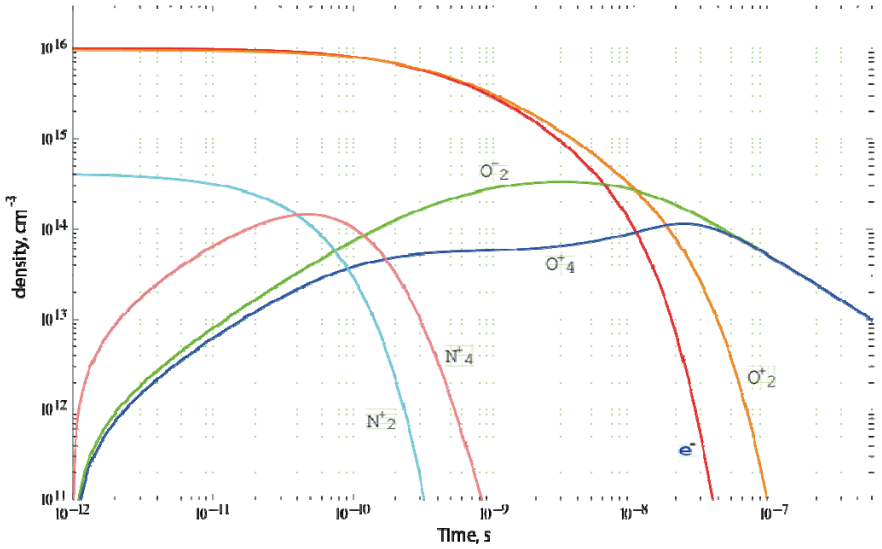

b

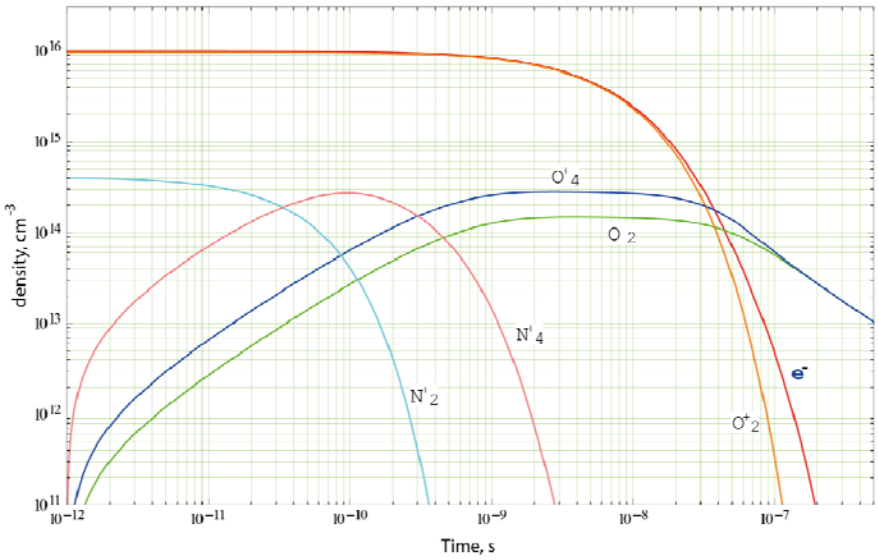

Figure 5.23 Time behavior of the plasma components without external electric field (***a***) and with the field strength 2 kV/cm (***b***).

It is seen that for increased electric field strength both electron attachment to O_2 molecules and their recombination with positive ions O_2^+, O_4^+, N_2^+, and N_4^+ go slower.

6. Theory of ionization of air molecules in the field of high-power KrF laser radiation

Ionization of atmospheric air molecules by UV laser radiation well below the optical breakdown threshold may occur in two modes. The first mode is the direct multi-photon ionization (MPI) of air molecules from the ground state, and the second is the resonance enhanced multi-photon ionization (REMPI) proceeding through an excitation of high-energy upper intermediate molecular states which is followed by one-photon ionization.

6.1. Direct multiphoton ionization of air molecules

The direct multi-photon ionization of air can be estimated on the basis of Keldysh theory [77] using the following relation for the electron density rate

$$\frac{dN_e}{dt} \approx \omega N_0 \sum_j \alpha_j A_j K_j^{3/2} \left(\frac{e^2 E^2}{8m\omega^2 I_j} \right)^{K_j} \tag{6.1}$$

Here, the ionization yield is calculated as a sum over different air components with their ionization potentials I_j and concentration fraction coefficient α_j. In Eq. (6.1), $A_j \sim 1$, ω and E are frequency and electric strength of laser pulse field, K_j is the MPI degree, m is the rest mass of the electron, and N_0 is the density of air molecules.

Standard composition of air at the normal conditions (temperature $15\,^{o}C$ and pressure 101.3 kPa) is shown in the **Table 1**, in which the components are listed with their ionization potentials. In addition, atmospheric air can contain ozone (fraction up to $\alpha_{O_3} \le 10^{-5}$, ionization potential $I_{O_3} = 12.5\,\text{eV}$) and water vapor (fraction is determined by the humidity, ionization potential $I_{H_2O} = 12.621\text{eV}$).

Table 1. The standard air composition.

Gas component	Fraction, %	Ionization potential, eV
N_2	78.084	15.58
O_2	20.9476	12.06
Ar	0.934	15.7596
CO_2	0.0314	14.4
Ne	0.001818	21.56
CH_4	0.0002	12.61
He	0.000524	24.59
Kr	0.000114	13.9996
H_2	0.00005	15.43
Xe	0.0000087	12.13

The direct MPI yield in atmospheric air by 100-ns KrF laser pulse calculated according to Eq. (6.1) is shown in **Fig. 6.1**, in which the density of electrons is plotted as a function of laser intensity.

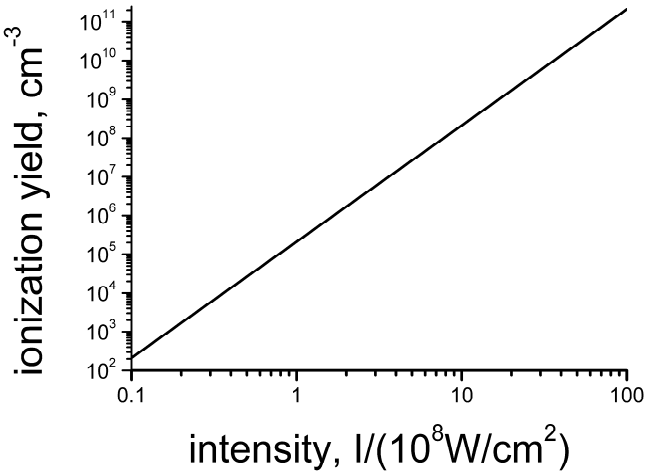

Figure 6.1. Direct multi-photon ionization yield in atmospheric air calculated for 100-ns KrF laser pulse.

6.2. Process of (2 + 1) REMPI in air with KrF laser radiation

Resonance enhanced multi-photon ionization (REMPI) processes can lead to significant enhancement of the ionization yield: Laser-induced excitation of an intermediate electronic state leads to significant enhancement of the ionization rate. Reach vibration spectrum of the

key air components, molecular nitrogen and oxygen, makes available a variety of REMPI channels in the field of high-power UV laser radiation, which have been intensively studied for a long period [18, 78–85]. The most promising REMPI channels are those which proceed through a two-photon excitation of metastable states: The characteristic relaxation time for these states should be sufficiently large to provide coherent interaction with the field of (sufficiently short) laser pulse [81]. The (2 + 1) REMPI in nitrogen through the $^1\Sigma_g^+$ molecular state in the field of ArF laser radiation has been studied experimentally in [50, 51]. Multi-photon ionization of molecular oxygen via two-photon resonant $ns\sigma_g$, $nd\sigma_g$, and $nd\pi_g$ Rydberg levels by KrF laser radiation has been considered in [52].

In the field of KrF laser radiation, ionization of key air components proceeds in (3 + 1) REMPI scheme in nitrogen [50], and in (2 + 1) REMPI scheme in oxygen [78]. As the number of photons needed to ionize O_2 molecule is less than for N_2 molecule, ionization yield in oxygen is higher than in nitrogen. At the laser wavelength $\lambda \approx 248$ nm, (2 + 1) REMPI in O_2 consists of the two-photon excitation of the intermediate relatively long lifetime 3s Rydberg state followed by one-photon ionization [52, 87].

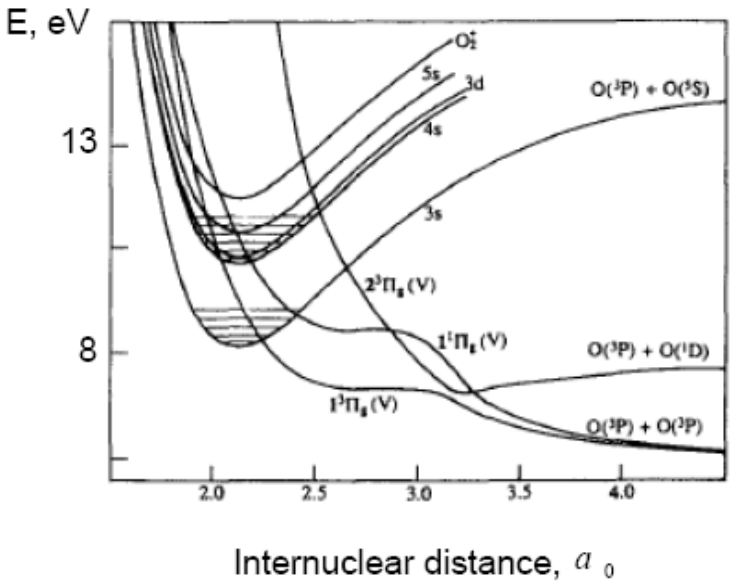

Figure 6.2. Potential energy curves of molecular oxygen corresponding to Rydberg states (taken from [87]).

6.2.1. (2 + 1)REMPI master equations. Theory of laser-matter interaction under the condition of two-photon resonance with subsequent ionization of the excited quantum state has been developed in [86, 88], and the general theory of multi-photon REMPI is given in [89]. Under the slow varying amplitude and phase (SVAP) approximation, assuming $E(z,\tau)$ is the envelope of the laser pulse, $E(z,\tau)\exp[i(\omega t - kz)]$, and $P(z,\tau)$ is the envelope of the polarization of the two-photon transition, $P(z,\tau)\exp[i2(\omega t - kz)]$, one can write down the following system of equations describing evolution of the two-level quantum system in the field of high-power laser radiation under the condition of the two-photon resonance [86, 88]

$$\begin{aligned}
\frac{\partial P}{\partial \tau} &= i\Delta\Omega P - i\frac{r_{12}}{2\hbar}(N_1 - N_2)E^{*2} - \left(\gamma + \frac{1}{T_2}\right)P \\
\frac{\partial N_1}{\partial \tau} &= -2\,\mathrm{Im}\left\{\frac{r_{12}}{2\hbar}E^2 P\right\} - \gamma_1 N_1 - \frac{1-N_1}{T_1}, \\
\frac{\partial N_2}{\partial \tau} &= 2\,\mathrm{Im}\left\{\frac{r_{12}}{2\hbar}E^2 P\right\} - \gamma_2 N_2 - \frac{N_2}{T_1}
\end{aligned} \tag{6.2}$$

Here, N_1 and N_2 are the populations of the ground (1) and excited (2) states of the molecule, respectively. The matrix elements of the two-photon transition (the polarizabilities of the quantum states and the inter-state two-photon transition amplitude) are

$$\begin{aligned}
r_{ii} &= \frac{2}{\hbar}\sum_{l\neq 1,2}\frac{\mu_{il}^2\omega_{li}}{\omega_{li}^2 - \omega^2}, \\
r_{12} &= \frac{1}{\hbar}\sum_{l\neq 1,2}\frac{\mu_{1l}\mu_{l2}}{\omega_{l2} + \omega},
\end{aligned} \tag{6.3}$$

the sum is over the virtual intermediate states through which the two-photon transition between the molecular states 1 and 2 is mediated, μ_{nm} and $\hbar\omega_{mn}$ are the corresponding dipole matrix element and the energy of the virtual transition. The photo-ionization width of the correspondent state is $\gamma_i = \mathrm{Im}(r_{ii}/\hbar)|E|^2$, i=1, 2, the parameter $\gamma = (\gamma_1 + \gamma_2)/2$, and the characteristic transversal and longitudinal relaxation (i.e., the characteristic polarization and density population relaxation times) are T_2 and T_1, respectively. The detuning $\Delta\Omega = (2\omega - \omega_{12}) + (1/2\hbar)\,\mathrm{Re}(r_{22} - r_{11})|E|^2$ takes into account the shift of the laser frequency from exact two-photon resonance and the ac Stark shift.

In our case of interest, the ground state of the oxygen molecule is $X^3\Sigma_g^-$ and the excited state is 3*s* Rydberg state, $C^3\Pi_g$. Hence, the ionization width γ_1 is negligible, and the ionization yield due to one-photon ionization of the Rydberg state is determined by the following equation

$$\frac{\partial N_i}{\partial \tau} = \gamma_2 N_2 \tag{6.4}$$

The population relaxation time T_1 in the case of (dipole-forbidden) two-photon transition is sufficiently high and well exceeds pulse duration even for 100-ns laser pulses. The corresponding relaxation terms in the second and in the third equation of the system (6.2) can be omitted.

Depending on the relation between the laser pulse duration τ_p and the characteristic polarization relaxation time T_2, one should distinguish two qualitatively different interaction regimes, coherent and non-coherent. In the dense atmospheric pressure gases, the characteristic time T_2 is determined mainly by collisions of excited molecule with free electrons of weekly-ionized plasma or with other molecules. The regime of coherent interaction is thus specific for ultra-short laser pulse of sub-picosecond duration or shorter, $\tau_p << T_2$.

6.2.2. Coherent interaction regime. We will restrict ourselves by the case of exact resonance $\Delta\Omega \approx 0$. The system of equations (6.2) then can be integrated exactly [86]. We rewrite the master system (6.2) in the following dimensionless form

$$\begin{aligned}
&\frac{\partial P}{\partial \xi} = -\frac{1}{2}(N_2 - N_1)F^2 - \alpha F^2 P, \\
&\frac{\partial N_1}{\partial \xi} = -PF^2, \\
&\frac{\partial N_2}{\partial \xi} = PF^2 - 2\alpha F^2 N_2
\end{aligned} \tag{6.5}$$

Here, the polarization is considered to be purely imaginary (its real part is infinitesimal), the dimensionless field amplitude is $F^2 = \tau_p r_{12} E^2 / \hbar$, the intrinsic time is normalized by the pulse duration, $\xi = \tau / \tau_p$, and the parameter $\alpha = (16\pi r_{12}\omega / c)^{-1}\sigma_i$ is the ratio of the one-photon ionization rate (with the characteristic cross-section σ_i) to the rate of the two-photon excitation. The initial ($\xi \to -\infty$) conditions to the system (6.5) are $P = N_2 = 0$ and $N_1 = 1$, which correspond to initially non-excited molecules. Introducing the instantaneous (cumulative) pulse energy flux,

$$S(\tau) = \int_{-\infty}^{\tau/\tau_p} F^2 d\xi, \tag{6.6}$$

one can find the following exact solution of Eqs. (6.5),

$$P = \begin{cases} \left[\dfrac{\alpha}{\nu^2}\sin^2(\nu S/2) + \dfrac{1}{2\nu}\sin(\nu S)\right]\exp[-\alpha S], & \alpha<1 \\ \left[\dfrac{\alpha}{\delta^2}\sinh^2(\delta S/2) + \dfrac{1}{2\delta}\sinh(\delta S)\right]\exp[-\alpha S], & \alpha>1 \end{cases}$$

$$N_1 = \begin{cases} \dfrac{1}{\nu^2}\left[\alpha\sin(\nu S/2) + \nu\cos(\nu S/2)\right]^2\exp[-\alpha S], & \alpha<1 \\ \dfrac{1}{\delta^2}\left[\alpha\sinh(\delta S/2) + \delta\cosh(\delta S/2)\right]^2\exp[-\alpha S], & \alpha>1 \end{cases} \tag{6.7}$$

$$N_2 = \begin{cases} \dfrac{1}{\nu^2}\sin^2(\nu S/2)\exp[-\alpha S], & \alpha<1 \\ \dfrac{1}{\delta^2}\sinh^2(\delta S/2)\exp[-\alpha S], & \alpha>1 \end{cases}$$

here the parameters $\nu = (1-\alpha^2)^{1/2}$ and $\delta = (\alpha^2 - 1)^{1/2}$ are introduced in the cases α<1 and α>1, respectively. The ionization yield by the end of the laser pulse can be defined in this case as $N_i = 1 - (N_1 + N_2)$, and we find

$$N_i = \begin{cases} 1-\left(1+\dfrac{\alpha}{\nu}\sin(\nu W)+2\dfrac{\alpha^2}{\nu^2}\sin^2\left(\dfrac{\nu W}{2}\right)\right)\exp[-\alpha W], & \alpha<1 \\ 1-\left(1+\dfrac{\alpha}{\delta}\sinh(\delta W)+2\dfrac{\alpha^2}{\delta^2}\sinh^2\left(\dfrac{\delta W}{2}\right)\right)\exp[-\alpha W], & \alpha>1 \end{cases} \tag{6.8}$$

Here $W = S|_{\xi\to+\infty}$ is the total energy flux of the laser pulse. When the ultrashort pulse energy flux is small, $\nu W << 1$, $\delta W << 1$, one can easily find that the ionization yield scales as the pulse energy flux to the third power,

$$N_i \approx \frac{1}{6}\alpha W^3 \tag{6.9}$$

which coincides with the scaling law for the direct three-photon ionization process. However, the two-step ionization process will definitely prevail with respect to the direct three-photon ionization because of the fact that values of corresponding matrix elements for *real* transitions well exceeds those for *virtual* transitions, compare (6.9) and (6.1),

$$\frac{1}{6}\frac{\sigma_i I_{12}^2 \tau_p^3}{16\pi\omega} >> 3^{3/2}\omega\tau_p\left(\frac{e^2}{8m\omega^2 I_{O_2}}\right)^3 \tag{6.10}$$

We have to point out the following interesting property of the exact solution (6.7). In the case of a small ratio of the one-photon ionization rate to the rate of the two-photon excitation, $\alpha<<1$, the coherent oscillations of population densities and polarization of the two-photon transition emerge. In this case, the specific π- and 2π-pulse interaction regimes are realizing [86].

When the pulse energy satisfy the π-pulse condition,

$$\nu W = \pi + 2\pi m, \quad m = 0,1,2,.. \tag{6.11}$$

almost all the molecules remain excited by the end of the laser pulse, $N_2 = \nu^{-2}\exp[-\alpha W] >> N_1$. The rate of ionization yield is then maximal and scales linearly with the laser intensity,

$$\frac{\partial N_i}{\partial \tau} = 2\alpha F^2 N_2 \propto (2\alpha/\nu^2)F^2 \tag{6.12}$$

The most effective ionization regime is realized for the 2π-pulse interaction regime, when

$$\nu W = 2\pi m, \quad m = 0,1,2,.. \tag{6.13}$$

In this case, most of the molecules become unexcited to the end of the laser pulse,

$$N_2|_{\xi\to+\infty} = 0 \tag{6.14}$$

and all amount of energy lost by the laser pulse is spent for the ionization only,

$$N_i = 1 - \exp[-\alpha W] \approx \alpha W \tag{6.15}$$

Thus, the ionization yield in this regime also scales linearly with the pulse energy (or laser intensity) [86].

6.2.3. Non-Coherent interaction regime. When the duration of the laser pulse well exceeds the characteristic polarization relaxation time T_2, $\tau_p >> T_2$, the laser-molecule interaction proceeds in the non-coherent regime. In this regime, the polarization of the two-photon resonance molecular transition can be adiabatically excluded from the system of equations (6.2),

$$P \approx -i\frac{r_{12}}{2\hbar}(N_1 - N_2)E^{*2}\frac{(\gamma + 1/T_2) + i\Delta\Omega}{(\gamma + 1/T_2)^2 + (\Delta\Omega)^2} \tag{6.16}$$

As a result, the dynamics of (2 + 1) REMPI in the non-coherent case is described by the following system of rate equations,

$$\begin{aligned}
\frac{\partial N_1}{\partial t} &= -\mu\frac{\gamma + 1/T_2}{(\gamma + 1/T_2)^2 + (\Delta\Omega)^2}(N_1 - N_2), \\
\frac{\partial N_2}{\partial t} &= \mu\frac{\gamma + 1/T_2}{(\gamma + 1/T_2)^2 + (\Delta\Omega)^2}(N_1 - N_2) - 2\gamma N_2, \\
\frac{\partial N_i}{\partial t} &= 2\gamma N_2
\end{aligned} \tag{6.17}$$

the coefficient $\mu = \frac{1}{2}\left(\frac{r_{12}}{\hbar}\right)^2 |E|^4$ characterizes the strength of the two-photon transition.

We will assume the most interesting from the practical point of view situation when the nanosecond laser pulse produces the low-density plasma, $N_2 << N_1$.

When the laser pulse intensity is sufficiently small and the detuning from the two-photon resonance is large, so that the probability of the two-photon transition is small during the laser pulse, we find the ionization rate is given by the relation

$$\frac{\partial N_i}{\partial t} \approx 2\gamma\int_{-\infty}^{t}\mu(t')T_2\frac{1}{1 + (\Delta\Omega T_2)^2}dt' \tag{6.18}$$

and one can estimate the ionization yield during the laser pulse as

$$N_i \approx \gamma\mu T_2\tau_p^2\frac{1}{1 + (\Delta\Omega T_2)^2} \approx \left(\frac{4\pi r_{12}\omega}{c}\right)^2\sigma_i T_2\tau_p^2\left(\frac{I}{\hbar\omega}\right)^3\frac{1}{1 + (\Delta\Omega T_2)^2} \tag{6.19}$$

where I is the laser pulse intensity.

When the excitation and photoionization rates are larger than τ_p^{-1} and the parameter $\alpha << 1$, populations of the ground and excited molecular states exhibit oscillations with the characteristic Rabi frequency

$$\Omega_R \sim \mu \frac{\gamma + 1/T_2}{(\gamma + 1/T_2)^2 + (\Delta\Omega)^2} \tag{6.20}$$

In this case, however, the laser intensity should be rather large to provide the high excitation probability.

Photo-ionization cross section for the high-energy Rydberg state is usually rather large, so for the most interesting practical situations the other limiting case $\alpha >> 1$ can be realized. Assuming the population of the excited state is small, $N_2 << N_1$, one can find from Eqs. (6.17) the quasi steady-state solution

$$N_2 \approx \frac{1}{2}\frac{\mu}{\gamma}\frac{\gamma + 1/T_2}{(\gamma + 1/T_2)^2 + (\Delta\Omega)^2} \tag{6.21}$$

Depending on the relation between three characteristic parameters of the problem at hand, the (intensity-dependent) photo-ionization rate γ, the polarization relaxation time T_2, and the frequency detuning $\Delta\Omega$ (which, in general, is also intensity-dependent through the ac Stark shift), various interaction regimes and ionization yield scaling laws become available.

At low laser radiation intensities $\gamma << 1/T_2$, one can easily see from Eq. (6.21) that the population of the excited Rydberg state grows linearly with the intensity,

$$N_2 \approx \frac{1}{2}\frac{\mu}{\gamma} T_2 \frac{1}{1 + (\Delta\Omega T_2)^2} \propto I \tag{6.22}$$

and hence the ionization rate scales as $\partial N_i / \partial t \propto I^2$. For the UV KrF laser radiation ($\lambda = 248nm$), the threshold intensity $\gamma T_2 \sim 1$ at $T_2 \sim 1$ps gives the value $I \sim 1.6 \times 10^{-6}$ W$/\sigma_i$ that for the cross-section $\sigma_i \sim 10^{-17}$cm^2 is $I \sim 1.6 \times 10^{11}$ W/cm^2. This estimate is in good agreement with our experimental results in which the ionization yield in atmospheric air scales as squared intensity in the domain $4 \times 10^8 \div 10^{11}$ W/cm^2 for 20-ns KrF laser pulses.

With the increase in intensity $\gamma >> 1/T_2$ at large frequency detuning $\gamma << \Delta\Omega$ we find

$$N_2 \approx \frac{\mu}{2(\Delta\Omega)^2} \propto I^2 \tag{6.23}$$

and the ionization rate scales as the cubic intensity, $\partial N_i / \partial t \propto I^3$. Finally, when $\gamma >> 1/T_2$ and $\gamma >> \Delta\Omega$, the population of the Rydberg state reaches its saturation,

$$N_2 \approx \frac{1}{2}\frac{\mu}{\gamma^2} \propto const(I) \tag{6.24}$$

The ionization rate is thus linear function of laser intensity, $\partial N_i / \partial t \propto I$.

6.3 Self-focusing and filamentation of UV KrF laser pulses under the dominant (2 + 1) REMPI interaction regime

In the regime of dominant (2 + 1) REMPI, the nonlinear polarization of the air is determined by resonant two-photon excitation of an intermediate Rydberg state of oxygen molecules rather than the nonresonant Kerr nonlinear polarization. Hence, the self-focusing of the ultra-short UV laser pulse proceeds in a manner different from conventional one [37–39]. When the pulse duration is shorter than the characteristic polarization relaxation time of the resonant two-photon transition T_2, i.e., when the interaction proceeds in the coherent regime (see 6.2.2), the normalized polarization according to Eq. (6.7) can be approximated as ($\alpha << 1$)

$$P(x,r,\tau) \approx \frac{1}{2}\sin S(x,r,\tau), \tag{6.25}$$

with the pulse area *S* given by Eq. (6.6). To deal with the self-focusing, we assume the smooth radial profile of the laser pulse, and as a result of Eq. (6.25) the smooth radial profile of the nonlinear polarization. The form of nonlinearity (6.25) enables us to conclude that the self-focusing process has to reveal quite different features than that for non-resonant Kerr nonlinearity. In the case of our interest the polarization depends on cumulative variable, the pulse area *S,* which is essentially non-local in time, rather than the immediate response in the case of Kerr nonlinearity [37–39].

To describe laser pulse propagation effects, we have to solve the wave equation which under the slow varying amplitude and phase approximation can be written in the following form

$$\frac{\partial E}{\partial x} - i\frac{c}{2\omega}\Delta_{\perp}E = -\frac{1}{L_s}PE - \frac{\alpha}{L_s}N_2E \tag{6.26}$$

here $L_s = (4\pi\omega N r_{12} / c)^{-1}$ is the characteristic two-photon absorption length, *N* is the density of resonant molecules. The pulse envelope function *f* is introduced by assuming the laser pulse field profile of a transverse Gaussian shape

$$E(r,x,\tau) = \frac{E_0(\tau)}{f(x,\tau)}\exp\left[-\frac{r^2}{2R_0^2 f^2(x,\tau)}\right]\exp(-is), \tag{6.27}$$

here R_0 is the laser beam initial radius, and *s* is the eikonal function [90].

Using the near-axis paraxial ray approximation and aberration-free approximation [90], one can derive the following equation for the transverse envelope function of the ultra-short laser pulse,

$$R_0^2\left(\frac{\partial f}{\partial x}\right)^2 + \left(\frac{1}{k_0^2 R_0^2 f^2} - \frac{1}{2k_0 L_s}\sin\left[\int_{-\infty}^{\tau/\tau_p}\frac{F_0^{\,2}(\xi)}{f^2(x,\xi)}d\xi\right]\right) = const \tag{6.28}$$

On the initial stage of self-focusing, when variation of the transverse shape of the ultra-short laser pulse is rather small, $|1 - f|=1$, the integration constant in the right hand side of Eq. (6.28) is determined by the initial conditions at $x=0$, i.e., can be written as

$$R_0^2 \tan^2 \Theta + \left(\frac{1}{k_0^2 R_0^2} - \frac{1}{2k_0 L_s} \sin\left[\int_{-\infty}^{\tau} F_0^{\,2}(\tau) d\tau \right] \right) \tag{6.29}$$

here Θ is the angle of initial focusing, determined by the focal length Z, $\tan\Theta = R_0 / Z$. Below, we will restrict ourselves by the case of zero focusing angle $\Theta = 0$.

Substituting (6.29) into the right hand side of Eq. (6.28), we find in the limit $|1 - f|=1$

$$\frac{1}{4} R_0^2 \left(\frac{\partial f^2}{\partial x} \right)^2 + \left(\frac{1}{k_0^2 R_0^2} - \frac{\Phi \cos\Phi}{2k_0 L_s} \right)(1 - f^2) = 0 \tag{6.30}$$

where $\Phi = \int_{-\infty}^{\tau} F_0^{\,2}(\tau) d\tau$ is the on-axis instantaneous (cumulative) fluence of the laser pulse. One can easily find the solution to Eq. (6.30)

$$f(x,\tau) = \left[1 + (x / L_{diff})^2 - (x / L_f)^2 \Phi \cos\Phi \right]^{1/2} \tag{6.31}$$

where the diffraction length $L_{diff} = k_0 R_0^2$ and the self-focusing characteristic length $L_f = \sqrt{2 L_s L_{diff}}$ are introduced. According to Eq. (6.31), the leading edge of the laser pulse, for which the cumulative fluence is small, exhibits the diffraction-like spread in the transverse direction, $f \sim (1 + x^2 / L_{diff}^2)^{1/2}$. With an increase in fluence, since $\Phi \geq (L_f / L_{diff})^2 = 2L_s / L_{diff}$ laser pulse starts self-induced focusing. If the initial intensity of the USP is large enough, so that the cumulative fluence reaches the value $\Phi = \pi / 2$, the cosine function changes its sign, and the self-induced defocusing of the proper part of the pulse starts. When $\Phi >> 1$, the laser pulse exhibit alternating self-induced focusing and defocusing, according to Eq. (6.31).

In **Fig. 6.3**, the envelope f is shown as a function of cumulative fluence at different propagation distances of the ultrashort laser pulse. Calculations are restricted to propagation distances of $x / L_f \leq 1.45$. With further increase in distance, rapid collapse of the pulse envelope function arises which leads to the breaking up the validity conditions for the envelope equation (6.30). Propagation over the longer distances should be considered using exact wave equation taking into account a significant phase shifts produced by the eikonal function s (see Eq. (6.27)), possibly with a modified paraxial ray approximation.

We have to point out two distinctive features of the filamentation process of the ultrashort UV laser pulse under the dominant (2 + 1) REMPI regime. First, the transverse radius of the filament is determined by a balance between the self-induced focusing process and the defocusing. Defocusing of the laser pulse in the non-resonant medium is related to the electron refraction in plasma, which emerges as a result of the multi-photon ionization of medium molecules in the leading front of the laser pulse. Under the dominant (2 + 1) REMPI process,

defocusing arises with the change of sign in the polarization function (6.25) with an increase in the laser pulse cumulative fluence.

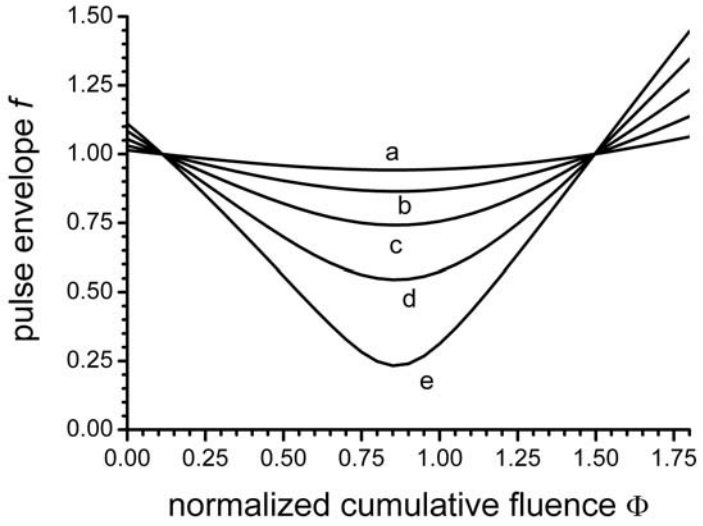

Figure 6.3. The laser pulse envelope as a function of normalized cumulative fluence Φ at different pulse propagation distances: $x/L_f =$ (a) 0.5, (b) 0.75, (c) 1.0, (d) 1.25, (e) 1.45. Calculations are made at diffraction to self-focusing lengths ratio $L_{diff}/L_f = \sqrt{kR_0^2/2L_s} = 3$.

The second distinctive feature is that the threshold for self-focusing in the case of our interest is determined by the total energy of the laser pulse rather than its power, in contrast with filamentation under the non-resonant Kerr-dominated nonlinearity [37–39]. Threshold of the self-focusing can be estimated as follows. Assuming the pulse area S be sufficiently small, so as $\sin S \approx S$ and $f \approx 1$ at the beginning stage of the self-focusing, one can find that the second term in the left hand side of Eq. (6.28) becomes negative when the energy of the laser pulse exceeds the threshold value

$$W_{th} = \hbar c N L_s^2 \tag{6.32}$$

Taking for estimate $r_{12} \sim 10^{-24} - 10^{-25}$ cm^3 and KrF laser radiation ($\lambda = 248$ nm), we have the threshold energy of the order of 10^{-6} J.

7. Long plasma channels in air produced by combined UV laser radiation

The experiments are performed with the hybrid Ti:Sapphire/KrF laser facility described in Section 3. At the output a 100-ns pulse of a free-running lasing is obtained with energy of several tens of joules, which is overlapped with amplified short-pulse train, with peak power as high as 0.2÷0.3 TW, repeated with the resonator round-trip time ~17 ns (upper trace in **Fig. 7.1a)**. Remind that amplitudes of short-pulses (~1 ps) in the oscilloscope traces are ~10^3 times less than the real ones. In the case when a ring cavity of the short-pulse multiplier is blocked, only a single pulse is generated and injected into the unstable resonator, with rarely modulated

output radiation observed at the output (upper trace in **Fig. 7.1b)**. Without any injection only the free-running oscillation pulse of ~100 ns duration is produced (upper trace in **Fig. 7.1c)**. Thus we can experimentally compare air ionization by differently modulated UV radiation with approximately equal total energy of the laser pulse up to 30 J.

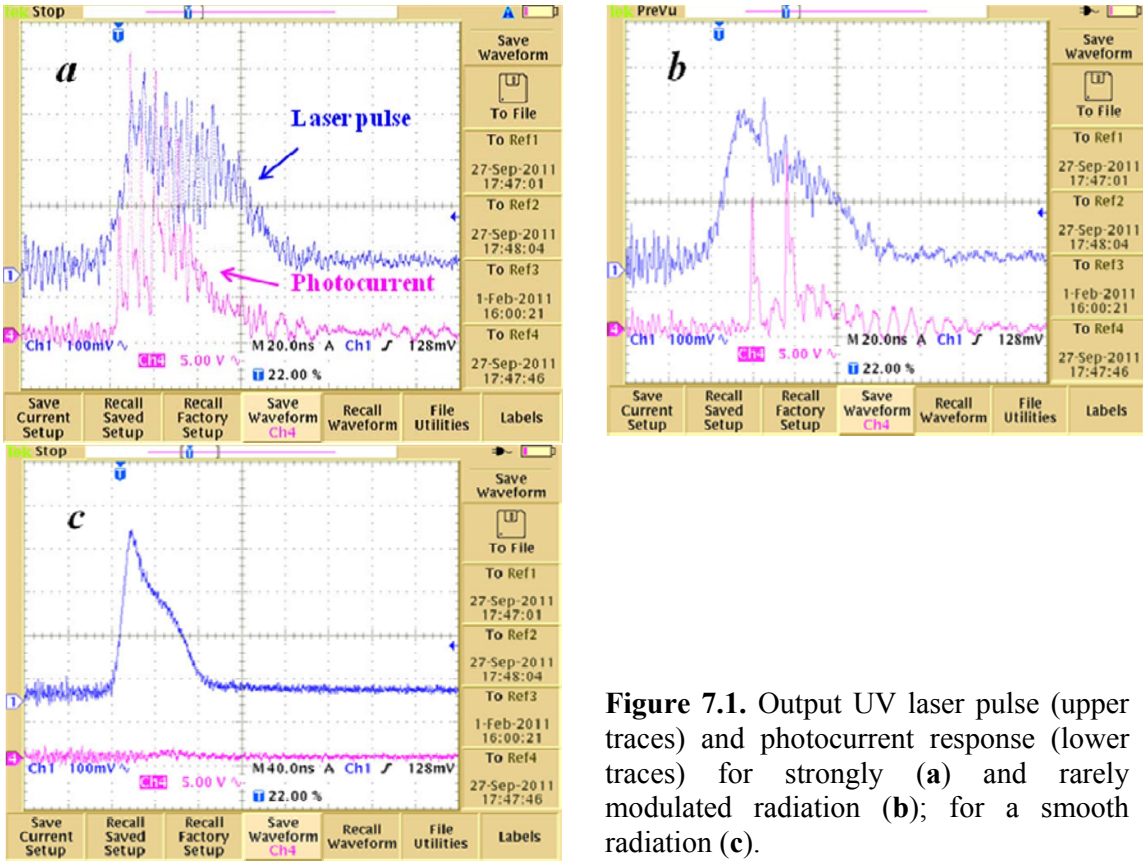

Figure 7.1. Output UV laser pulse (upper traces) and photocurrent response (lower traces) for strongly (**a**) and rarely modulated radiation (**b**); for a smooth radiation (**c**).

A layout of plasma conductivity measurements is shown in **Fig. 7.2**. A spherical mirror with a focal length of F=8 m focused a slightly convergent output laser beam in such a way that a geometric focus is at the distance of 6.75 m from the mirror. Two spherical electrodes of 5-cm diameter are set at L=20 cm distance. Laser radiation is directed into inter-electrode gap through 1-cm in diameter holes in the electrodes. A fast photocurrent response at the 50-Ohm oscilloscope input is proportional to the applied DC voltage of U=5–22 kV, and it is related to electron component of the plasma. Short spikes of 2-ns FWHM duration are observed in oscilloscope traces (lower traces in **Figs. 7.1a, 7.1b)** being synchronous with the short-pulse train. These photocurrent peaks are 100 times higher than the photocurrent value measured for 100-ns smooth laser pulse in a free-running lasing (**Fig. 7.1c**). For strongly modulated UV laser pulse a quasi-steady basement in the photocurrent response, which increases in time, is more pronounced, if compare with rarely modulated laser pulse. Apparently, this effect of the pulse train evidences about the certain accumulation of electrons.

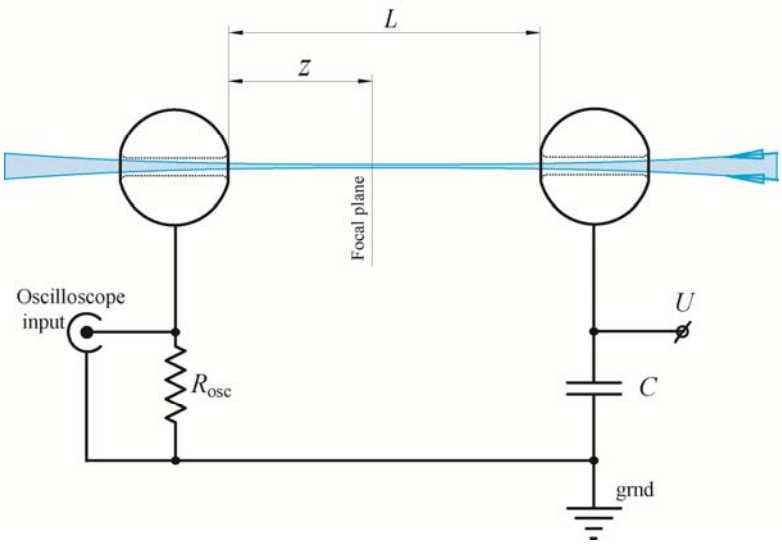

Figure 7.2. Layout of photocurrent measurements.

The dependence of the photocurrent amplitude on the position of geometric focus relative to the inter-electrode gap at applied voltage U=5 kV is shown in **Fig. 7.3**. Zero coordinate z=0 corresponds to the geometric focus coinciding with the ground electrode. It is seen that plasma conductivity exists along about ~100-cm length that coincides with our photocurrent measurements of the filamentation length (see Section 4) for a single short pulse.

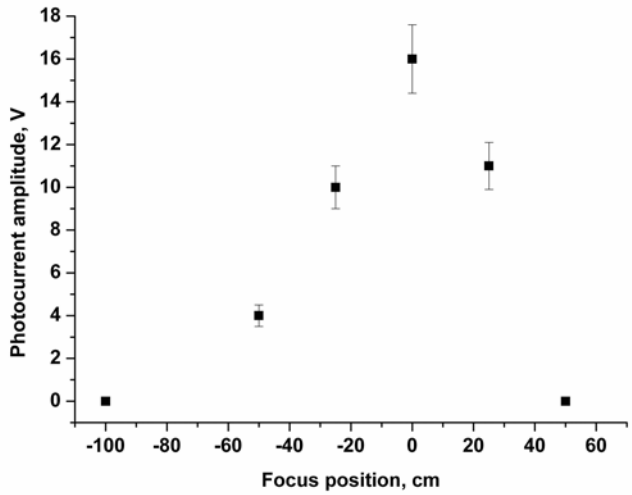

Figure 7.3. Photocurrent amplitude in dependence on focus position at U=5 kV.

An average conductivity of the plasma channel can be estimated from the photocurrent measurements, and energy distribution of laser radiation near the focus is shown in **Fig. 7.4.** The laser energy distribution is measured in the same manner as described in Section 4 – fluorescence of a glass plate under UV irradiation is imaged on a time-gated CCD. The laser beam profiles are demonstrated for 50-cm distance before the focus (***a, b***), for a focal plane (***c***), and for 50-cm distance behind the focus (***d***). These measurements are carried out for a single short pulse (***a, d***) and a train of 3 short pulses following with a time interval ~ 5 ns (***b, c***) without any 100-ns background lasing. In this performance a short-pulse train (or a single pulse) are amplified consequently in both double-pass Berdysh and GARPUN amplifiers.

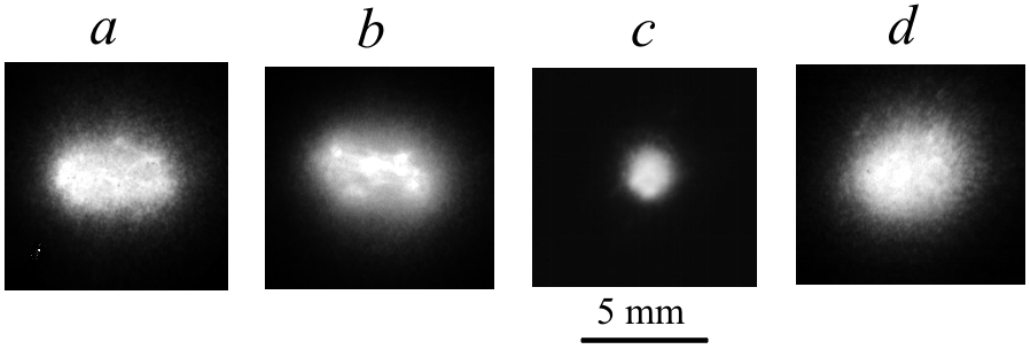

Figure 7.4. Laser beam profiles for different distances from the focus: 50 cm before the focus (***a, b***), in the focus (***c***), and 50 cm behind the focus (***d***). ***a, d*** – measurements for a single short pulse; ***b, c*** – for the train of 3 pulses

The filamentation of the beam is pronouncedly seen in the cross sections of the beam before the focus, and it is smoothed after the focus (in detail the process of filamentation has been described in Section 4). Also, for a short-pulse train uniformity of the beam profile is higher as a result of increased interaction of consequent short pulses with plasma filaments created by the previous ones.

An average diameter of the beam increased about 3 times at 50-cm distances apart from the focus. The length of the beam waist, where the cross section area slightly changed, is measured to be ~40 cm. It means that we can consider the diameter of the waist as 1 mm and corresponding area S=0.8*10^{-2} см^2 for photocurrent measurements around the geometric focus.

To estimate the average plasma conductivity and electron density along the beam waist we assume from **Fig. 7.3** the maximum photocurrent signal u=15 V (z=0), which for oscilloscope input R_{osc} =50 Ohm corresponds a photocurrent I=0.3 A through the plasma channel. The resistivity of the plasma is $R = U/I$ =17 kOhm, and a specific electron conductivity $\sigma_e = L/RS = 0.16$ (Ohm·cm)$^{-1}$. Then the electron density can be found as $n_e = \sigma_e/e\mu_e \approx 1.6\cdot10^{15}$ cm^{-3} with assumed electron mobility in atmospheric-pressure air $\mu_e \approx 600$ cm^2·(V·s)$^{-1}$ [45, 46]. Note, that the local conductivity and electron density in filaments might be at least an order of magnitude higher (see, e.g., [38]).

Thus the most effective air ionization is observed for a strongly modulated radiation pulse produced under regenerative amplification of the USP train. Let us analyze this favorable regime in more detail.

Figure 7.5 compares photocurrent signals (upper traces) produced in atmospheric pressure air by the amplified USP train (without quasi-steady lasing) and the combined amplitude-modulated laser pulse (lower traces). The former is obtained when the USP train is injected into the resonator with a misaligned output meniscus lens coupler i.e. actually in a double-pass amplification mode. In the latter case, the reflecting coupler is perfectly aligned, and a multi-pass regenerative amplification mode is realized.

The photocurrent peaks that are synchronous with laser radiation spikes have the same maximal amplitude in both cases. The corresponding electron density in the plasma channel is

estimated as n_{emax}=1.6×10^{15} cm^{-3}. Because of the limited temporal resolution of our measurement scheme (~1ns), n_{emax} might be significantly less than the initial values n_{e0} at the moment of the USP passage. The photocurrent peaks duration at the FWHM ~2 ns, on the contrary, exceeds temporal resolution, and thus it is a characteristic time of plasma relaxation via dissociative electron-ion recombination dominating at sufficiently high electron concentration $n_e \geq n_e^*$ = 10^{14}÷10^{15} cm^{-3}. In the case of combined amplitude-modulated radiation, one can observe a pedestal between the peaks, which is 3÷5 times less than the peak values and corresponds to n_e = (3÷5)×10^{14} см$^{-3}$. A quasi-steady constituent of photocurrent evidences the change of dominant relaxation process of electron attachment to oxygen molecules at lower densities $n_e \leq n_e^*$ and establishment of an equilibrium with reverse electron photodetachment process under quasi-steady laser radiation.

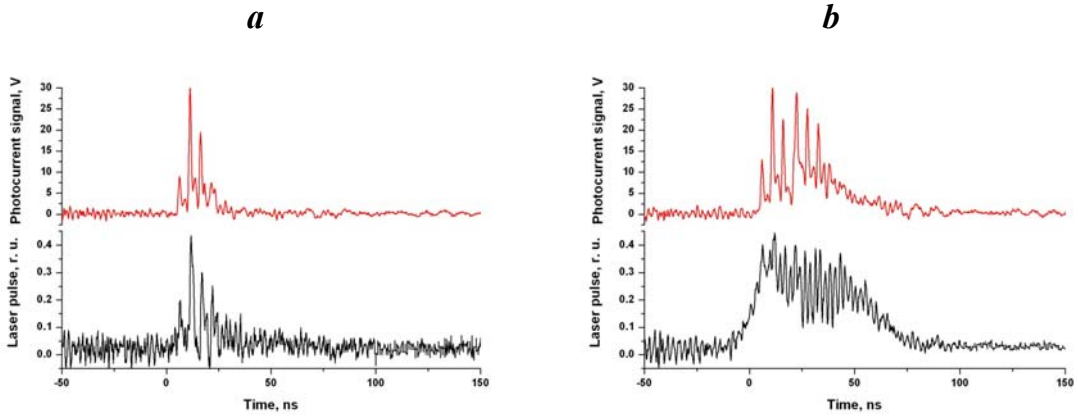

Figure 7.5. UV laser pulse (upper traces) and photocurrent signals (upper traces) produced by USP pulse train (***a***) and combined amplitude-modulated radiation (***b***).

8. Guiding long-distance HV electric discharges by combined subpicosecond and nanosecond UV pulses

It has been demonstrated that the hybrid terawatt Ti:Sapphire/KrF laser facility GARPUN-MTW is capable to generate UV USP of sub-TW peak power and temporal width of 0.5 – 1.0 ps, as well as 100-ns long amplitude-modulated pulses with energy of several tens joules (see Sections 2 and 3). These allow us to produce ~1-m-long plasma channels maintained for ~100 ns with conductivity 100 times higher than that for a smooth 100-ns non-modulated pulse (Section 6). Such regimes enable us to keep rather high electron density for fairly long time (~100 ns) and seem to be favorable to trigger HV electric discharge more effectively.

8.1. Pilot experiments on UV laser-induced air discharge in DC electric field

Beginning experiments are performed with a discharge gap formed by two semispherical electrodes of 15-mm radii with applied DC voltage of U=50 kV (**Fig. 8.1a**). UV laser pulses with up to 30-J energy, 100-ns duration and with different waveforms are focused by F=8-m spherical mirror in the center of grounded electrode and tangentially to the HV electrode. The discharge current is measured by means of Rogovski coil, which enfolded the ground electrode mount. A breakdown delay time relative to the laser pulse is determined in a comparison of discharge current oscilloscope traces (upper traces in **Fig. 8.2**) with photodetector signals showing both laser pulses (shot spikes in the beginning of bottom traces in **Fig. 8.2**) and luminescence of the discharge plasma (the following broader pulses).

The maximal interelectrode distance for which HV breakdown is still observed with 100% probability without any UV laser illumination is l =1.5 cm which corresponds to average electric field strength in the gap $E=U/l\approx$30 kV/cm, typical for the breakdown of dry air in the uniform field. Laser-triggered breakdown in the case of a smooth UV laser pulse (it is generated when a USP train is blocked at the input of the main GARPUN amplifier) happened for significantly longer interelectrode distances as high as l =4.0 cm. For the maximal gaps the discharge is developed along an accidental trajectory, that is no laser guiding is observed (**Fig. 8.1b**). In the case of the combined pulse (when the USP train is amplified regeneratively in the main GARPUN amplifier together with a free-running lasing) the maximal laser-triggered length attained 7.0 cm, the discharge being perfectly guided by the laser beam (**Fig. 8.1c**).

The discharge delay for shorter interelectrode distances (l =2 cm) is less than tens nanoseconds for both smooth and combined laser pulses (**Fig. 8.2a**). For longer distances it increased up to 5 μs. It is found in these experiments that breakdown characteristics do not depend on the HV polarity. Laser-guided DC voltage discharge at analogous experimental conditions has been investigated with the use of self-guided femtosecond IR USP in Ref. [91] and in Ref. [92] at longer (~10 cm) discharge gap. Evidently, the discharge is developing here as a result of the avalanche-like growth of electron density, starting from photo-electrons produced by UV laser radiation. Induced in this way conductivity of the plasma channel created between the electrodes by the combined laser pulse, became sufficient to sustain the discharge current and sufficient for the development of spark: Joule heating resulted in the reduction of the neutral gas density N_0 and hence in the enhancement of the reduced electric field E/N_0 [91].

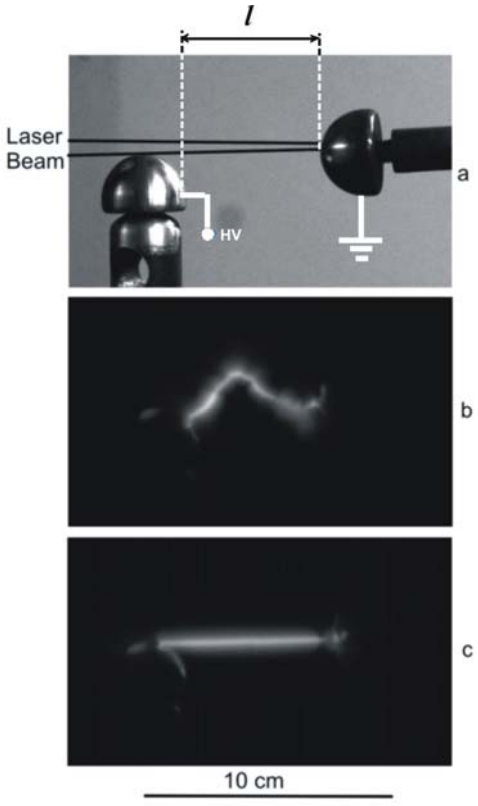

Figure 8.1. View of (**a**) the inter-electrode gap and triggered HV discharges in cases (**b**) l=4.0 cm and smooth laser pulse, (**c**) l=7.0 cm and combined (modulated) laser pulse.

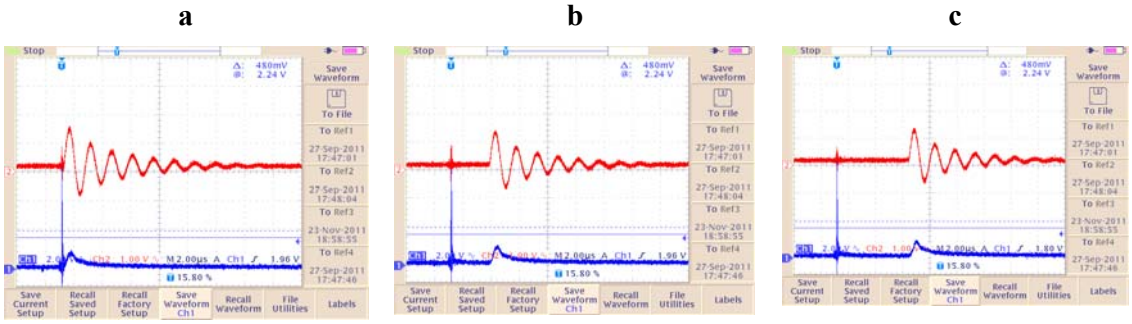

Figure 8.2. Oscilloscope traces of the discharge current (upper traces), laser pulse and plasma luminescence (bottom traces) for various interelectrode gaps l = (**a**) 2; (**b**) 6; and (**c**) 7 cm. Time scale is 2μs/div.

The above results confirm the basic idea of HV discharge triggering and guiding in the experiments with a limited voltage. There has been demonstrated lowering of HV breakdown threshold and perfect discharge guiding.

8.2. Application of the plasma channels created by combined (subpicosecond and 100-ns) UV laser pulses for controlling long-distance HV discharge

The aim is to compare smooth and amplitude-modulated 100-ns pulses of UV laser radiation for triggering and guiding a long HV discharge in atmospheric air. The following experimental improvements are introduced: (i) a double capacity scheme with opposite polarity of electrodes is used (**Fig. 8.3**) which allows us to double a steady voltage at the discharge gap up to ΔU=2U=140 kV; (ii) pulsed 7-stage HV Marx generator is designed and tested with output peak voltage up to 500 kV synchronized with the laser (**Fig. 8.4**); when being applied to a spherical electrode of 15-mm radius placed at 70-cm distance from a plane grounded electrode, it allowed us to investigate breakdown with different delays of a HV pulse relative to the laser pulse. UV radiation is focused by F = 8 m spherical mirror between electrodes. The discharge current is measured by means of Rogovski coils, and HV pulse is monitored by a resistive low-inductance load surrounded by the second Rogovski coil. Breakdown delay time relative to the laser pulse is found in a comparison of discharge current and voltage oscilloscope traces with photodetector signals (see below in **Fig. 8.5**). The discharge images are obtained with CCD camera "Videoscan-285" with time integration over 100 ms.

In experiments with a steady voltage the interelectrode distance l=8.0 cm is set fixed while values of applied voltage are varied from air self breakdown to a threshold for laser triggering. Self-breakdown voltage being something occasional in the range ΔU_{br} = 80÷100 kV corresponded to mean electric field strength in the gap $E_{br} = \Delta U_{br}/l$ = 10÷12.5 kV/cm. It is less then in previous experiments probably because of field nonuniformity for larger ratio of the distance l to electrodes radii and higher humidity of laboratory air in summer. Both modulated and smooth laser pulses of the same energy ~6 J are compared demonstrating great difference in laser triggering voltage, discharge guiding and time delays between the laser pulse and HV breakdown. For modulated pulse triggering threshold (lowest voltage when discharge is still developed) is ΔU_{trig} = 28 kV which is 3 times less than ΔU_{br}. While being triggered the discharge is obligatory guided along the laser beam (**Fig. 8.3**). Time delay is no more than 10 μs at the threshold ΔU_{trig} and less than 0.3 μs for high ΔU. These corresponds to the leader velocity 35-fold growth from ~0.8×10^6 to 2.7×10^7 cm/s which implies that the leader-streamer mechanism becomes dominating. For a smooth pulse and the same interelectrode gap l = 8.0

cm triggering happened at significantly higher voltage $\Delta U_{trig} \approx 60$ kV, no laser guiding is observed at all, and time delays are as large as 400÷500 μs.

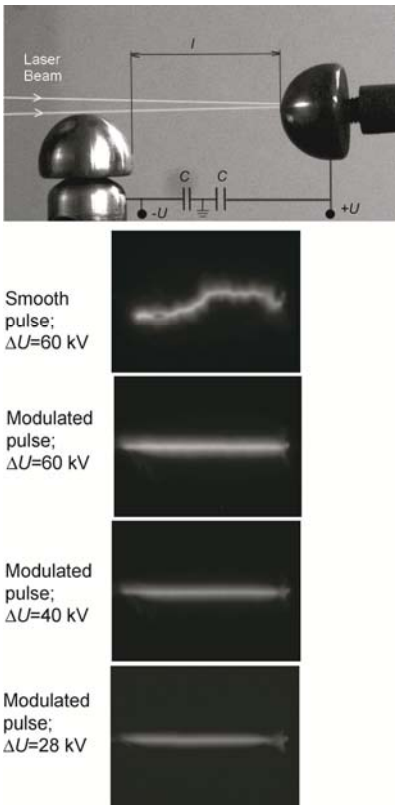

Figure 8.3. A view of the interelectrode gap (above) and laser-triggered HV discharge for smooth and modulated laser pulses at different applied voltages. Interelectrode distance l = 8.0 cm.

A layout of pulsed HV test bench for long-distance discharge studies is shown in **Fig. 8.4**. The experiments are performed in small sphere – plane electrode configuration. Focused laser beam of 6.3-J energy is turned up to vertical direction by the mirror and passed into the discharge gap through the hole of 38-mm diameter in the grounded electrode. HV pulse of 420-kV amplitude is applied to the spherical electrode with a variable delay τ relative to the laser pulse **(Fig. 8.5)**. The HV breakdown time τ_{br} is registered in oscilloscope traces by rapidly increasing discharge current and simultaneous drop down of the voltage signal. Note that a small pedestal in current signals before the breakdown (or even if the breakdown is not developed at all) is really caused by Marx charge leakage through its internal resistors and 2-kΩ load.

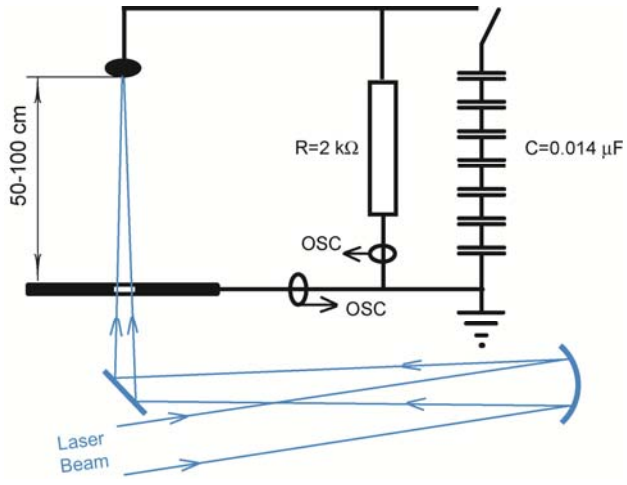

Figure 8.4. Layout of 7-stage Marx generator and experiments on laser triggering of long HV discharges.

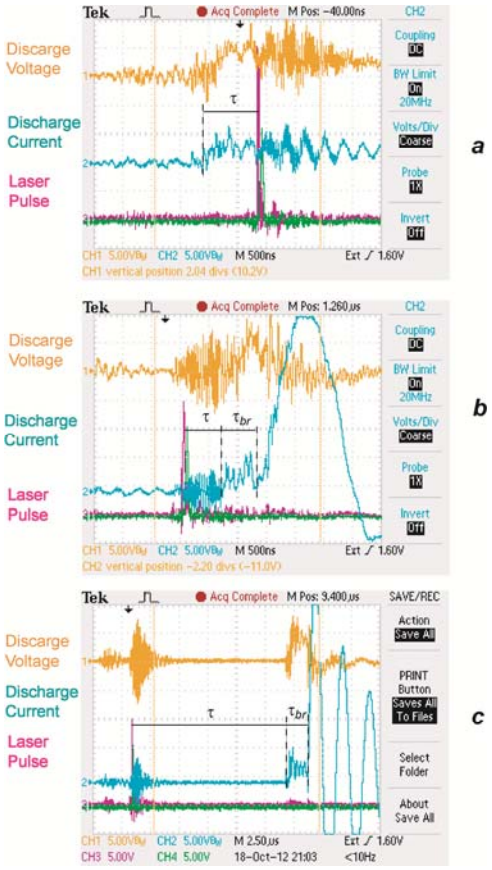

Figure 8.5. Typical oscilloscope traces of Marx generator voltage (upper traces), discharge current (middle traces) and modulated laser pulse (bottom traces) for various delays τ : -0.93 μs (***a***), 0.77 μs (***b***) and 13.7 μs (***c***).

For amplitude-modulated laser pulse the dependence of HV breakdown delay time τ_{br} of the interelectrode distance $l \approx 70$ cm on delay time of the applied 420-kV voltage τ is shown in **Fig. 8.6.** The minimal breakdown delay $\tau_{br} \approx 0.6$ μs corresponds to $\tau \approx 0.8$ μs. It increased up to $\tau_{br} = 3.7$ μs for $\tau = 18$ μs. Thus, the corresponding leader velocity decreased from ~1.2×10^8 cm/s down to ~2×10^7cm/s with an increase in HV pulse delay. If the HV pulse passed ahead of the laser pulse more than ~1 μs (corresponding to negative values of τ in the graph) the breakdown is not developed. For the smooth pulse no breakdown is observed at the same experimental conditions even for the optimal delay time $\tau = 0.8$ μs.

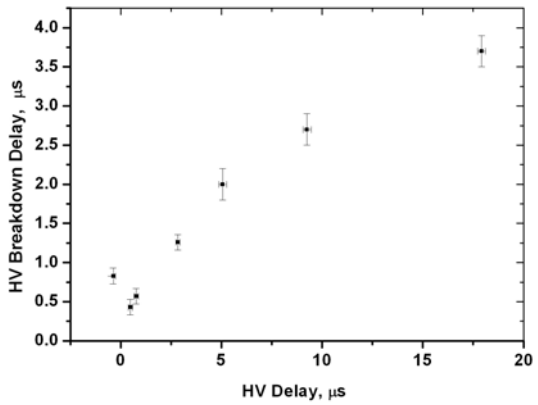

Figure 8.6. HV breakdown delay of the 70-cm interelectrode distance triggered by modulated laser pulse vs. the delay time of applied voltage of 420-kV amplitude.

The CCD images in **Fig. 8.7** demonstrate well guiding of the discharge by amplitude-modulated laser radiation for different time delays of the applied HV pulse**.** A slightly crankshaft-like form of the discharge is appeared in the time-integrated images, which apparently points to a step-wise development of the discharge leader.

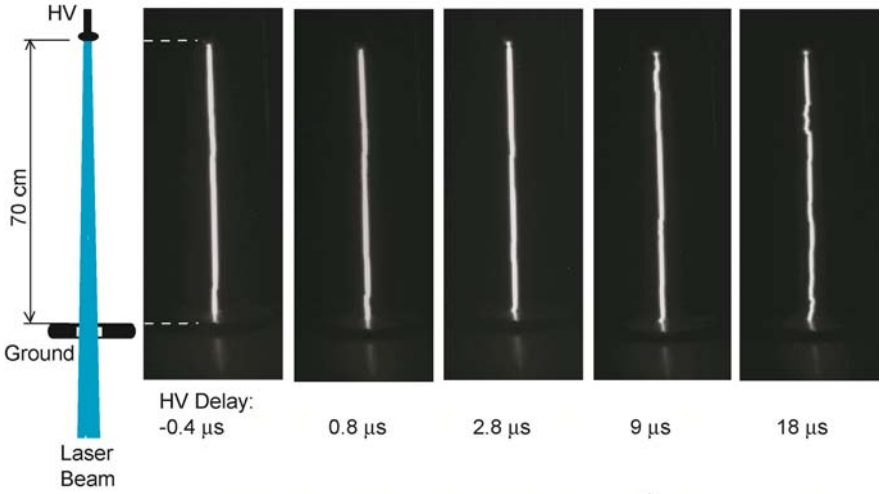

Figure 8.7. CCD images of the HV discharge for various delays of the applied voltage.

The above results are in a reasonable agreement with the model of leader [93], according to which the discharge is developing in the following way. The diffused corona (a bush of streamers) via avalanche ionization in enhanced electric field provides the total current sufficient to sustain the leader, which high-conductivity plasma channel (a stem) creates connection to the high-voltage electrode. Ohmic heating in the leader-corona transition region (a leader tip) leads to the increase of gas temperature, hydrodynamic expansion, and, hence, decrease of gas density. As a result, the rate of electron's detachment of O_2^- ions (formed due to electron attachment to oxygen molecules) significantly increases, which provides an advancement of the leader. The coupled propagation of the leader and its streamer corona lasts until the streamers will reach the ground electrode (the final jump). The leader velocity

$$V_l = I_l / Q_l \tag{8.1}$$

is related to the current I_l entering the leader at its tip. The linear charge Q_l , which is needed for the leader advancement, is estimated under assumption of complete conversion of ohmic energy loss into the gas temperature as [93]

$$Q_l = \frac{7}{2} f^{-1} \frac{N_0 S}{E_{eff} L} k_B \left(T_c - T_0\right) \tag{8.2}$$

where N_0 is the air density, S and L are the effective cross section and the length of the transition region near the leader tip, E_{eff} is the strength of the effective net electric field in the transition region. The characteristic coefficient f, in fact, is the fraction of electric field's work, which is transferred into neutral gas heating, T_0 and T_c are the temperature of the ambient air and the critical temperature of neutral gas molecules inside the transition region, at which the leader advancement is sustained, respectively.

In Refs. [94, 95], the following qualitative explanation of the leader speed enhancement for laser-guided discharge was proposed. In the case of self-breakdown, in the absence of laser field pre-ionization, the critical temperature is of the order T_c~1500^{0}C, at which almost complete collisional detachment of electrons of O_2^- ions in transition region occurs and provides sufficient for leader advancement conductivity. Under conditions of laser-guided discharge, the average density of negative ions is much higher than that for the self-breakdown, and to provide necessary conductivity one needs to detach only a small part of electrons, for which a smaller temperature is sufficient. As a result, the leader velocity increases as $V_l \propto 1/(T_c - T_0)$.

The main conclusions of the current experiments are as follows: (i) once again we confirmed the finding of our previous experiments that amplitude-modulated UV radiation is very effective tool for triggering and guiding of the HV discharge; (ii) long-time delays of tens or even hundred microseconds being observed in steady-voltage and delayed pulsed voltage experiments exceed by many orders of magnitude the lifetime of free electrons in laser-produced plasma channel; (iii) a step-wise propagation of the discharge leader is predicted from time-integrated images. Based on the obtained results the probable mechanism of low-threshold long-distance air breakdown and guiding along a laser beam can be proposed. Electrons produced by UV radiation via direct MPI or REMPI, as well as in revival of bound electrons in O_2^- ions via photodetachment (these processes are proven to be significantly more efficient for combined amplitude-modulated radiation) after termination of the laser pulse are finally captured by O_2 molecules. Afterwards O_2^- negative ions having very low binding energy of ~0.5 eV are easily ionized in the applied electric field, like they are a low ionization potential additive to the gas. Avalanche ionization in enhanced electric field of streamer corona, as well as electron collisional detachment in the leader tip both depend on the O_2^- ions density, i.e. initial density of laser-produced photoelectrons. Such discharge is able to occur for the time as long as ~1 ms until O_2^- ions recombine with positive O_4^+ ions. In present experiments with a delayed HV pulse, the maximal breakdown delay of 3.7 μs is determined by a decrease of the HV pulse-form.

8.3. Development and spatial structure of the laser-guided HV discharge

Evolution of long-distance pulsed HV discharge triggered by a single USP of Ti:Sapphire laser (λ~800 nm) was studied by time framing or streak camera techniques in a number of papers (see, e.g., Refs. [94–98]). Positive and negative leader formation and their propagation with a velocity as high as (2.4±0.5)×10^6 m/s was observed for applied voltage of 2.2 MV. Velocity of the positive leader initiated and supported by filaments is much higher than in a self-breakdown discharge. Such positive leader velocity determined a laser guided discharge length up to 2.4 m (of the total overlapped discharge gap length of 4.5 m) if one supposes a laser plasma channel lifetime to be ~1 μs. It should be noted that up to now there have not been experiments on HV discharge dynamics carried out with USP trains, even though they are able to prolong plasma channel lifetime. UV laser pulses, which are of especial interest for efficient air ionization have not been also studied with exception of paper [99] where 35-ps pulse at fourth harmonic of Nd:YAG laser (λ =266 nm) was used.

In the present study of temporal evolution of a long pulsed laser-induced HV discharge we used the HV test-bench described in Subsection 8.2. A single UV USP is generated by a frequency-tripled Ti:Sapphire front-end. After passing a ring-like mirror scheme, it is multiplied into a train with a time interval $\Delta t \approx 3$ ns between individual pulses. This train is successively amplified for four passes through Berdysh KrF laser preamplifier and for two

passes through the main KrF laser amplifier GARPUN (see Subsection 2.4). Total output energy in the train consisting of about 10 pulses reached 3 J after amplification being superimposed with the 1.3-J ASE (**Fig. 8.8**).

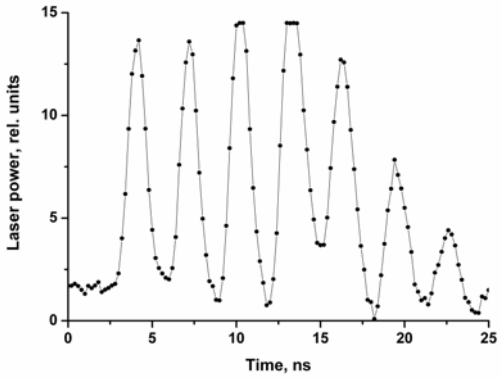

Figure 8.8. Oscilloscope trace of the USP train integrated because of oscilloscope response time.

A layout of the interelectrode gap can be seen in a static streak camera image (without sweeping) (**Fig. 8.9).** Schematically it is shown at the top of **Figs. 8.10, 8.11**. Laser beam is focused by a spherical mirror with the focal length F=8 m and directed by a plane turning mirror into the discharge gap through a 18-mm hole in a plane grounded disc 70 cm in diameter (**1** in **Fig. 8.9**), on which surface a semispherical electrode of 37-mm radius (**2**) is situated. Linear focus of the laser beam is situated near HV semispherical electrode of 15-mm radius (**3**). Filamentation of this beam provided air ionization and plasma channel along the whole interelectrode length (see Sec. 7). A distance between electrodes is varied in the range of l =25÷50 cm. A positive peak voltage of 390-kV is applied to the HV electrode from a 7-stage Marx pulsed voltage generator (PVG).

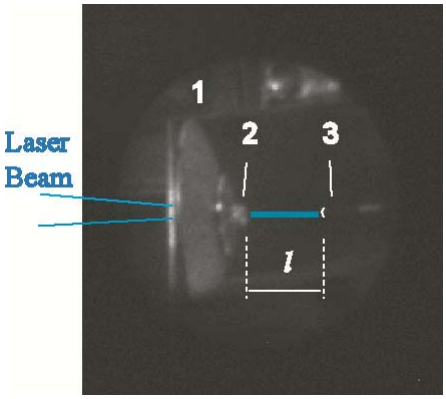

Figure 8.9. Static image of the discharge gap obtained with the streak camera without sweeping.

The discharge current is measured with a Rogowski coil and the PVG voltage is measured with another Rogowski coil, which encircled a low-inductance load with a resistance of 2 kOhm connected in parallel with the discharge gap. The instant of gap breakdown is recorded on waveforms as an abrupt rise in the current signal and a simultaneous voltage drop. The

discharge is imaged with a streak camera "Agat" that had a sweeping speed ~20 ns/cm. A streak image from the screen is recordered by the Videoscan-285 CCD camera with an acquisition interval of 100 ms. Laser guiding of the discharge is permanently controlled during these experiments. For limited registration time of the streak camera (~50 ns) a very low jitter of the HV breakdown is allowed. It is attained by decreasing the discharge gap down to l = 25 cm and by increasing average electric field strength up to 15 kV/cm, respectively. Note that guided discharge is observed also for longer interelectrode distances, but it takes more time for breakdown evolution, and, consequently, jitter goes out of the registration time.

Typical streak camera images of an initial stage of the discharge are shown in **Figs. 8.10, 8.11**. These images are rather difficult to register. Because the main electric energy stored in the PVG capacitor, even though coupled to the discharge in the later time, is accompanied by so intensive light emission that the latter provided parasitic flash exposure of the streak camera screen, and this fact significantly reduced a contrast of the images. For example, one can see a bright luminescence of the screen in the form of semi-circle at the very beginning of sweeping and somehow less intensive circle (actually, it is an image of the streak camera photocathode) in the center. Nevertheless, all together these images allowed us to identify the general features of the discharge evolution described in literature [8, 9, 100, 101]. **Figure 8.10** corresponds to a longer gap l = 50 cm, when no discharge took place, while in **Fig. 8.11** one can see different discharge features at the early stage for l = 25 cm.

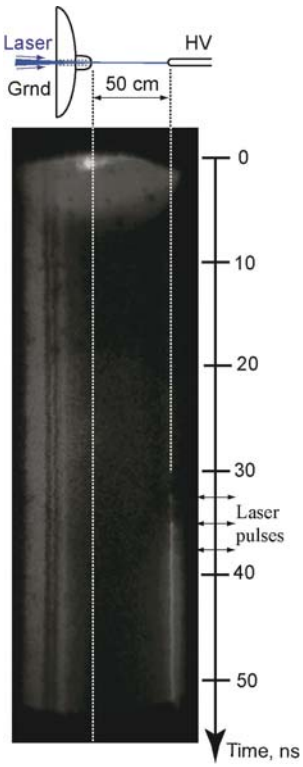

Figure 8.10. Streak camera image for early stage of HV discharge with interelectrode distance l = 50 cm. There is no electric discharge. Radiation of erosion plasma plumes near the anode can be seen in the lower right corner below "laser pulses" on the time scale.

Thus, in **Figs. 8.10, 8.11** a consequence of erosion plasma plumes formed on the HV electrode by the USP laser train can be seen. By the way, it made possible a precise calibration of the streak camera sweeping speed. Radiation of erosion plasma plumes near the anode is observed for a long time in all images. For shorter interelectrode gap l = 25 cm in **Fig. 8.11*a*** the breakdown process already begins before the laser pulse train, and expanding slightly luminous region (its front is marked by a dashed white line) adjacent to the anode might be interpreted like a positive leader tip propagating towards the grounded electrode with approximately constant velocity of $v_L = 1.2\times10^6$ m/s. In the next image (***b***) this leader moves with higher

velocity of $v_L = 4.0\times10^6$ m/s, apparently because of preliminary air ionization by laser radiation that has came into the gap before HV pulse. Before the final jump, when the leader head is approaching to the grounded electrode, it accelerates up to 3.2×10^7 m/s. To our knowledge, these are the highest velocities compared with previous experiments with a single UV [99] or Ti:Sapphire USP [94–98]. At the final jump starting with some short delay after the moment when the streamer corona reaches the grounded electrode a return stroke of the discharge arises (***a-c***), which is a wave where the HV electric field potential drops to zero while a discharge current (and therefore plasma luminosity) rapidly rises. The return stroke propagates with very high initial phase velocity of $v_{RS} = 6.7\times10^7$ m/s, which is of the order of the light velocity. When approaching to the HV electrode, the return stroke wave gradually decelerates.

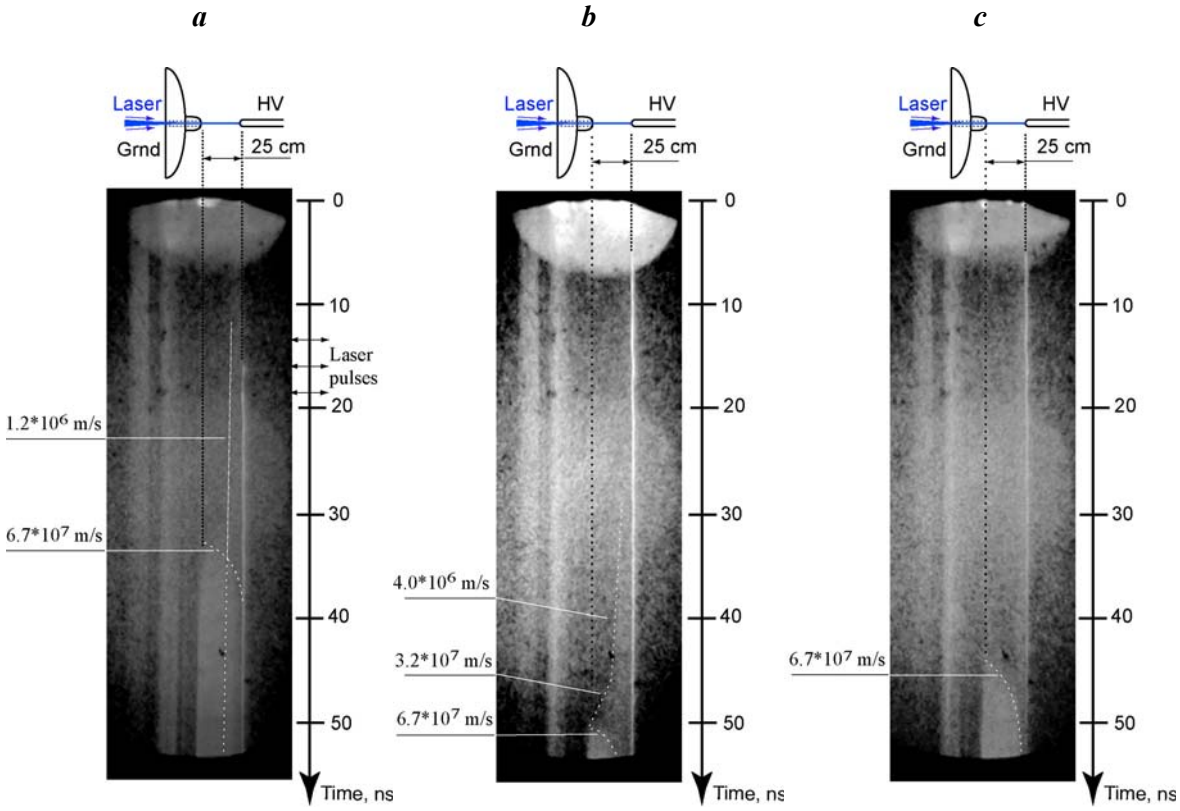

Figure 8.11. Streak camera images for early stages of HV discharge with interelectrode distance $l = 25$ cm. USP train is after (a) and before (b,c) the beginning of HV pulse.

Unfortunately, some mentioned above features are not seen so clear in the other streak images because of parasitic flash exposure of the steak camera. Nevertheless, it is expected that they have a general character for such kind of laser-guided long-distance HV discharges, when initial air ionization is produced by laser radiation. Note, that the highest velocities of a positive leader $v_L \sim10^7$ m/s and of a return stroke $v_{RS} = 1.3\times10^7$ m/s were measured in laboratory experiments for a self-breakdown regime (without laser illumination) of 6-m length spark at 2-MV voltage [102]. In our experiments, typical discharge triggering delay time was no more than 50 ns, which was less than the characteristic electron attachment time in DC electric field with the strength higher than 6kV/cm [30] (see also Subsection 5.7). As a result, the USP train produced enough number of electrons for the leader to propagate along the laser-produced plasma channel, and there was no need for additional avalanche ionization to create conductivity sufficient for the discharge development, and thus the leader discharge developed in a different regime rather than that formulated in the model [93].

9. Conclusions

1. Different operation regimes of the hybrid Ti:Sapphire / KrF laser facility GARPUN-MTW are realized to generate the variety of UV pulses intended for atmospheric air ionization:
   - a single USP of ~ 0.6 J energy, ≤ 1 ps pulse duration, and ~ 1 TW peak power;
   - a USP train (up to 10 pulses) with ~ 2 J total energy, ~ 1 ps pulse duration, ~ 0.1÷0.2 TW peak power, and ≥ 2 ns time interval between the pulses;
   - an amplitude-modulated pulse combined of the USP train and 100-ns pulse of quasi-steady lasing with ≤ 30 J total energy and 0.1÷0.2 TW peak power of individual USP.
2. The USP parameters are controlled including:
   - a correction of phase aberrations after KrF amplifier chain by means of an adaptive mirror to improve laser beam divergence;
   - an introduction of an initial negative frequency chirp to compensate a group velocity dispersion in the KrF amplifier windows and extended air track;
   - designing and implementation of pulse multiplexers and various amplification layouts to produce a short train of UV USPs for successive amplification in large-aperture e-beam-pumped KrF amplifiers.
3. Filamentation of the USP UV laser beam in atmospheric air is investigated:
   - filamentation of focused femtosecond UV USP and plasma channel formation governed by variable wavefront distortions is experimentally and numerically studied in comparison with the IR USP; a twofold increase in the plasma channels length is demonstrated when a spherical aberration has been introduced into the initial transverse spatial distribution of the USP;
   - focusing capabilities of multiply-filamented supercritical (P/P_{cr}~3000) subTW-level UV laser beam of both a single USP and USP train are studied along 100-m-long laboratory track and linear focusing behavior is demonstrated for numerical apertures of all-mirror focusing system in the range NA=1.5·10^{-2} − 1.5·10^{-3}, being favorable for a spatial matching of the USP and long-lasting radiation in combined amplitude-modulated pulse.
4. Air ionization and plasma relaxation under irradiation with UV nanosecond and femtosecond pulses are investigated using two different laser sources, both operating at wavelength λ = 248 nm, namely, a discharge-pumped KrF laser with output energy up to 200 mJ and variable pulse duration 4÷25 ns, and frequency-tripled Ti:Sapphire laser system with output energy up to 0.4 mJ and pulse width of ~ 100 fs:
   - (2 + 1) Resonance Enhanced Multi-Photon Ionization (REMPI) of oxygen molecules via an intermediate excited state is shown to be the main process of air ionization by nanosecond pulses with intensity ≥ 3×10^8 W/cm^2, while (3 + 1) REMPI of nitrogen is less probable; for femtosecond pulses direct Multi-Photon Ionization (MPI) of oxygen seems to be the main process;
   - plasma density in the channel formed by the second USP of a tandem IR pulse in the process of filamentation is slightly less than the density formed by the first USP for time delay from 1.5 to 15 ns; in the case of a tandem UV pulse, for delays longer than 5 ns the electron density for the second USP does not differ from that for the first USP, whereas at shorter delays it falls down threefold which can be ascribed to absorption of the second USP in plasma channel produced by the first one;
   - by analysing electron density dynamics in the air plasma we have shown that at plasma densities ≥ 10^{14}÷10^{15} cm^{-3} recombination of photoelectrons with parent positive ions O_2^+ dominates and results in an irreversible loss of electrons, whereas for lower densities electrons are captured by O_2 molecules and can be easily detached by UV radiation with relatively low intensity ≥ 10^7 W/cm^2;

- a revival effect of electrons captured in O_2^- ions by the second nanosecond UV pulse is demonstrated and provides a justification of the UV pulse train benefit to increase electron density in laser-produced plasma channels;
- a lifetime of electrons in regard of the three-body attachment process to O_2 molecules is investigated in applied DC electric field both experimentally and theoretically showing a six-fold increase with a field strength varying from 0.2 to 7 kV/cm;
- numerical modeling of temporal behavior of different plasma components in DC electric field demonstrates that negative O_2^- ions exist for several hundred microseconds before their recombination with positive O_4^+ and O_2^+ ions.

5. A comprehensive theoretical study of direct Multi-Photon Ionization (MPI) and Resonance-Enhanced Multi-Photon Ionization (REMPI) is undertaken which allow us:
   - to clarify different regimes of air ionization and to compare them with the obtained experimental data;
   - to investigate the effect of REMPI on filamentation of the UV USP laser beam.
6. Focused amplitude-modulated 100-ns UV laser pulses composed of high-intensity subpicosecond USP train, which effectively ionize air via direct MPI or REMPI and low-intensity long-lasting pedestal, which suppresses electron attachment between the USP pulses are demonstrated to produce plasma density ~ 10^{15} cm^{-3}, which is 100 times higher compared with a smooth pulse.
7. The HV electric discharge laser-guiding experiments are performed for three different configurations, namely, (i) discharge initiation in a short (up to 8 cm) gap with DC voltage supply; (ii) discharge guiding in a long 70-cm gap with a controllable delay of the HV pulse, and (iii) temporal evolution measurements of high-speed laser-guided 25-cm gap breakdown:
   - for a short discharge gap ($l \leq 2$ cm), amplitude-modulated laser pulse initiated HV discharge with a time delay of tens nanoseconds – evidently it is developing due to an avalanche-like growth of electron density, starting from photo-electrons produced by the laser pulse;
   - with increased gap length ($l \sim 8$ cm) breakdown delays of 0.3÷10 μs are measured, which implies that the leader-streamer mechanism becomes dominating with characteristic velocities from 0.8×10^4 to 2.7×10^5 m/s;
   - for a long gap ($l \sim 80$ cm) and 420-kV HV pulse delayed from 0.8 to 18 μs relative to the laser pulse (i.e. much longer than a free electron lifetime), a guided discharge still exists with delays from 0.6 to 3.7 μs, a step-wise leader propagation being observed with corresponding average velocities from ~1.2×10^6 to ~2×10^5 m/s;
   - direct registration with a streak camera of the breakdown space-time structure for $l = 25$ cm gap at 390-kV pulsed voltage reveals the leader propagation with the highest ever measured velocity of up to 3.2×10^7 m/s followed by a reverse stroke moving with velocity 6.7×10^7 m/s, which is near the speed of light; as the USP train produces high enough electron density and typical discharge triggering delay time is less than characteristic electron attachment time, there is no need for additional avalanche ionization to create conductivity sufficient for the discharge development, and thus the leader is supported in a different regime compared with a conventional leader propagation.
8. A qualitative model of laser-guided discharge is proposed – photolectrons produced by UV radiation via direct MPI or REMPI, as well as in revival of bound electrons in O_2^- ions via photodetachment finally form (after termination of the laser pulse) O_2^- negative ions having very low binding energy of ~0.5 eV. Preferable avalanche ionization of these ions in the vicinity of streamer corona, as well as temperature-dependent electron

detachment in the leader tip ensure discharge guiding, which is able to occur for the time as long as ~1 ms until O_2^- ions recombine with positive O_4^+ ions.

10. References

1. Koopman D.V., Wilkenson T.D. *J. Appl. Phy*s., **42**, 1883 (1971).
2. Zvorykin V.D., Nikolaev F.A., Kholin I.V., et al. *Fiz. Plazmy*, **5**, 1140 (1979).
3. Askar'yan G.A. *Sov.Phys. JETP*, **28**, 732 (1968).
4. Chateauneuf M., Payeur S., Dubois J., Kieffer J.-C. *Appl. Phys. Lett.*, **92**, 091104 (2008).
5. Zvorykin V.D., Levchenko A.O., Ustinovskii N.N., Smetanin I.V. *JETP Lett.*, **91**, 226 (2010).
6. Zvorykin V.D., Levchenko A.O., Shutov A.V., et al. *Phys. Plasmas*, **19**, 033509 (2012).
7. Zhao X.M., Diels J.-C., Wang Y.C., Elizondo J. *IEEE J. Quantum Electron*., **31**, 599 (1995).
8. Bazelyan E.M., Raizer Yu.P., "Lightning and lightning protection physics", Philadelphia: IOP Publ., 2000.
9. Bazelyan E.M., Raizer Yu.P. *Phys. Usp*., **43** (7), 701 (2000).
10. Kasparian J., Ackermann R., Andre Y.-B., et al. *Opt. Express*, **16**, 5757 (2008).
11. Zvorykin V.D., Levchenko A.O., Ustinovskii N.N. *Quantum Electron*., **41** (3), 227 (2011).
12. Penano J., Sprangle P., Hafizi B., et al. *J. Appl. Phys*., **111**, 033105 (2012).
13. Couairon A., Berge L. *Phys. Rev. Lett*., **88**, 135003 (2002).
14. Basov N.G., Vadkovskii A.D., Zvorykin V.D., et al. *Quantum. Electron*., **24** (1), 13 (1994).
15. Zvorykin V.D., Didenko N.V., Ionin A.A., et al. *Laser Part. Beams,* **25**, 435 (2007).
16. Zvorykin V.D., Levchenko A.O., Ustinovskii N.N. *Quantum. Electron*., **40** (5), 381 (2010).
17. Zvorykin V.D., Ionin A.A., Levchenko A.O., et al. *J. Phys. Conf. Ser*., **244**, 032014 (2010).
18. Johnson P.M., Otis C.E. *Annu. Rev. Phys. Chem*., **323**, 139 (1981).
19. Zvorykin V.D., Levchenko A.O., Smetanin I.V., Ustinovskii N.N. Patent of the Russian Federation, No. 90620. Priority of 21.09.2009.
20. Zvorykin V.D., Levchenko A.O., Smetanin I.V., Ustinovskii N.N. Patent of the Russian Federation, No. 2406188. Priority of 15.09.2009.
21. Zvorykin V.D., Levchenko A.O., Smetanin I.V., Ustinovskii N.N. Patent of the Russian Federation, No. 2411662. Priority of 31.05.2010.
22. Zvorykin V.D., Levchenko A.O., Smetanin I.V., Ustinovskii N.N. Proc. XIIIth School for Young Scientists "Topical Physical Problems" and IVth Workshop "Innovative Aspects of Basic Research") (Zvenigorod – Moscow, FIAN, 2010) p. 144.
23. Zvorykin V.D., Ionin A.A., Levchenko A.O., et al. Abstracts of the 39th Int. (Zvenigorod) Conf. on Plasma Physics and Controlled Thermonuclear Fusion (Zvenigorod, IOFRAN, 2012) p. 220.
24. Ionin A.A., Kudryashov S.I., Levchenko A.O., et al. *Appl. Phys. Lett*., **100**, 104105 (2012).
25. Ionin A.A., Kudryashov S.V., Levchenko A.O., et al. *AIP Conf. Proc.,* **1464**, 711-720 (2012).
26. Ionin A.A., Kudryashov S.V., Levchenko A.O., et al. *SPIE Newsroom*, (2012) doi: 10.1117/2.1201211.004550.
27. Zvorykin V.D., Ionin A.A., Levchenko A.O., et al. *Nuclear Instruments and Methods in Physics Research B*, **309**, 218 (2013).

28. Zvorykin V.D., Ionin A.A., Levchenko A.O., et al. *Quantum. Electron*., **43** (4), 332 (2013).
29. Zvorykin V.D., Ionin A.A., Levchenko A.O., et al. *Quantum. Electron*., **43** (4), 339 (2013).
30. Shutov A.V., Smetanin I.V., Ionin A.A., et al. *Appl. Phys. Lett.,* **103**, 034106 (2013).
31. Geints Y.E., Zemlyanov A.A., Izyumov N.A., et al. *JETP*, **116** (2), 197 (2013)
32. Ionin A.A., Kudryashov S.I., Mokrousova D.V. et al. *Laser Physics Letters*, **11** (1), 016001 (2014).
33. Ionin A.A., Iroshnikov N.G., Kosareva O. et al. *JOSA B*, **30** (8), 2257 (2013).
34. Geints Yu.E., Zemlyanov A.A., Ionin A.A., et al. *Quantum. Electron*., **42** (4), 319 (2012).
35. Dergachev A.A., Ionin A.A., Kandidov et al. *Quantum. Electron*., **43** (1), 29 (2013).
36. Zvorykin V.D., Lebo I.G., Rozanov V.B. *Bull. of Lebedev Phys. Inst.*, No. 9-10, 20 (1997).
37. Berge L., Skupin S., Nuter R., et al. *Rep. Progress in Phys.*, **70**, 1633 (2007).
38. Couairon A., Mysyrowicz A. *Phys.Rep*., **441**, 47 (2007).
39. Chin S.L. *Femtosecond Laser Filamentation,* Springer, N.Y., 2010.
40. Zhou B., Akturk S., Prade B., et al. *Opt. Express*, **17**, 11450 (2009).
41. Polynkin P. and Moloney J.V. *Appl. Phys. Lett*., **99**, 151103 (2011).
42. Shneider M.N., Zheltikov A.M., and Miles R.B. *Phys Plasmas*, **18**, 063509 (2011).
43. Liu W., Chin S.L. *Opt. Express* **13**, 5750 (2005).
44. Perelomov A.M., Popov V.S., Terent'ev M.V. *Sov. Phys. JETP* **23**, 1393 (1966).
45. Huxley L.G.H. and Crompton R.W. *The Diffusion and Drift of Electrons in Gases*, John Wiley & Sons, 1974.
46. Raizer Yu.P. *Gas Discharge Physics*, Springer Verlag, 1997.
47. Losev L.L., Soskov V.I. *Quantum Electron*., **19**, 46 (1989).
48. Losev L.L., Soskov V.I. *Atmospheric and Oceanic Optics*, **3**, 772 (1990).
49. Aota T., Takahashi E., Losev L.L., et al. *Japanese J. of Appl. Phys*., **44**, 3313 (2005).
50. Guthrie J.A., Wang X.X., Radziemski L.J. *Chem. Phys. Lett*., **170**, 117 (1990).
51. Bominaar J., Shoemaecker C., Dam N., et al. *Chem. Phys. Lett*., **435**, 242 (2007).
52. Ogorzalek Loo R., Marinelli W.J., Houston P.L., et al., *J. Chem. Phys*., **91,** 5185 (1989).
53. Stupitskii E.L. *High Temperature*, **44**, 172 (2006).
54. Kossyi I.A., Kostinsky A.Yu., Matveev A.A., Silakov V.P. *Plasma Sources Sci. Technol.,* **1**, 207 (1992).
55. Schwarz J., Rambo P., and Diels J.C. *Appl. Phys. B* **72**, 343 (2001).
56. Khan N., Mariun N., Aris I., and Yeak J. *New Journal of Physics* **4**, 61.1 (2002).
57. Burch D.S., Smith S.J., Branscomb L.M. *Phys. Rev*., **112**, 171 (1958).
58. Dinu L., Groenenboom G.C., van der Zande W.J. *J. Chem Phys.*, **119**, 8864 (2003).
59. Hodges R.V., Lee L.C., Moseley J.T. *J. Chem Phys.*, **75**, 2998 (1980).
60. Ling P., Lucchese R.R. *J. Chem Phys.*, **114**, 9350 (2001).
61. Méjean G., Ackermann R., Kasparian J., et al. *Appl. Phys. Lett*., **88**, 021101 (2006).
62. Physics and chemistry of gas discharges in microwave beams (Proc. IOFAN, v. 47), Moscow, Nauka, 1994.
63. Bloch F. *Phys. Rev*., **48**, 689 (1935).
64. Longmire C.L. *Phys. Fluids*, **27**, 2694 (1984).
65. Ladouceur H.D., Baronavski A.P. et.al. *Optics Communications*, **189**, 107 (2001).
66. Chanin L.M., Phelps A.V., Biondi M.A. *Phys. Rev.*, **128**, 219 (1962).
67. Spence D., Schulz G.J. *Phys.Rev. A*. **5**, 2 (1972).
68. Phelps A.V. Defense Nuclear Agency Reaction Rate Handbook (M.H. Bortner, T. Baurer Eds), Chapter 17, 1972.
69. Alexandrov N.L. *Sov. Phys. Uspekhi*, **31**, 101 (1988).

70. Belenov E.M., Isakov V.A., Nazarkin A.V., and Smetanin I.V. *J. Sov. Laser Research*, **13**, 118 (1992).
71. McDaniel E.W. Collision phenomena in ionized gases, J. Wiley & Sons, Inc., 1964.
72. Gordeyev O.A., Kalinin A.P., Komov A.L., et al. *Reviews on the Thermophysical properties of Substances*, Institute of High Temperatures of the Russian Ac. Sci., Moscow (1985), Vol. 5, iss.55.
73. Engelhardt A.G., Phelps A.V., Risk C.G. *Phys Rev.*, **135**, A1566 (1964).
74. Itikawa Y. and Mason N. *J. Phys. Chem. Ref. Data*, **34**, 1 (2005).
75. Islamov R.S., Kochetov I.V., Pevgov V.G. *P.N. Lebedev Physical Inst. Preprint* No. 169, Moscow, 1977.
76. Phelps A.V. (unpublished) ftp://jila.colorado.edu/collision data/.
77. Keldysh L.V. *ZhETF*, **47**, 1945 (1964)
78. Katsumata S., Kimura K. *Applied spectroscopy Reviews*, **27**, 193 (1992).
79. Bischel W.K., Perry B.E. and Crosley D.R. *Chem. Phys. Lett*., **82**, 85 (1981).
80. Alden M. and Wendt W. *Opt. Comm.*, **69**, 31 (1988).
81. Hanisco T.F. and Kummel A.C. *J. Phys. Chem*., **95**, 8565 (1991).
82. Lykke K.R. and Kay B.D. *J. Chem. Phys*., **95**, 2252 (1991).
83. Clark A., Kosmidis C., Dies R.M. et al., *J. Phys. D : Appl. Phys*., **26**, 2107 (1993).
84. Laufer G., Lee A.S. and Chelliah H.K. *Appl. Opt*., **36**, 3278 (1997).
85. Way J., Hummelt J., and Scharer J. *J. Appl. Phys*., **106**, 083303 (2009).
86. Belenov E.M., Kryukov P.G., Nazarkin A.V., Smetanin I.V. *Quantum Electron*., **22,** 1113 (1992).
87. Yokelson R.J., Lipert R.J., and Chupka W.A. *J. Phys. Chem*., **97**, 6153 (1992).
88. Poluektov I.A., Nazarkin A.V. *Sov. J. Quantum Electron*., **11**, 159 (1981).
89. Dixit S.N. and McKoy V. *J. Chem. Phys*., **82**, 3546 (1985).
90. Akhmanov S.A., Sukhorukov A.P., and Khokhlov R.V. *Sov. Phys. Usp.* **10,** 609 (1968).
91. Tsortzakis S., Prade B., Franco M., et al., *Phys. Rev. E*, **64**, 057401 (2001).
92. Gordon D.F., Ting A., Hubbard R.F., et al., *Phys. Plasmas*, **10**, 4530 (2003).
93. Gallimberti I., Bacchiega G., Bondiou-Clergerie A., Lalande P*., C. R. Physique*, **3**, 1335 (2002).
94. Pepin H., Comtois D., Vidal F. et al. *Phys. Plasmas*, **8**, 2532 (2001).
95. Comtois D., Pepin H., Vidal F. et al. *IEEE Trans. Plasma Sci.*, **31**, 377 (2003).
96. Comtois D., Chien C.Y., Desparois A. et al. *Appl. Phys. Lett*., **76**, 819 (2000).
97. Ackermann B., Mechain G., Mejean G. et al. *Appl. Phys. B*, **82**, 561 (2006).
98. Fujii T., Miki M., Goto N., et al. *Phys. Plasmas*, **15**, 013107 (2008).
99. Antipov A.A., Grasyuk A.Z., Zhigalkyn A.K., et al. *Sov. Phys. Tech. Phys.*, **36**, 490 (1991).
100. Uman M.A., "The Lightning Discharge", Dover Publications, 2001.
101. Rakov V. and Uman M., "Lightning: physics and effects", Cambridge University Press, 2003.
102. Sherbakov Y.V., Lebedev V.B., Rakov V.A., 2008 Annual Report Conference on Electrical Insulation Dielectric Phenomena, p. 633, IEEE 2008.

Attachment 1: List of published papers and reports with abstracts

1. A.A. Ionin, S.I. Kudryashov, A.O. Levchenko, L.V. Seleznev, A.V. Shutov, D.V. Sinitsyn, I.V. Smetanin, N.N. Ustinovsky, V.D. Zvorykin, "Triggering and guiding electric discharge by a train of UV picosecond pulses combined with a long UV pulse", *Appl. Phys. Lett.*, **100**, 104105 (2012).
*Abstract.*Non-self-sustained electric discharge and electric breakdown were triggered and guided by a train of picosecond ultraviolet (UV) pulses overlapped with a long free-running UV pulse of a hybrid Ti:Sapphire-KrF laser facility. Photocurrent sustained by this train is two orders of magnitude higher, and electric breakdown distance is twice longer than those for the discharge triggered by the long UV pulse only.

2. Ionin A.A., Kudryashov S.V., Levchenko A.O., et al. *SPIE Newsroom*, (2012) doi: 10.1117/2.1201211.004550.
Abstract. Non-self-sustained electric discharge and electric breakdown were triggered and guided by a train of picosecond pulses overlapped with a long free-running pulse at the same frequency.

3. A.A. Ionin, S.I. Kudryashov, A.O. Levchenko, L.V. Seleznev, A.V. Shutov, D.V. Sinitsyn, I.V. Smetanin, N.N. Ustinovsky, and V.D. Zvorykin, "Triggering and guiding electric discharge by a train of ultrashort UV pulses", *AIP Conf. Proc.,* **1464**, 711-720 (2012).
Abstract. Non-self-sustained electric discharge and electric breakdown were triggered and guided by a train of ultrashort sub-TW ultraviolet (UV) pulses overlapped with a long free-running UV pulse of a hybrid Ti:Sapphire - KrF laser facility. Photocurrent sustained by this train is two orders of magnitude higher, and electric breakdown distance is twice longer than those for the discharge triggered by the long UV pulse only. When transporting the laser radiation over the long distance, UV filaments of ~ 100 m length were observed.

4. Yu E Geints, A A Zemlyanov, A A Ionin, S I Kudryashov, L V Seleznev, D V Sinitsyn, E S Sunchugasheva, "Nonlinear propagation of a high-power focused femtosecond laser pulse in air under atmospheric and reduced pressure", *Quantum. Electron*., 2012, **42** (4), 319–326
*Abstract.*This paper examines the propagation of focused femtosecond gigawatt laser pulses in air under normal and reduced pressure in the case of Kerr self-focusing and photoionization of the medium. The influence of gas density on the beam dimensions and power and the electron density in the plasma column in the nonlinear focus zone of the laser beam has been studied experimentally and by numerical simulation. It has been shown that, in rarefied air, the radiation-induced reduction in the rate of plasma formation diminishes the blocking effect of the plasma on the growth of the beam intensity in the case of tight focusing. This allows higher power densities of ultrashort laser pulses to be reached in the focal waist region in comparison with beam self-focusing under atmospheric pressure.

5. A.A. Ionin, S.I. Kudryashov, A.O. Levchenko, L.V. Seleznev, A.V. Shutov, D.V. Sinitsyn, I.V. Smetanin, N.N. Ustinovsky, and V.D. Zvorykin, "Triggering and guiding electric discharge by a train of ultrashort UV pulses and a long UV pulse emitted by a hybrid Ti:Sapphire – KrF laser facility" *Proc. of SPIE,* 8547, 85470G (2012).
*Abstract.*Non-self-sustained electric discharge and electric breakdown were triggered and guided by a train of ultrashort sub-TW ultraviolet (UV) pulses overlapped with a long free-running UV pulse of a hybrid Ti:Sapphire - KrF laser facility. Photocurrent sustained by this train is two orders of magnitude higher, and electric breakdown distance is twice longer than

those for the discharge triggered by the long UV pulse only. When transporting the laser radiation over the long distance, UV filaments of ~ 100 m length were observed.

6. V.D. Zvorykin, A.A. Ionin, A.O. Levchenko, L.V. Seleznev, A.V. Shutov, D.V. Sinitsyn, I.V. Smetanin, N.N. Ustinovskii, "Effects of picosecond terawatt UV laser beam filamentation and a repetitive pulse train on creation of prolonged plasma channels in atmospheric air", *Nuclear Instruments and Methods in Physics Research B*, **309**, 218 (2013).
Abstract. Amplitude-modulated UV laser pulse of up to 30 J energy was produced at hybrid Ti:Sapphire/KrF GARPUN-MTW laser facility when a preliminary amplified train of short pulses was injected into unstable resonator cavity of the main e-beam-pumped KrF amplifier. The combined radiation consisted of regeneratively amplified picosecond pulses with subTW peak power overlapped with 100-ns pulse of a free-running lasing. The advantages of combined radiation for production of long-lived prolonged plasma channels in air and HV discharge triggering were demonstrated: photocurrent sustained by modulated pulse is two orders of magnitude higher and HV breakdown distance is twice longer than for a smooth UV pulse. It was found that in contrast to IR radiation multiple filamentation of high-power UV laser beam does not produce extended nonlinear focusing of UV radiation.

7. V.D. Zvorykin, A.A. Ionin, A.O. Levchenko, G.A. Mesyats, L.V. Seleznev, D.V. Sinitsyn,I.V. Smetanin, E.A. Sunchugasheva, N.N. Ustinovskii, A.V. Shutov "Production of extended plasma channels in atmospheric air by amplitude-modulated UV radiation of GARPUN-MTW Ti : sapphire – KrF laser. Part 1. Regenerative amplification of subpicosecond pulses in a wide-aperture electron beam pumped KrF amplifier" *Quantum. Electron*., 43 (4), 332 (2013).
Abstract. Regenerative amplification of single and multiple ultrashortsubpicosecond UV pulses in a wide-aperture KrF amplifier with an unstable confocal resonator was investigated on theGARPUN-MTW hybrid laser system. Amplitude-modulated100-ns long UV radiation pulses with an energy of several tens of joules were obtained at the output of the system. The pulses were a combination of a quasi-stationary oscillation pulse and a train of amplified ultrashort pulses (USPs) with a peak power of 0.2 – 0.3TW, which exceeded the power of free-running lasing pulse by three orders of magnitude. The population inversion recovery time in the active KrF laser medium was estimated: $\tau_e \geq 2.0$ ns. Trains of USPs spaced at an interval $\Delta t \approx \tau_e$ were shown to exhibit the highest amplification efficiency. The production of amplitude-modulated UV pulses opens up the way to the production and maintenance of extended plasma channels in atmospheric air.

8. V.D. Zvorykin, A.A. Ionin, A.O. Levchenko, G.A. Mesyats, L.V. Seleznev, D.V. Sinitsyn,I.V. Smetanin, E.A. Sunchugasheva, N.N. Ustinovskii, A.V. Shutov "Production of extended plasma channels in atmospheric air by amplitude-modulated UV radiation of GARPUN-MTW Ti : sapphire – KrF laser. Part 2. Accumulation of plasma electrons and electric discharge control" *Quantum. Electron*., 43 (4), 339 (2013).
Abstract. The problem of the production of extended (~1 m) plasma channels is studied in atmospheric air by amplitude-modulated laser pulses of UV radiation, which are a superposition of a subpicosecond USP train amplified in a regenerative KrF amplifier with an unstable confocal resonator and a quasi-stationary lasing pulse. The USPs possess a high (0.2 – 0.3 TW) peak power and efficiently ionize oxygen molecules due to multiphoton ionization, and the quasi-stationary lasing pulse, which has a relatively long duration(~100 ns), maintains the electron density at a level $n_e = (3 – 5). 10^{14}$ cm^{-3} by suppressing electron attachment to oxygen. Experiments in laser triggering of high-voltage electric discharge ssuggest that the use of combined pulses results in a significant lowering of the breakdown threshold and enables controlling the discharge trajectory with a higher efficiency in comparison with smooth pulses.

It was shown that controlled breakdowns may develop with a delay of tens of microseconds relative to the laser pulse, which is many orders of magnitude greater than the lifetime of free electrons in the laser-induced plasma. We propose a mechanism for this breakdown, which involves speeding-up of the avalanche ionization of the air by negative molecular oxygen ions with a low electron binding energy (~0.5 eV) and a long lifetime(~1 ms), which are produced upon cessation of the laser pulse.

9. Dergachev A.A., Ionin A.A., Kandidov et al. "Filamentation of IR and UV femtosecond pulses upon focusing in air" *Quantum. Electron*., 43 (1), 29 (2013).
*Abstract.*The filamentation of IR and UV laser pulses has been studied numerically and experimentally for different initial beam focusing geometries, and linear electron density profiles along the plasma channel of filaments have been obtained. The results demonstrate that changes in laser beam focusing have a stronger effect on filament and plasma channel parameters for UV radiation than for IR radiation. Focusing causes individual high fluence regions produced by refocusing to merge to form a continuous extended filament with a continuous plasma channel.

10. Geints Y.E., Zemlyanov A.A., Izyumov N.A., et al. "Self-focusing of profiled ultrashort-wavelength laser beams in air" *JETP*, **116** (2), 197 (2013)
*Abstract.*We report on the results of laboratory experiments of filamentation of sharply focused gigawatt femtosecond laser radiation passed through various aperture diaphragms in air. For the multiple filamentation regime, the dependences of the length and spatial structure of the filamentation region on the initial beam profile are established. It is found that light beam profiling by a diaphragm leads in some cases to a displacement of the filamentation region and to repeated self-focusing of radiation behind the linear focal waist. In the beam of the same power in the absence of a diaphragm and in the regime of the formation of a single filament, this effect terminates in front of the geometrical focus. The experimental results are illustrated by numerical simulation data.

11. A.A. Ionin, N.G. Iroshnikov, O. Kosareva, A. Larichev, D. Mokrousova , N.A. Panov, L.V. Seleznev, D.V. Sinitsyn, E.S. Sunchugasheva, "Filamentation of femtosecond laser pulses governed by variable wavefront distortions via a deformable mirror", 2013, *JOSA B*, **30** p.2257.
Abstract. Filamentation of focused UV and IR femtosecond laser pulses and plasma channel formation governed by variable wavefront distortions was experimentally and numerically studied. A deformable mirror was used to control the plasma channel length by introducing a spherical aberration into the initial transverse spatial distribution of a femtosecond laser pulse. An at least double increase of the plasma channel length was observed with increasing deformation of the mirror. Numerical calculations show that the hat-like phase shape of the aberration ensures that the energy of the initial laser pulse remains confined for a longer distance within the limited transverse size of the filament.

12. A.V. Shutov, I.V. Smetanin, A. A. Ionin, A.O. Levchenko, L.V. Seleznev, D.A. Sinitsyn, N. N. Ustinovskii, V.D. Zvorykin, "Direct measurement of the characteristic three-body electron attachment time in the atmospheric air in direct current electric field", *Appl. Phys. Lett*., 2013, **103**, 034106.
Abstract. We report the results of theoretical and experimental study of the characteristic time for three-body attachment of electrons produced by 100 fs UV laser pulse in the atmosphere air in the external DC electric field ranged from 0.2 to 10 kV/cm.

13. A.A. Ionin, S.I. Kudryashov, A.O. Levchenko, et al., "Triggering and Guiding of Electric Discharge by a Train of Sub-TW UV Laser Pulses", *Proc. SPIE*, 2013, **8796**, 87961M.
Abstract. Non-self-sustained electric discharge and electric breakdown were triggered and guided by a train of ultrashort sub-TW ultraviolet (UV) pulses overlapped with a long free-running UV pulse of a hybrid Ti:Sapphire - KrF laser facility. Photocurrent sustained by this train is two orders of magnitude higher, and electric breakdown distance is twice longer than those for the discharge triggered by the long UV pulse only. When transporting the laser radiation over the long distance, UV filaments of ~ 100 m length were observed.

14. A.Ionin , L.Seleznev and E.Sunchugasheva, Controlling plasma channels through ultrashort laser pulse filamentation, *Proc. of SPIE* **8898**, 88980Z (2013)
Abstract. A review of studies fulfilled at the Lebedev Institute in collaboration with the Moscow State University and Institute of Atmospheric Optics in Tomsk (Siberia) on influence of various characteristics of ultrashort laser pulse on plasma channels formed under its filamentation is presented. Filamentation of high-power laser pulses with wavefront controlled by a deformable mirror, with cross-sections spatially formed by various diaphragms and with different wavelengths was experimentally and numerically studied. An application of plasma channels formed due to filamentation of ultrashort laser pulse including a train of such pulses for triggering and guiding electric discharge is discussed.

15. A.A. Ionin, S.I. Kudryashov, D.V. Mokrousova, L.V. Seleznev, D.V. Sinitsyn, E.A. Sunchugasheva "Plasma channels under filamentation of infrared and ultraviolet double femtosecond laser pulses", *Laser Physics Letters*, **11** (1), 016001 (2014).
*Abstract.*The influence of a plasma channel, created by a filament of focused UV or IR femtosecond laser pulse (λ = 248 or 740 nm), on the characteristics of another plasma channel formed by a femtosecond pulse at the same wavelength following the first one with varied nanosecond time delays was experimentally studied. The dependence of the optical transparency of the first channel and the plasma density of the second channel on the time delay was demonstrated to be quite different for such double UV and IR femtosecond pulses.

Attachment 2. List of presentations at conferences and meetings with abstracts

1. A.A.Ionin, "Guiding electric discharge by combined nanosecond and femtosecond pulses" (invited), Int. Conf. SPIE Security+Defence, 19-22 Sept. 2011, Prague, Czech Republic, *Techn. Program*, p.61 (2011)
Abstract. Non-self-sustained electric discharge and electric breakdown were triggered and guided by a train of picosecond ultraviolet (UV) pulses overlapped with a long free-running UV pulse of a hybrid Ti:Sapphire-KrF laser facility. Photocurrent sustained by this train is two orders of magnitude higher, and electric breakdown distance is twice longer than those for the discharge triggered by the long UV pulse only.

2. V.D. Zvorykin, A.A. Ionin, S.I. Kudryashov, A.O. Levchenko, L.V. Seleznev, A.V. Shutov, D.V. Sinitsyn, I.V. Smetanin, and N.N. Ustinovsky, "Extended ionized channel in atmosphere created by sub-terawatt modulated UV laser pulse", XXXIX International conference on plasma physics and Controlled Thermonuclear Fusion, 6-10 Feb 2012, Zvenigorod (Zvenigorod, IOFRAN, 2012) p. 220.
Abstract. Non-self-sustained electric discharge and electric breakdown were triggered and guided by a train of picosecond ultraviolet (UV) pulses overlapped with a long free-running UV pulse of a hybrid Ti:Sapphire-KrF laser facility. Photocurrent sustained by this train is two orders of magnitude higher, and electric breakdown distance is twice longer than those for the discharge triggered by the long UV pulse only.

3. A.A.Ionin, S.I.Kudryashov, A.O.Levchenko, L.V.Seleznev, A.V.Shutov, D.V.Sinitsyn, I.V.Smetanin, N.N.Ustinovsky, V.D.Zvorykin, Triggering and guiding electric discharge by a train of sub-TW ultrashort UV pulses, (invited), *Abstracts* of 15-th International Conference "Laser Optics 2012" on CD, St.Petersburg, June 25-29, (2012)
Abstract. Non-self-sustained electric discharge and electric breakdown were triggered and guided by a train of ultrashort sub-TW UV pulses overlapped with a long (~100ns) free-running UV pulse of a hybrid Ti:Sapphire-KrF laser facility. Photocurrent sustained by this train is two orders of magnitude higher, and electric breakdown distance is twice longer than those for the discharge triggered by the long UV pulse only.

4. V.D. Zvorykin, A.A. Ionin, A.O. Levchenko, L.V. Seleznev, A.V. Shutov, D.V. Sinitsyn, I.V. Smetanin, N.N. Ustinovskii, "Amplification of a train of uv picosecond subtw pulses combined with a 100-ns pulse at garpun-mtw KrF laser facility", *Abstract*s of 15th International Conference "Laser Optics 2012" on CD, St.Petersburg, Russia, June 25 - 29, 2012
Abstract. Regenerative amplification of single and multiple ultrashort subpicosecond UV pulses in a wide-aperture KrF amplifier with an unstable confocal resonator was investigated on the GARPUN-MTW hybrid laser system.

5. V.D. Zvorykin, A.A. Ionin, A.O. Levchenko, L.V. Seleznev, D.V. Sinitsyn, I.V. Smetanin, N.N. Ustinovskii, A.V. Shutov, "Extended plasma channels in the atmospheric air produced by UV Ti:Sapphire/KrF GARPUN-MTW laser for guiding MW radiation and HV electric discharge" (keynote lecture), 25th Symposium on Plasma Physics and Technology, June 18-21, 2012, Prague, Czech Republic
Abstract. Electric breakdown and non-self-sustained electric discharge were triggered and guided by a train of picosecond ultraviolet (UV) pulses overlapped with a long free-running UV pulse of a hybrid Ti:Sapphire-KrF laser facility. Photocurrent sustained by this train is two

orders of magnitude higher, and electric breakdown distance is twice longer than those for the discharge triggered by the long UV pulse only.

6. A.A. Ionin, S.I. Kudryashov, A.O. Levchenko, L.V. Seleznev, A.V. Shutov, D.V. Sinitsyn, I.V. Smetanin, N.N. Ustinovsky, and V.D. Zvorykin, "Triggering and guiding electric discharge by a train of ultrashort UV pulses" (invited), Int. Conf. High Power Laser Ablation HPLA 2012, 30 April-3 May 2012, Santa Fe, NM, USA.
Abstract. Non-self-sustained electric discharge and electric breakdown were triggered and guided by a train of ultrashort sub-TW ultraviolet (UV) pulses overlapped with a long free-running UV pulse of a hybrid Ti:Sapphire-KrF laser facility. Photocurrent sustained by this train is two orders of magnitude higher, and electric breakdown distance is twice longer than those for the discharge triggered by the long UV pulse only. When transporting the laser radiation over the long distance, UV filaments of ~100 m length were observed.

7. A.A.Ionin, S.I.Kudryashov, A.O.Levchenko, L.V.Seleznev, A.V.Shutov, D.V.Sinitsyn, I.V.Smetanin, E.S.Sunchugasheva, N.N.Ustinovsky, V.D.Zvorykin Triggering and Guiding of Electric Discharge by a Train of Sub-TW UV Laser Pulses (invited), The 2nd International Symposium on Laser Interaction with Matter, Sept. 9th~12th, Xi'an, Shaanxi, P. R. China, 2012
Abstract. Electric breakdown and non-self-sustained electric discharge were triggered and guided by a train of ultrashort sub-TW ultraviolet (UV) pulses overlapped with a long free-running UV pulse of a hybrid Ti:Sapphire-KrF laser facility. Photocurrent sustained by this train is two orders of magnitude higher, and electric breakdown distance is twice longer than those for the discharge triggered by the long UV pulse only. UV filaments of ~100 m length were observed when transporting the laser radiation over the long distance.

8. Smetanin I.V., Levchenko A.O., Schutov A.V., Ustinovskii N. N., Zvorykin V.D. "Resonance enhanced multi-photon ionization of atmospheric air in the field of high-power UV laser radiation" 15th International Conference on Laser Optics, June25-29, 2012, St. Petersburg, Technical Program, paper ThR5-32, p.49.
Abstract. We report the results of experimental and theoretical investigation of multi-photon ionization of atmospheric air in the field of high-power nanosecond GARPUN KrF laser radiation. We have found in experiment that the dominant air ionization process is (2+1) REMPI of molecular oxygen, the ionization yield scales as squared intensity at 4x10^8 to 10^11 W/cm^2. Theory of coherent and incoherent (2+1) REMPI is developed which is in agreement with our experimental results.

9. A. A. Ionin, S. I. Kudryashov, A. O. Levchenko, L. V. Seleznev, A. V. Shutov, D. V. Sinitsyn, I. V. Smetanin, N. N. Ustinovsky, and V. D. Zvorykin, Triggering and guiding electric discharge by a train of ultrashort UV pulses and a long UV pulse emitted by a hybrid Ti:Sapphire-KrF laser facility (invited), SPIE Security + Defence Conf., 24-27 Sept 2012, Edinburgh, UK, *Book of Abstracts*, p.72.
Abstract. Non-self-sustained electric discharge and electric breakdown were triggered and guided by a train of ultrashort sub-TW ultraviolet (UV) pulses overlapped with a long free-running UV pulse of a hybrid Ti:Sapphire - KrF laser facility. Photocurrent sustained by this train is two orders of magnitude higher, and electric breakdown distance is twice longer than those for the discharge triggered by the long UV pulse only. When transporting the laser radiation over the longdistance, UV filaments of ~ 100 m length were observed.

10. V.D. Zvorykin, A.A. Ionin, A.O. Levchenko, L.V. Seleznev, A.V. Shutov, D.V. Sinitsyn, I.V. Smetanin, and N.N. Ustinovsky, "Filamentation of subpicosecond UV pulse with terawatt

peak-power created by hybrid Ti:sapphire/KrF laser system GARPUN-MTW", XL International conference on plasma physics and, 11-15 Feb 2013 г., Zvenigorod
Abstract. Filamentation of subpicosecond UV pulses with terawatt peak-power created by hybrid Ti:sapphire/KrF laser system was studied. Long range filaments were observed.

11. V.D. Zvorykin, A.A. Ionin, A.O. Levchenko, L.V. Seleznev, D.V. Sinitsyn, I.V. Smetanin, N.N. Ustinovskii, A.V. Shutov, "Formation and application of extended plasma channels produced in atmospheric air by trains of picosecond UV pulses at GARPUN-MTW Ti:Sa/KrF laser", 6th International Conference on the Frontiers of Plasma Physics and Technology FPPT'13, 4-8 March 2013, Gaborone, Botswana, Book of *Abstract*s.
Abstract. Experiments in laser triggering of high-voltage electric discharges suggest that the use of combined pulses results in a significant lowering of the breakdown threshold and enables controlling the discharge trajectory with a higher efficiency in comparison with smooth pulses.

12. V.D. Zvorykin, A.A. Ionin, L.V. Seleznev, A.O. Levchenko, D.V. Sinitsyn, I.V. Smetanin, E.A. Sunchugasheva, N.N. Ustinovskii, A.V. Shutov, "Multiple filamentation of picosecond sub-terawatt UV radiation pulses generated by Ti:Sapphire/KrF laser system GARPUN-MTW", ICONO/LAT 2013, June 23-26, 2013, Moscow, Russia, Conference program, p.107, Technical digest on CD.
Abstract. Multiple filamentation of UV picosecond pulses being amplified at hybrid Ti:Sapphire/KrF laser facility GARPUN-MTW was investigated under propagation along an extended air distance of ~100 m. Peak pulse power attained 0.3 TW, which is in 3000 times higher than the critical value (~108 W) for filamentation of 248 nm wavelength radiation. In contrast to IR radiation filamentary UV laser beam does not reveal extended nonlinear focusing.

13. V.D. Zvorykin, A.A. Ionin, A.O. Levchenko, L.V. Seleznev, D.V. Sinitsyn, I.V. Smetanin, N.N. Ustinovskii, A.V. Shutov, "Guiding of HV electric discharge by amplitude-modulated UV radiation of Ti:Sapphire/KrF GARPUN-MTW laser", *Abstract*s of International Symposium on Fundamentals of Laser Assisted Micro & Nanotechnologies (FLAMN-13), 24-28 June 2013, Poushkin/St. Petersburg, Russia.
Abstract. The possibility of electric discharge control by amplitude-modulated UV pulses was demonstrated. Experiments in laser triggering of high-voltage electric discharges suggest that the use of combined pulses results in a significant lowering of the breakdown threshold and enables controlling the discharge trajectory with a higher efficiency in comparison with smooth pulses.

14. V.D. Zvorykin, A.A. Ionin, A.O. Levchenko, L.V. Seleznev, D.V. Sinitsyn, I.V. Smetanin, N.N. Ustinovskii, A.V. Shutov, "Air ionization by UV picosecond subTW laser pulses combined with 100 ns GW pulse at GARPUN-MTW Ti:Sapphire/KrF laser facility", 22nd Laser Physics Workshop LPHYS'13, 15-19 July 2013, Prague, Czech Republic, Program, p.57.
Abstract. The hybrid Ti:Sapphire/KrF GARPUN-MTW laser system is its capability to generate amplitude-modulated UV radiation combined of amplified train of picosecond USPs with peak power up to 0.3 TW and 100-ns free-running laser pulse. Filamentation of the pulse along up to 100 m distance was studied.

15. A.A. Ionin, "Controlling plasma channels through ultrashort laser pulse filamentation" (invited), ICONO/LAT 2013, June 23-26, 2013, Moscow, Russia, Conference program, p.95, Technical digest on CD.

Abstract. A review of studies fulfilled at the Lebedev Institute in collaboration with the Moscow State University and Institute of Atmospheric Optics in Tomsk on influence of various characteristics of ultrashort laser pulse on plasma channels formed under its filamentation is presented. Filamentation of high-power laser pulses with wavefront controlled by a deformable mirror, with cross-sections spatially formed by various diaphragms and with different wavelengths was experimentally and numerically studied. An application of plasma channels formed due to filamentation of ultrashort laser pulse including a train of such pulses for triggering and guiding long electric discharges is discussed.

16. E.S. Sunchugasheva, A.A. Ionin, S.I. Kudryashov, L.V. Seleznev, D.V. Sinitsyn, N.G. Iroshnikov, O.G. Kosareva, A.V. Larichev, N.V. Panov, "Femtosecond laser pulse filamentation in air controlled by the pulse aberration", ICONO/LAT 2013, June 23-26, 2013, Moscow, Russia, *Conference program*, p.116, Technical digest on CD.
Abstract. Self-focusing of spatially shaped femtosecond laser pulse was numerically and experimentally studied. By using such a pulse relocating of filament area and radiation refocusing behind the linear focal point was demonstrated.

17. A. Ionin, L. Seleznev, and E. Sunchugasheva, "Control of plasma channel parameters at filamentation of femtosecond laser pulses" (invited), 22th International Laser Physics Workshop (LPHYS'13), July 15–19, 2013, Prague, Czech Republic, Program, p. 56 (2013).
Abstract. Influence of various characteristics of ultrashort laser pulse on plasma channels formed under its filamentation is presented as a review of studies fulfilled at the Lebedev Institute in collaboration with the Moscow State University and Institute of Atmospheric Optics in Tomsk on. Filamentation of high-power laser pulses with wavefront controlled by a deformable mirror, with cross-sections spatially formed by various diaphragms and with different wavelengths was experimentally and numerically studied. An application of plasma channels formed due to filamentation of ultrashort laser pulse including a train of such pulses for triggering and guiding long electric discharges is discussed.

18. A.Ionin, "Controlling plasma channels through ultrashort laser pulse filamentation"(invited), Int SPIE Symposium Security+Defence 2013, 23-26 Sept 2013, Dresden,Germany, *Book of Abstracts.*
Abstract. Influence of various characteristics of ultrashort laser pulse on plasma channels formed under its filamentation is presented as a review of studies fulfilled at the Lebedev Institute in collaboration with the Moscow State University and Institute of Atmospheric Optics in Tomsk on. Filamentation of high-power laser pulses with wavefront controlled by a deformable mirror, with cross-sections spatially formed by various diaphragms and with different wavelengths was experimentally and numerically studied. An application of plasma channels formed due to filamentation of ultrashort laser pulse including a train of such pulses for triggering and guiding long electric discharges is discussed.

19. I.V. Smetanin, A.O. Levchenko, A.V. Shutov, N.N. Ustinovskii, V.D. Zvorykin, "Resonance Enhanced Multi-Photon Ionization of Atmospheric Air by High-Power KrF Laser Radiation", International Conference on Coherent and Nonlinear Optics (ICONO) & Conference on Lasers, Applications, and Technologies ICONO/LAT 2013, 18-22 June 2013, Moscow, Russia, p.78.
Abstract. (2+1) REMPI of molecular oxygen in atmospheric air by the nanosecond GARPUN KrF laser radiation is investigated. We have measured the ionization yield scales as squared intensity at 4x10^8 to 10^11 W/cm^2. Theory of coherent and incoherent (2+1) REMPI is developed in the wide domain of pulse duration, from the ultrashort pulses shorter than

polarization relaxation time up to durations of hundred nanoseconds, which is in agreement with our experimental results.

20. A.V. Shutov, I.V. Smetanin, A.O. Levchenko, N.N. Ustinovskii, V. D. Zvorykin, "Direct Measurement of the Characteristic Three-Body Electron Attachment Rates in Atmospheric Air in DC Electric Field", International Conference on Coherent and Nonlinear Optics (ICONO) & Conference on Lasers, Applications, and Technologies ICONO/LAT 2013, 18-22 June 2013, Moscow, Russia, p.115.
Abstract. We report the results of theoretical and experimental study of the characteristic time for three-body attachment of laser-plasma electrons in the atmosphere air in the external DC electric field with the strength ranged from 0.1 to 10 kV/cm.

21. I.V. Smetanin, V.D. Zvorykin , A.O. Levchenko, A.V. Shutov, N.N. Ustinovskii, "Theory of the (2+1) Resonance Enhanced Multi-Photon Ionization of Atmospheric Air by High-Power UV Laser Radiation", 22nd Laser Physics Workshop LPHYS'13, 15-19 July 2013, Prague, Czech Republic, *Program*, p.30.
Abstract. Resonance enhanced multi-photon ionization (REMPI) of air molecules in the field of high-power UV laser radiation is very promising for the formation of long ionized channels in the atmosphere. At the laser wavelength $\lambda \approx 248\ nm$, (2+1) REMPI in O_2 consists in the two-photon excitation of the intermediate relatively long lifetime 3s $C^3\Pi_g$ Rydberg state followed by the one-photon ionization. We have measured that the ionization yield at moderate intensities $\sim 4\times10^8 \div 10^{11}$ W/cm^2 scales as intensity to the second power for nanosecond-domain pulse durations, which is the sign of predominant (2+1) REMPI process.Here we report the theory of (2+1) REMPI of molecules in the field of high-power UV laser radiation. Depending on relation between the laser pulsewidth τ_p and the polarization relaxation time T_2 of two-photon resonance transition, the laser-molecule interaction proceeds in coherent ($\tau_p < T_2$) or incoherent ($\tau_p > T_2$) regimes.The self-focusing of UV laser pulse is discussed when (2+1) REMPI process dominates. Resonant character of interaction lead to the decrease in the self-focusing threshold, which in the coherent interaction regime depends on the pulse energy rather than the pulse power characteristic for Kerr –dominating nonlinearity.

22. V.D. Zvorykin , A.A. Ionin, L.V. Seleznev, A.O. Levchenko, D.V. Sinitsyn, I.V. Smetanin, E.A. Sunchugasheva, N.N. Ustinovskii, and A.V. Shutov "Multiple Filamentation of the UV Supercritical Laser Beam" X International Symposium «Radiation from Relativistic Electrons in Periodic Structures "RREPS-13" merged with "Meghri-13"» 23-27 September 2013, Armenia, Yerevan. *Book of Abstract*s, p. 22
Abstract. Multiple filamentation of UV picosecond pulses with P~0.3 TW (P/P_{cr}~3000) being produced at GARPUN-MTW Ti:Sapphire/KrF laser facility was investigated for the first time under propagation along an extended air distance of ~100 m in various focusing geometries (NA=1.5·10^{-2} − 1.5·10^{-3}).

23. V.D. Zvorykin, A.A. Ionin, A.O. Levchenko, L.V. Seleznev, A.V. Shutov, D.V. Sinitsyn, I.V. Smetanin, N.N. Ustinovskii "Effects of picosecond terawatt UV laser beam filamentation and a repetitive pulse train on creation of prolonged plasma channels in atmospheric air" 5th International Conference "Charged and Neutral Particles Channeling Phenomena" September 23-28, 2012 Alghero (SS), Italy. *Book of Abstract*s, p. 156.
Abstract. Multiple filamentation over very long propagation distances ~ 100 m was measured for peak pulse power exceeding the critical value for λ=248-nm radiation (~10^8 W) in 2000 times. An all-reflection mirror focusing scheme with a small numerical aperture of about 3 10^{-4} was designed. The intensity distribution was recorded by using glass plate fluorescence under

UV irradiation with imaging at the time-gated CCD. It was found that the filamentation of high-power UV laser beam is quite different of longer wavelengths.

Attachment 3. Information on patents and copy rights

There were no any patents claimed and obtained during the Project. Authors' copy rights can be claimed on the scientific results formulated in above mentioned publications.